Photovoltaic Technologies Developed for Space-Based Solar Power

Thesis by

Samuel Loke

In Partial Fulfillment of the Requirements for the

Degree of

Doctor of Philosophy

CALIFORNIA INSTITUTE OF TECHNOLOGY

Pasadena, California

2022

Defended May 3, 2022

Samuel Loke

ORCID: 0000-0003-1856-3605

Acknowledgements

Every graduate student's doctoral programme is challenging and arduous in their own way. Such a programme cannot be done without the support of a village's worth of fantastic people supporting said student. I am no different, and it gives me great pleasure and pride to acknowledge here the amazing human beings who helped me see this thesis through to completion.

I'd like to start by thanking my family: my father Daniel Loke, my mother Lay Lee Ng, and my sister Desiree Loke who were my emotional, logistical, and financial bedrock through it all. They gave me life guidance through the hardest parts of the programme and were there for me when the hour was darkest. Much more folly would be have been committed were it not for their patience and sage advice.

I'd also like to thank my Dungeons and Dragons playgroup comprising Oscar Zamora, Maria Zamora-Hopper, Elizabeth Bennett, and Emmy Cobb. Dungeons and Dragons is a logistical game where you wrangle the schedules of 5-6 consenting adults with adult lives and deadlines, in order to meet for 3 hours on a regular basis in the name of friendship and adventure. I was truly blessed with some of the finest folk on this front. Through a whole real world plague, we continued to meet once a fortnight, and till the end of this programme we continue to meet. We've seen each other through some of our greatest challenges, and I am honoured to have met and journeyed with you all, in game and in real life.

Thanks must also go out to my advisor, Harry Atwater, without whom I would not have had the opportunity to delve into this very exciting body of work. Without his patience and academic guidance, none of this work would be possible, and I would be unable to explore the stars as I have done these past seven years. Thank you for accepting me into your team and teaching me so much.

Just as equally, credit must be given to my colleagues in the Atwater team and collaborators. The Caltech SSPI team of Nina Vaidya, Ali Naqavi, Michael Kelzenberg, Pilar Espinet-Gonzalez, Emily Warmann, Jing-Shun Huang, and Arky Yang, as well as collaborator Stepan Demchyschyn from JKU, have all been wonderful people to work with, and I learnt much from everyone. I'm thankful for having had the opportunity to work with you all.

Finally, I'd like to thank Coco for seeing me through some hard times.

Abstract

In this thesis, photovoltaic technologies were developed for space-based solar power. Two methods of realizing SBSP were introduced, namely concentrated photovoltaics (CPV) and radiation hard flat panel photovoltaics. Both techniques are instrumental to realizing SBSP as they are pathways to realizing high specific power and lower launch costs. Technologies developed to support these two forms of SBSP were then reported.

In support of CPV, ultralight broadband mid-infrared coatings were developed for the concentrating mirrors used in our project. This was done to create radiative pathways for heat loss to ensure that the solar cells do not overheat. Using the rigorous coupled wave analysis technique, we optimized a backside single-layer coating using 2nm Cr/ 2µm CP1/ 500nm Ag that had an mIR emissivity of 0.6. Adding a second layer of this coating, we predicted that a 0.5nm Cr/ 1.9µm CP1/ 3nm Cr/ 2µm CP1/ 500nm Ag screen could achieve an emissivity of 0.8. We also optimized a 10nm ITO/ 2 µm CP1/ 500nm Ag frontside emitter which had a visible reflectivity of 0.896 and a mIR emissivity of 0.554. A backside emitter coating that was 0.927 emissive in the mIR with areal density 6.0 gm^{-2} was successfully fabricated, as was a frontside mirror emitter coating with visible reflectivity of 0.896 and a mIR emissivity of 0.582 with areal density 4.1 gm^{-2}.

In support of radiation hard photovoltaics, organo-lead halide perovskites (OHLP) were investigated. Challenges facing their fabrication were explored, with special focus on the electron transport layer PCBM as well as OHLP formulation. It was found that doping PCBM with a surfactant CTAB was beneficial, but did not work with all surfaces. An ITO/NiO_x/MAPbI3/CTAB+PCBM/Cu device with in-house champion efficiency of 12.41% was achieved, and an ITO/NiOx/$FA_{0.85}Cs_{0.15}PbI_3$/PCBM/Cu device with in-house champion efficiency of 11.81% was achieved. Time-dependant drift diffusion modelling was employed to account for the S-kink arising from poor PCBM carrier concentration.

Finally, the proton degradation of OHLP devices and constituent transport layers were investigated to shed better light on how OHLP devices degrade under proton irradiation. Films of ITO, PEDOT, NiOx, PCBM, and PTCDi were found to degrade under 30keV and 75keV protons of up to 1.4 x 10^{14} p^+cm^{-2} fluence, but their electrical resistivity and optical transmissivity were not found to impact the cell as much as the OHLP absorber layer itself. Observing the light IV and EQE degradation of OHLP cells, it is evident that proton deposition in the OHLP layer itself causes the most damage, especially at 30keV and 75keV protons with fluences from 4.3 x 10^{13} p^+cm^{-2} to 1.7 x 10^{14} p^+cm^{-2}. By considering the discrepancy in trends between J_{sc} and EQE, we concluded that the protons much accelerate intensity-based metastable photodegradation. Finally, by observing their anneal recovery, we concluded that it was temperature dependant and that maximum irrecoverable damage occurs at the OHLP/HTL interface.

Published Content and Contributions

[1] E. C. Warmann, P. Espinet-Gonzalez, N. Vaidya, S. Loke, A. Naqavi, T. Vinogradova, M. Kelzenberg, C. Leclerc, E. Gdoutos, S. Pellegrino and H. A. Atwater, "An ultralight concentrator photovoltaic system for space solar power harvesting," *Acta Astronautica,* vol. 170, pp. 443-451, 2020. https://doi.org/10.1016/j.actaastro.2019.12.032

S.L. helped simulate and characterize the ITO Salisbury screen.

[2] A. Naqavi, S. P. Loke, M. D. Kelzenberg, D. M. Callahan, T. Tiwald, E. C. Warmann, P. Espinet-Gonzalez, N. Vaidya, T. A. Roy, J.-S. Huang, T. G. Vinogradova and H. A. Atwater, "Extremely broadband ultralight thermally-emissive optical coatings," *Optics Express,* vol. 26, no. 14, pp. 18545-18562, 2018. https://doi.org/10.1364/OE.26.018545

S.L. helped optimize, fabricate, and characterize the 1-layer and 2-layer Cr Salisbury screens.

Contents

List of Illustrations

List of Tables

Chapter 1: Space-Based Solar Power

1.1 Principles of Space-Based Solar Power

Researchers, companies, and governments across the globe are on a race to find sustainable sources of clean, renewable energy to combat the many environmental and industrial challenges that beset our current society. Annual global electricity consumption is well into the 20 000 TWh range [1], and in the US, at least 60% of this electricity is still generated through means of combustion [2] that produce harmful greenhouse emissions responsible for climate change [3]. Amongst the modern-day suite of renewable sources of energy, solar power, and in this case photovoltaics, stands amongst them as a hot topic. It is a very alluring prospect to harness the power of the Sun, an energy source that had existed 4.6 billion years before civilization and, given its predicted 10 billion year lifespan, will likely last long after [4]. From an engineering point of view, the Sun delivers up to about 1.37 kWm^{-2} of sunlight [5]. Given modern day terrestrial photovoltaic harvesting, it has been estimated that this is more than enough to meet current day energy demands [6]. To the photovoltaic researcher, our motivation is thus to advance the efficiency with which we harvest solar power, not just by considering intrinsic device efficiency, but also considering the limitations of solar power and how to solve it.

There are three major shortcomings intrinsic to terrestrial photovoltaic harvesting. First, a portion of useful sunlight is always lost to the atmosphere through scattering. Figure 1.1 plots three different spectra: the AM0 spectra seen just outside the Earth's atmosphere, the AM1.5 direct spectra seen at the equator at oblique incidence, and the AM1.5 global spectra averaged across the globe [5] [7]. Numerically, AM0 illumination offers up to the 1.37kWm^{-2} as mentioned earlier, while AM1.5 illumination offers a maximum of 1kwm^{-2}. The second issue lies in the day night cycle every point on Earth is subject to, meaning no matter where one builds their solar plant, there will always be downtime where energy cannot be harvested. This intrinsic limitation compounds into a third issue because, somewhat paradoxically, electricity demand has been shown to rises in the evening [8], meaning that photovoltaic energy generated during the day must be stored for the night, causing additional losses. When designing terrestrial solar panels, these three limitations must be accounted for and designed around.

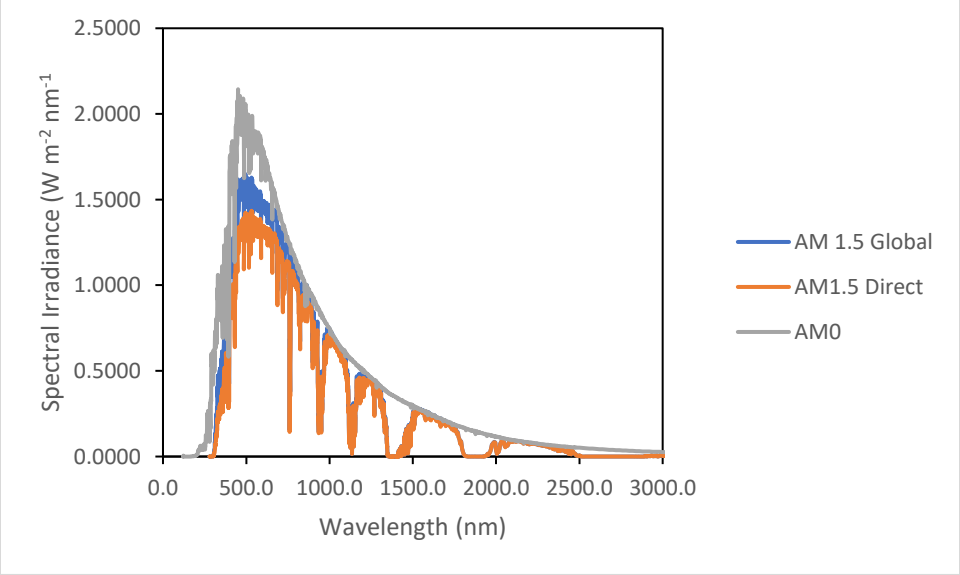

Figure 1.1. Spectral plots of the AM0, AM1.5 Direct, and AM1.5 Global solar intensity spectra [5] [7].

It is here that we introduce the idea of space-based solar power (SBSP). Figure 1.2 shows a schematic of how this technology works. The concept of SBSP is to launch an array of photovoltaic cells into orbit around the Sun where they may harvest solar energy. This harvested electric energy will then be transmitted to Earth wirelessly, usually through a microwave phased array transmitter, where it will be collected at terrestrial rectenna stations and re-converted back to useful electricity [9]. Although the technology is presently still very young and costly [10], it is capable of overcoming the aforementioned shortcomings. Firstly, we are harvesting the energy in space, allowing us to be privy to that higher intensity of sunlight. This translates to more solar power. Second, instead of being restricted to a fixed point on Earth, our solar cells are now orbiting the Earth, meaning that if we engineer the orbit correctly, we can make sure that the solar cells are never shadowed by the Earth during nighttime, either via a far geostationary orbit or a short period low earth orbit [11]. Since it is always noon in space, the correct orbit will overcome the intrinsic day-night limitation terrestrial solar cells experience. Finally, by being in space and wirelessly transmitting power 24 hours a day, 7 days a week, we can easily deliver noon levels of power to areas that are experiencing night, overcoming the energy storage issues. Inspired by the elegance with which this exciting, radical technology solves some of solar power's intrinsic problems, we commit this thesis to the development and study of photovoltaic technologies for SBSP.

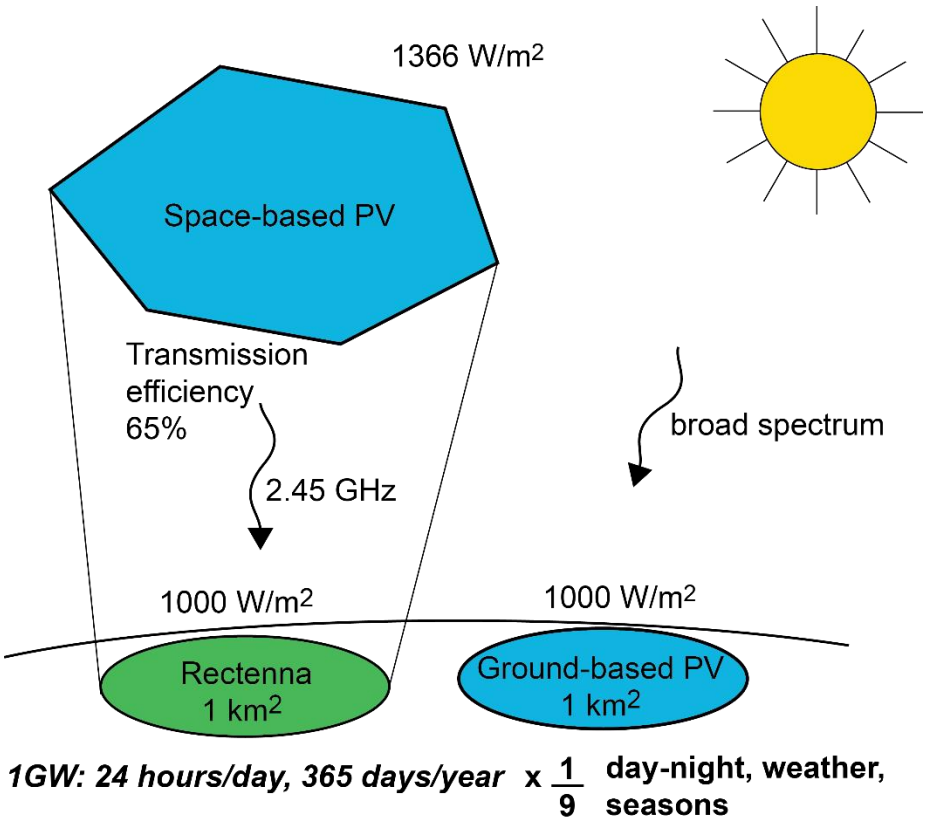

Figure 1.2. Schematic demonstrating the operating principles of SBSP.

The biggest hurdle to more widespread implementation of SBSP lies in the launch cost of sending photovoltaic cells, or indeed any payload, into space. Despite growing demand for private space missions, together with a major effort to commercialize space missions [12], launch costs remain mass-driven and vary from USD 1 400/kg to upwards of USD 50 000/kg [12]. This directly affects the cost per Watt of

installation of solar panels for SBSP, sitting directly on top of the cost of manufacturing. As such, much of the technologies developed in this body of work are done with the intention to lower the density and areal density (mass per unit area) of solar panels [13]. The mass per unit area then relates to the power generated per unit area of a cell to form another key metric: the specific power, or power generated per unit mass.

1.2. Lightweight Solar Panels for SBSP

1.2.1. Increasing Specific Power

In order to prioritize cutting down on the mass of space-based solar power, we must first review existing photovoltaic technology for space. Table 1.1. shows the specific power of various existing solar panels presently employed in space. We note areal densities of < 0.25 Wg^{-1}. However, these cells are all III-V cells which should average much higher specific powers. There is additional weight incurred in these cells that is causing a drop in specific power. This additional mass is coming from radiation shielding.

Work	Year	Absorber Layer	Specific power/ Wg^{-1}
US Naval Research Prototype [14]	2014	$GaInP_2$/InGaAs/Ge	0.0138
JAXA Solar Paddle PV [15]	2014	InGaP/GaAs/InGaAs	0.15
LISA-T Cubesat PV [16]	2016	InGaP/GaAs/InGaAs	0.25

Table 1.1. Specific powers of existing space-based photovoltaic cells.

Existing space-based photovoltaics require radiation shielding as there are a lot of high energy particles and radiation forming up the radiative background of space. For photovoltaics, the two most damaging types include high energy electron radiation and high energy proton radiation [17]. These forms of radiation are all capable of damaging a photovoltaic cell. There are several ways this is achieved. These charged particles could ionize the atoms in the device- stripping electrons from atoms in the bulk as these particles pass through, modifying doping concentration. They could also break chemical bonds between molecules in the devices, destroying the electronic properties they may have. They could also displace atoms in the crystal lattice of the electronics, creating defects that reduce the solar cell's ability to convert photons into an electric current. Finally, the deposition of high energy particles in a bulk causes collisions and energy transfer that simply thermalize the device, and excessive thermalization degraded photovoltaics [18]. As such, a considerable amount of mass budget must be spent on ensuring there is enough radiation shielding to prevent cells from degrading.

This amount of radiation shielding, practically speaking, ends up being very heavy. Consider Figure 1.3. which shows the mass breakdown of one of these cells. Per unit area, a thickness of at least 75µm each side is necessary to keep energetic particles from damaging the active layer in a 10-year cycle [17]. This translates to easily 86% of a cell's areal density, with only 15% being for the energy-generating layers of the cell itself. As such, there is a very large amount of mass savings that can potentially be incurred if one can design around reducing the amount of radiation shielding needed per unit area.

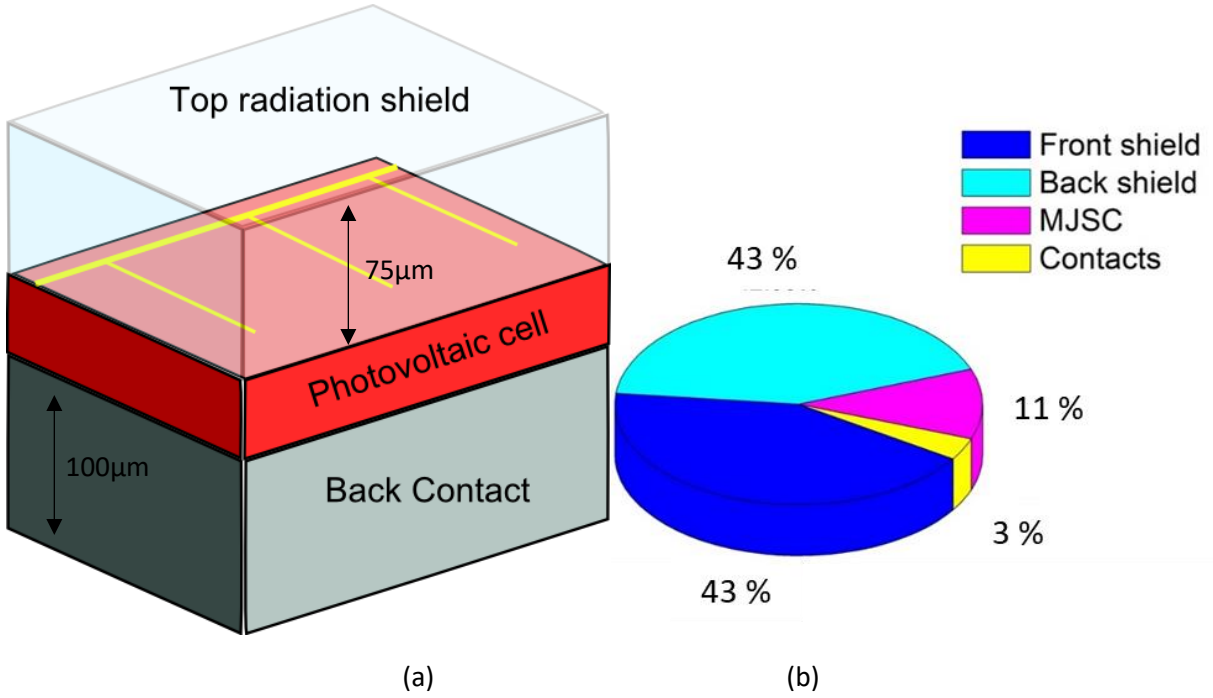

(a) (b)

Figure 1.3. Examining the mass density of existing space-based solar power. (a) A schematic of a solar cell to be used for SBSP and (b) the mass breakdown of such a cell.

In our body of work, this desire to reduce the amount of thick radiation shielding per unit area has manifested itself into two broad branches: concentrated photovoltaics and radiation-hard, shield-less flat panel photovoltaics. In this next section, we briefly go over the principles of these two types of technologies, as they give context for the body of work that will be reported in this thesis.

1.2.2 Concentrator Photovoltaics for SBSP

Our group has met reasonable success in increasing specific power of space-based photovoltaics by employing the principle of concentrated photovoltaics (CPV) [19]. The main goal of CPV is to use optical concentrators to increase the intensity of incident sunlight on the active photovoltaic cells, and also to reduce the active area occupied by said cells. Terrestrially, CPV has met with some degree of success with installations being commercially available [20]. There are various advantages to such a system. Fundamentally, increasing the intensity of incident light on a cell incurs theoretical increase in efficiency [21]. Furthermore, by reducing the amount of active photovoltaic material and replacing it with optical elements, the cost of production has an opportunity to be driven down. Finally, such a system can help us reduce the amount of thick radiation shielding used per unit area by replacing the amount of photovoltaic material needed per unit area. By increasing efficiency, reducing cost of production and reducing the amount of heavy shielding used per area, we see that CPV is an excellent candidate for increasing the specific power and reducing cost per Watt of installation for SBSP.

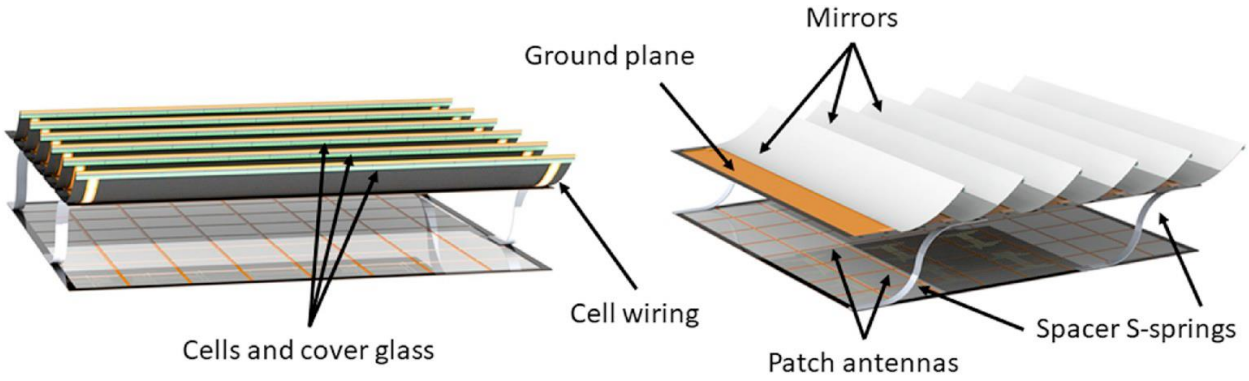

Figure 1.4. Schematic for proposed ultralight CPV for SBSP [19]. Used with permission. © 2019 Published by Elsevier Ltd on behalf of IAA.

The structure we developed is an array of parabolic mirrors as illustrated in Figure 1.4. The mirrors are arranged in a row with one in front of the other, and a strip of cells is stuck to the rear tip of each mirror. Incident sunlight is reflected off a mirror and thanks to its parabolic cross-sectional profile, this reflected light is concentrated onto the cells stuck to the rear of the mirror in front of it. Several key engineering questions had to be addressed in developing this this structure. First, the amount of concentrators versus the amount of cells used was considered to find the optimal power-to-weight ratio, and from there an ideal concentration band was decided upon to arrive at an ideal specific power. The ideal curvature of the mirrors and optimal placement of the cells were addressed via ray tracing. Through that study, the angular acceptance of incident light was accounted for and found to have an acceptance angle of 2.5° to 3.5° for concentration factors of 15x to 7.5x. Finally, a thermal management scheme was developed to ensure the high concentration of sunlight did not overheat the cells to the point where the cells degraded under excessive thermal load. This scheme, which is one of the subjects of our reported work here, briefly involves rapid conduction of heat away from the cell through the core of the mirror, followed by radiative emission through specialized coatings on both the backside as well as the mirrored frontside.

Through this study, our group was able to report a CPV structure with specific power of 4.1Wg^{-1}, which is ten times the specific power of existing flat panel SBSP and satisfies the minimum of 1 Wg^{-1} target that should be met for SBSP structures. By reducing the amount of area occupied by heavy radiation shielded cells with lightweight solar concentrators, the high specific power necessary for SBSP can easily be achieved.

1.2.3 Shield-less Flat Panel Photovoltaics for SBSP

Having successfully demonstrated how CPV can reduce the amount of radiation shielding used in photovoltaic structures for SBSP, we now seek potential avenues to improve our suite of SBSP technologies. While CPV offers many attractive advantages over flat panel photovoltaics, it has one key weakness, and that is the acceptance angle. As mentioned earlier, the high concentration factors could only be sustained over a small range of angles, less than 10°. Considering that our solar panels are supposed to be in orbit, this means that additional technologies must be developed to ensure that incident light will be within this range of acceptance angles. This proves logistically difficult. Obviously, acceptance angles are not so much of an issue with flat panel photovoltaics. However, the current dominant photovoltaic materials all experience radiation damage, and require heavy radiation shielding.

If there exist photovoltaic absorber materials that are radiation hard, surely we could make flat panel photovoltaics without the need for copious amounts of heavy radiation shielding per unit area.

In fact, we have several paths to achieve shield-less flat panel photovoltaics. At a base level, there are studies looking into reducing the absorber thickness and compensating with nanophotonic absorbers; these studies aim to increase radiation tolerance of existing III-V and Si solar cells by reducing the volume available for damage [22]. Simultaneously, various novel cell architectures are being explored. In particular, an array of nanowires of GaAs has been shown to also provide a fair amount of radiation hardness [23], offering a novel architectures for existing materials. Finally, there is the prospect of searching for intrinsically radiation hard absorber materials. Several new photovoltaic materials have been shown to demonstrate radiation resistance against electron and protons found in the Earth's orbit [24], offering exciting opportunities to incorporate new absorber layers into existing architectures.

Generically speaking, the elimination of the radiation shield will result in very high specific power. Most thin film solar panels have an active area of 500-700nm. Assuming a fairly heavy GaAs density of 5.23 g cm^{-3}, this translates to an areal density of 2.616 gm^{-2}. Assuming a reasonable efficiency of 17% under AM0 illumination of intensity 1.37 kWm^{-2}, a theoretical ceiling of over 100 Wg^{-1} specific power is available to us. Realistically, of course, some substrate an encapsulation is usually still necessary for support. Suppose then a reasonable flexible thin film support comprising 7µm of polyimide with density 1.42 gcm^{-3} on each side adding an extra 19.88 gm-2. The specific power of such a slightly more realistic average of 10.1 Wg^{-1}. In fact, this specific power has already been demonstrated in terrestrially flown flexible perovskite solar cells [25], making shield-less, radiation resistant, flexible flat panel photovoltaics not only exciting for SBSP, but also very achievable.

1.3. Thesis Outline

With our design space set up, we now briefly describe the topics that will be covered in this body of work. In Chapter 2, we will report the design, simulation, fabrication, and characterization of lightweight, thermally emissive optical coatings necessary for sustaining ideal operating temperatures of the earlier described space-based concentrated photovoltaics. In Chapter 3, we consider a potentially radiation hard photovoltaic absorber material known as organo-lead halide perovskites, its properties and challenges presented in fabricating such a material. In Chapter 4, we expand our investigation into this family of materials by subjecting them to actual proton irradiation with the intention of characterizing how proton degradation and recovery might occur. Summarily, this thesis is thus on the development of lightweight photovoltaic technologies, both concentrated and flat panel, for SBSP.

Chapter 2: Infrared Cooling Coating for Space-Based Solar Power

2.1. The Need for Radiative Cooling in SBSP

2.1.1. Heat Generation in Photovoltaic Devices

Heat is a core property of every body in this universe, and maintaining it within a specific window is crucial to retaining the desired properties a body possesses. Failure to do so will often result in undesired physical and electrical properties, a phase change, or worse, a chemical change, altering the structure and makeup of a body and thus its properties. As such, the flow of heat into and out of a body is a subject of important study as long as that body exists in our reality. We will find this especially true in the study of photovoltaics, where higher temperatures degrade the cell in various ways such as lowering V_{oc} [26] and resulting in critical failure above a certain temperature [27]. In this section, we will discuss the implications of heat accumulation and methods of heat dissipation in the context of space solar photovoltaics as executed by our team.

The generation of waste heat is a fundamental and inevitable phenomenon during the operation of a solar cell. Consider the photovoltaic effect illustrated in Figure 2.1. below [28]. Here we see incident on a semiconductor, represented by its band diagram. As long as the incident photon has more energy than the band gap, it will excite an electron in the valence band, promoting it into the conduction band, whereupon it becomes very mobile and able to be extracted as useful electric energy. However, the full energy of the photon is rarely captured, as many thermalization losses occur between excitation and carrier extraction. An excited electron will thermalize until it reaches the edge of the conduction band if the photon has more energy than the band gap. Some energy is lost simply by the charge carries traversing through a resistive medium, causing Joule Heating. Furthermore, there will always be some electron-hole pairs the recombine nonradiatively, losing energy by thermalizing the bulk, or they may be trapped by surface defects, causing similar thermalization. Finally, simply by being collected by the electrodes, a potential drop is experienced by the carriers, causing further thermalization. Incident illumination will always cause a solar cell to heat up, and since heat degrades a cell, we must consider ways to manage this heat accumulation.

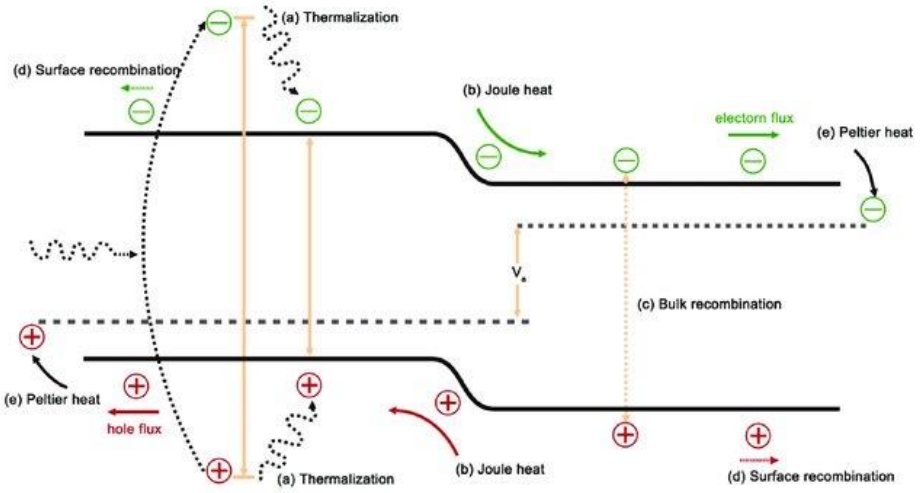

Figure 2.1. Schematic showing avenues for heat generation during the photovoltaic process [28]. Used with permission. © 2016 WILEY‐VCH Verlag GmbH & Co. KGaA, Weinheim.

2.1.2. Thermal Regulation Methods for Space-Based Photovoltaic Devices

The generation of heat within in solar cell, as well as its detrimental impact to the operation of the cell, have been explored. We now consider avenues through which heat may be transferred to and from a solar cell in space; seeking to quantify the rate of these heat flows. Through this study, we establish a heat management profile through which we may keep our extraterrestrial solar cells operating within a desired temperature range for a sustained lifetime.

Thermodynamically speaking, heat spontaneously flows from a hotter body to a colder body unless external work is performed on the system. There are three general avenues through which heat may spontaneously flow in this manner: conduction, convection and radiation. Conduction occurs when there is a temperature differential across a continuum: heat will flow from a warmer body to a colder body via conduction only if there is continuous matter between them, and heat is carried via the vibration of the particles in this continuum. Convection occurs when a body is surrounded by a moving fluid of a different temperature. Radiation is the transfer of heat from a warmer body to a colder body via the emission and absorption of thermal radiation, which is capable of propagating through media that are transparent to it. For a body enveloped in the vacuum of space, it is clear that the only avenue for heat flow out of a body is via radiation. As such, let us consider the flow of radiation into and out of the body in order to find a viable path for dissipation of excess heat.

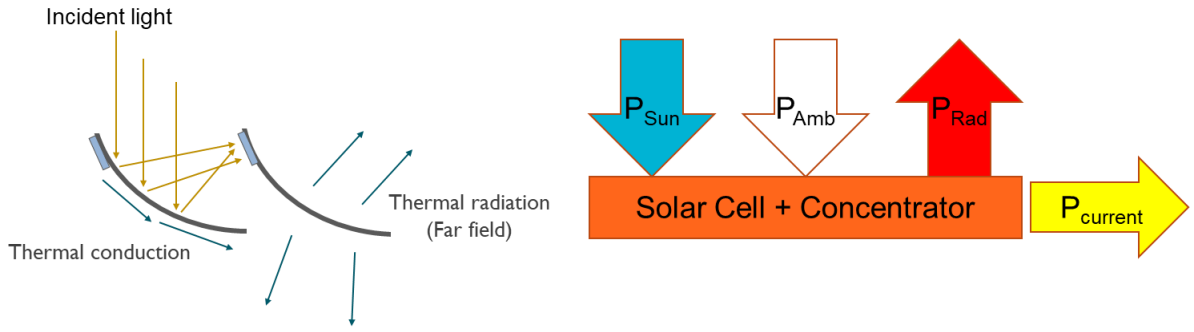

Figure 2.2. (a) Schematic depicting flow of energy across the concentrators, simplified in (b) where overall fluxes into and out of a concentrator are explored in a simplified diagram.

Let us contextualize our discussion thus far in terms of space solar photovoltaics by considering our parabolic concentrator array. As depicted in Figure 2.2. (a), light incident on a parabolic concentrator will be concentrated a spot on the back of the next concentrator, where the cell will be. Generalizing the earlier modes of heat generation into Figure 2.2 (b), one may say that through the cell's operation, some of this sunlight will be converted into useful, extracted electrical energy while the rest is retained in the cell and mirror structure as heat. Heat will flow from the cell to the rest of the concentrator via conduction. The front and back surfaces of the concentrator then exchange thermal radiative energy with the ambient surroundings, which in this case we may assume to be the vacuum of space which takes the form of a 3K blackbody. It will emit electromagnetic radiation as a blackbody under Planck's Law, scaled by the surface emissivity of each side, and absorb radiation from the ambient 3K blackbody, scaled by the surface absorptivity on each side. We may describe these fluxes of energy with the following equations:

$$P_{Net} = P_{Rad}(T_{Rad}) - P_{Amb}(T_{Amb}) - [P_{Sun} - P_{Current}] \quad 2.1$$

$$P_{Rad}(T_{Rad}) = P_{Rad,Front}(T_{Rad}) + P_{Rad,Back}(T_{Rad}) \quad 2.2$$

$$P_{Rad,Front}(T_{Rad}) = A \int d\Omega \int d\lambda \, I_{BB}(\lambda, T_{Rad}) \varepsilon_{Front}(\lambda, \Omega) = A \varepsilon_{Front} \sigma {T_{Rad}}^4 \quad 2.3$$

$$P_{Rad,Back}(T_{Rad}) = A \int d\Omega \int d\lambda \, I_{BB}(\lambda, T_{Rad}) \varepsilon_{Back}(\lambda, \Omega) = A \varepsilon_{Back} \sigma {T_{Rad}}^4 \quad 2.4$$

$$P_{Amb}(T_{Amb}) = A(\alpha_{Front} + \alpha_{Back}) \sigma {T_{Amb}}^4 \quad 2.5$$

where P_{Rad}, P_{Amb}, P_{Sun} and $P_{Current}$ are the flow of power out of the concentrator as radiation, into the concentrator from the ambient 3K blackbody, into the concentrator from the sun, and out of the concentrators as useful electrical energy, respectively. P_{Net} details the net flow of power into or out of the concentrator. T_{Rad} and T_{Amb} are the temperatures of the concentrator and the ambient vacuum of space. A is the area of either side of the mirror. Ω is the hemispherical solid angle a unit area of each side of the mirror will emit radiation to. IBB is the emission intensity of electromagnetic radiation with wavelength λ emitted by a perfect blackbody at temperature T_{Rad} under Planck's Law, ε and α represent the emissivity and absorptivity of each sides of the mirror and σ is the Stepan-Boltzmann constant.

Through this heat flow profile, the solar cell and mirror ensemble will reach a steady state temperature profile, where the extracted electrical energy and emitted radiative energy become large enough to equal the energy absorbed from the sun and the ambient 4K environment. At this steady state, P_{net} equals zero, allowing P_{Rad} to become a function of P_{Sun}, P_{Amb} and $P_{Current}$. Let us first assume P_{Sun} and $P_{Current}$ to be constant and neglect P_{Amb} as at 3K, it is very small. This leaves us with an equation whose variables are T_{mirror}, ε_{Front} and ε_{Back} like so:

$$A(\varepsilon_{Front} + \varepsilon_{Back}) \sigma {T_{Rad}}^4 = P_{Sun} - P_{Current} \, . \quad 2.6$$

In other words, for a given amount of solar concentration, the steady-state operating temperature of the mirror and the solar cell will be a function of the frontside and backside emissivity of the parabolic mirror. In order to keep the solar cell cool enough to operate without degradation, it is the thermal emissivity of the concentrator's surfaces we must focus our efforts on. We may do so by employing optical coatings on both sides of these concentrators that can emit large amounts of thermal radiation. This affords us control over the amount of radiation being emitted from the surfaces.

2.1.3 Emissive Coating Properties

Let us thus consider the design limitations when attempting to design optical coatings to maximize the emissivities of the fronside and the backside of the concentrators. First off, as with the rest of these space-based structures, the coatings must be thin and thus lightweight to minimize impact on launch costs. Also, the coatings must be resistant to high energy proton and electron radiation present in space. In addition, an important design restriction to keep in mind will be scalability- the mirrored surfaces are on the order of 10 cm^2 and as such it will be important for these coatings to be uniform on that order magnitude as well.

The window of the electromagnetic spectrum in which these coatings are highly emissive is perhaps the most important consideration. We note from equations 2.3 and 2.4 how the final radiative outflow of power is a product of the blackbody emission intensity at temperature T and wavelength λ as well as how emissive it is at that wavelength. Let us explore Planck's law of blackbody emission as stated in equation.

At different temperatures, a black body is most emissive at different windows of the electromagnetic spectrum. In other words, it becomes important to design the spectral emissivity of the coatings to maximize emission within the window that the concentrator is expected to emit at once it has reached its operating temperature. Aiming to achieve an operating temperature of less that 370K, the wavelength range of interest is from 5µm to 30µm, known as the mid infrared (mIR) regime.

$$I_{BB}(\lambda, T) = \frac{2hf^3}{c^2} \cdot \frac{1}{\exp\left({}^{hf}/_{k_B T}\right)-1} = \frac{2hc^2}{\lambda^5} \cdot \frac{1}{\exp\left({}^{hc}/_{\lambda k_B T}\right)-1} \ . \qquad 2.7$$

Finally, the last consideration concerns the frontside coating. This side is a mirror surface that must be highly reflective in the visible regime of 300nm to 900nm in order to reflect the useful electromagnetic radiation from the sun onto the solar cell, but otherwise desires to be highly emissive in the wavelength regime immediately after that. This calls for broadband frequency selectivity that we will investigate in greater depth as we design the frontside coating.

Let us now report the calculations of a colleague in a previous work [19] where we predict the emissivities each coating needs to achieve via thermal simulations. This is done pre-emptively under the assumption that achieving the broadband frequency selectivity for the frontside is a nontrivial problem. Here we consider a 15 Sun concentration on our cell, and vary the thickness of the mechanical core of the mirror, made of carbon fibre reinforced plastic (CFRP) the backside emitter emissivity and the mirror emissivity. Figure 2.3. summarizes the optimization plots. Specifically, at a backside emissivity of 0.88 and a frontside emissivity of 0.4-0.6, an equilibrium temperature of < 80C may be achieved.

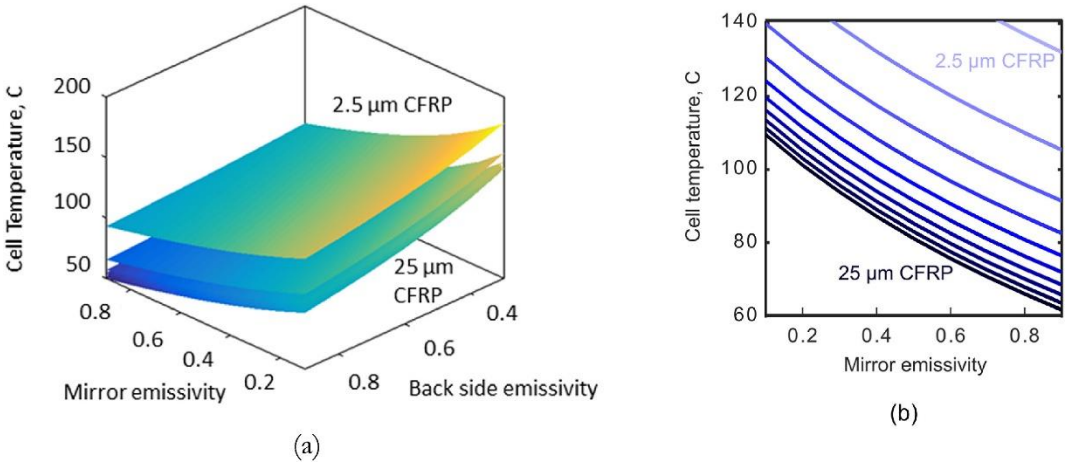

Figure 2.3. Thermal simulations predicting (a) equilibrium temperature as thickness, frontside mirror emissivity and backside emissivity varies and (b) when backside emissivity is fixed to 0.88 [19]. Used with permission. © 2019 Published by Elsevier Ltd on behalf of IAA.

With these parameters defined, we will, for the rest of this chapter, report two bodies of work, one published [29], and one presently under review, where we optimize the frontside and backside emitters and fabricate these structures on centimetre scales.

2.2. Design and Simulation of Thermal Coatings

2.2.1 The Salisbury Screen

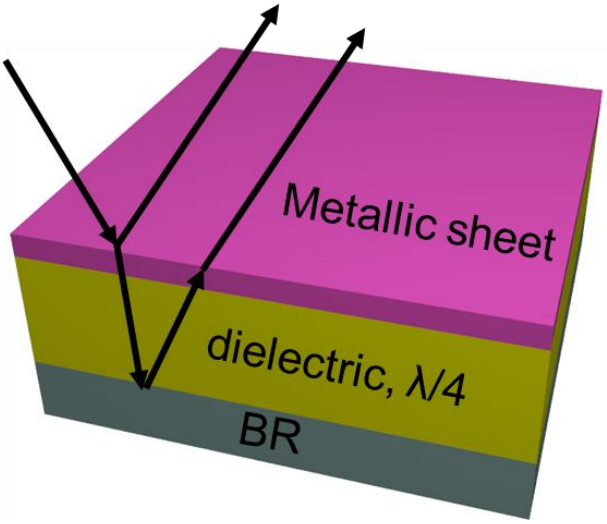

Figure 2.4. Schematic depicting the operation of a Salisbury screen. Note how the zeroth order and first order reflections will interfere with each other.

Let us quickly discuss the basic principle of the Salisbury screen whose structure we aim to employ for these coatings. A Salisbury screen, as shown in Figure 2.4., consists of three layers: a thick back reflector made of metal at the bottom, a middle dielectric spacer whose thickness is on the order magnitude of the wavelength regime we are operating in, and a topside thin metallic sheet [30]. When incident light falls on the Salisbury screen, the thin metallic sheet will reflect some of the light but allow another portion of it to propagate through it without absorbing it all. This allows a strong enough signal to travel a path length equal to twice the thickness of the dielectric layer. If the dielectric layer is a quarter of the wavelength of the incident light, after being reflected by the back reflector and reaching the metallic sheet as a first order reflection, it would have travelled half a wavelength and be exactly out of phase with the zeroth order incident light. The resulting destructive interference drastically reduces the amount of reflected light at that wavelength, meaning the coating is highly absorptive of light of that wavelength. By Kirckchoff's Law, we then state that at steady state, since a body is as absorptive as it is emissive, it will be very emissive of light of that wavelength as well. In this manner, we can engineer coatings that are highly emissive in the mIR by varying the dielectric thickness. While this resonance effect sounds at first like a narrow band effect that occurs at a specific wavelength, it has in fact reported to be fairly broadband [31]. Being lightweight and easy to fabricate, it offers many advantages over existing thermally emissive surfaces [32], [33], [34] such as easy large-scale fabrication, low fabrication cost, and launch cost.

2.2.2. Backside Coating Optimization

We begin by considering the backside coating, which has less demands than the frontside, Sun-facing coating, as it only needs to be emissive in the IR spectrum but not the visible spectrum, so we can first focus more on IR spectrum emissivity without having to factor in visible spectrum reflectivity, restricting the number of degrees of freedom to contend with in the initial design of Salisbury screens. Consider the topside layer of thin conducting material (hereafter referred to as the top conductor). For the backside coating, the role of the top conductor is thus: first, it must reflect some of the IR radiation that strikes its

surface as part of its zeroth order reflection. Second, it must allow enough IR radiation to transmit through it and into the dielectric layer for the interference effects to occur. In other words, we desire it to be equally reflective and transmissive, from a qualitative perspective. Consider the equations governing reflection and transmission at zero degree incidence as a function of optical constants as written below.

$$I = I_0(-4\pi kz\lambda) \quad 2.8$$

$$R = \left|\frac{n_1 - n_2}{n_1 + n_2}\right|^2 \quad 2.9$$

where I is intensity after transmission, I_0 is intensity before transmission, z is the thickness of the medium, n and k are the real and imaginary components of a material's refractive index, respectively. With n_1 being 1 for a vacuum. As we desire the top conductor to reflect about half the incident radiation and transmit the other half, we thus seek conductors with low damping constant k and desire to make it as thin as possible.

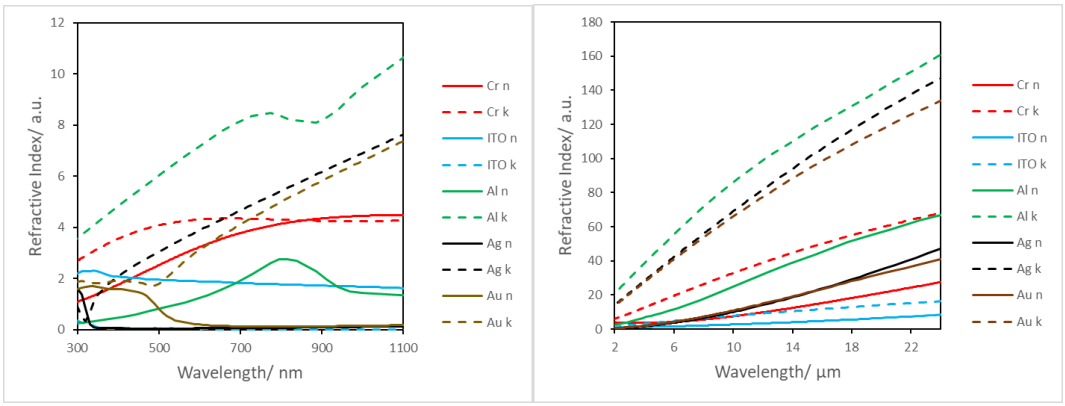

(a) (b)

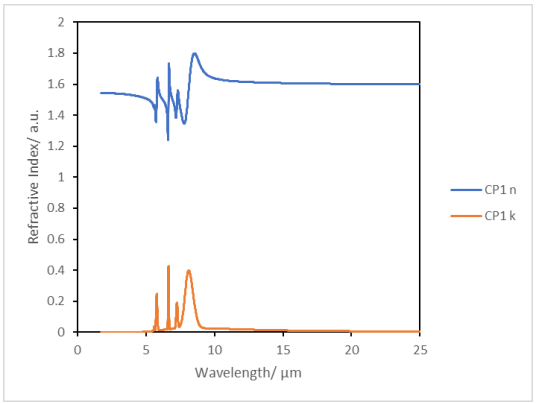

(c)

Figure 2.5. Refractive indices of (a) potential top conductors in the visible regime, (b) potential top conductors in the mIR regime, and (c) the CP1 dielectric spacer layer. Optical data of Cr, Al, Ag, and Au taken from refs [35], [36], [37], [38].

Consider then Figure 2.5. (a) and (b) that plots the visible and mIR refractive indices of various common conductors such as chromium, ITO, aluminium, silver and gold. Chromium immediately stands out as a material that fits our desired parameters. We will choose this material, but for illustrative purposes consider also aluminium in our initial calculations.

For our dielectric spacer layer as well as our bottom reflector, selecting a material is easier. The dielectric spacer layer must be radiation resistant and have an easily controlled thickness in the micron scale, as a quarter of the wavelength of radiation in the mIR falls around 5 μm. For this purpose, we have chosen the space-ready polymer CP1 from NeXolve [39], a polymer we have previously used in prototyping. We have measured its refractive index via ellipsometry and report both its visible and mIR refractive indices in Figure 2.5. (c). We will vary its thickness via spincoating. As for bottom reflector, we simply desire as reflective a surface as possible, and thus chose aluminium that was easy to evaporate.

With our materials selected, we endeavour to perform simulations to optimize our coatings. Being primarily a 1-dimensional stack homogenous in the in-plane directions, we seek to vary the thicknesses of the top conductor as well as the middle dielectric spacer layer, finding the mIR absorptivity at each thickness by integrating the spectral absorptivity at each wavelength using the formula in Equation 2.10 below. After reviewing various methods available at our disposal, we decided to employ the rigorous coupled wave analysis (RCWA). While the transfer matrix method (TMM) and the finite domain time dependant (FDTD) method are all excellent methods for modelling 1D stacks, we found the RCWA most suitable for our dimensions which included elements on the order of both nanometres and micrometres. In addition, we eventually wish to consider the absorptivity of patterned surfaces which the RCWA is a little better suited to handle than the TMM. We selected the RETICOLO RCWA code [40].

$$\varepsilon_{mIR} = \frac{\int_{5\mu m}^{30\mu m} \epsilon_{Spectral}(\lambda) * I_{BB}(\lambda) d\lambda}{\int_{5\mu m}^{30\mu m} I_{BB}(\lambda) d\lambda} \qquad 2.10$$

In Figure 2.6., we present the results of our optimization calculations. We present top conductor/ dielectric/ backreflector coatings of Cr/ CP1/ Al and Al/ CP1/ Al, wherein we sweep the thicknesses of Cr and CP1, and Al and CP1, respectively, recording the mIR absorptivity of each thickness combinations in the heatmap plots seen in Figure 2.6 (a) and (b). The importance of choosing the material of the top conductor is immediate. Already, we see that in order to achieve the Fabry-Perot effect necessary for absorptivities of above 40% across the mIR spectrum, the top conductor must be on the order of nanometers. Furthermore, as predicted earlier, should the top conductor be too reflective and too attenuative, as is the case in the Al/ CP1/ Al structure, the optimal Al thickness ends up being so thin that it is less than 0.5nm, which is difficult to achieve as this means we must conformally coat a cm^2 scale area with a film of Al that is 2-5 atoms thick, with the slightest deviation drastically altering the surface's absorptivity and emissivity parameters. Clearly, it is more feasible to work with the Cr/ CP1/ Ag structure where we find ourselves comfortably able to work in a Cr film thickness of 2-5nm and still achieve above 0.5 absorptivity across the mIR spectrum.

Another point of insight lies in how as both Cr and Al thicknesses are varied, we note a thickness at which a maximum amount of emissivity/absorptivity is observed. Thicker or thinner than this and the coating simply is not as emissive. Qualitatively this makes sense if one considers the phenomena by which the coating absorbs light. Enough first order, out-of-phase reflected light must be allowed to propagate through the thin metal layer and the dielectric medium to maximally interfere and completely cancel with

the zeroth order reflection. If this layer is too thin, too much first order reflected light will interfere with the zeroth order reflection, resulting in excess first order reflection. If the layer is too thick, too little first order reflected light exits and is unable to completely interfere with the zeroth order reflection, resulting in excess zeroth order reflection. There is an optimal amount of top metal that must be determined for maximal emissivity.

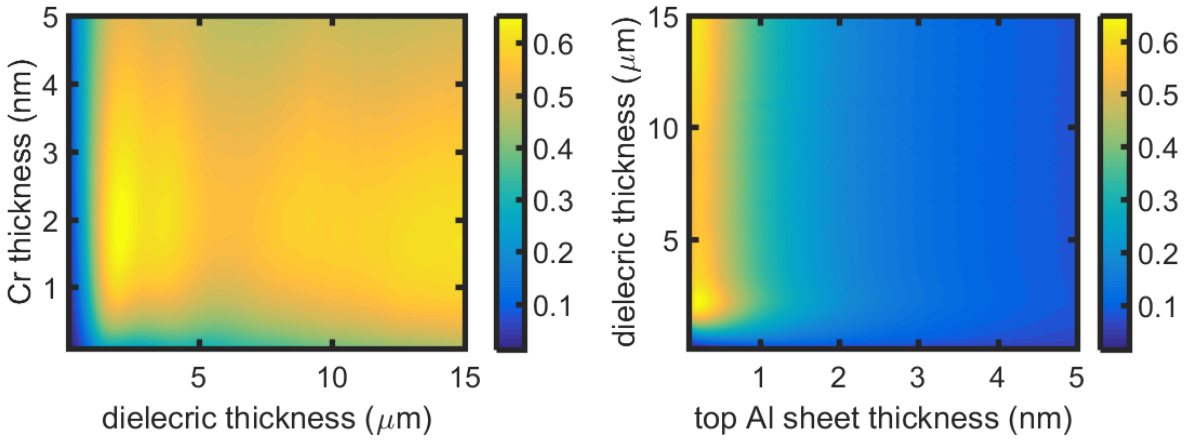

Figure 2.6. Optimization heat maps of (a) a Cr/CP1/Al coating AND (B) AN Al/CP1/Al coating, sweeping topside conductor (Cr, Al) thickness and CP1 dielectric thickness.

Looking at the variation of the absorptivity with dielectric thickness in the Cr/ CP1/ Ag structure in Figure 2.6. (a), we note about three thicknesses at which maxima absorptivity across the mIR spectrum is achieved: one at 2µm, one at about 4µm and a final peak beyond 15µm. The multiple maxima observed can be attributed to that fact that we seek to leverage an interference effect. Given that we desire a λ/2 path difference to create maximum destructive interference, it makes sense for the maxima to be also observed at about twice and quadruple the initial maxima as well. In a more practical context however, the final thickness we desire is 2µm. By performing a rudimentary thickness sweep, we have found maximum absorptivity as a Cr thickness of 2nm and a CP1 thickness of 2µm.

However, we find this mIR emissivity of 0.6 insufficient for the backside emitter using the heat calculations performed earlier in Section 2.1.3. In this next section we explore some potential structures that build on this solid initial 0.6 emissivity. To first order, when considering such a coating, a logical next step would be to add a second layer of topside conductor and middle dielectric. On principle, one would easily posit that this would create three different path lengths for the anti-resonant condition to be met, increasing the broadband nature of the absorption.

To maximize the emissivity of the proposed double-layered Salisbury screen, we perform similar multivariable optimization calculations for the following structure: Cr/ CP1/ Cr/ CP1/ Al, this time varying the thicknesses of all layers except Al. Sweeping across four parameters is difficult to visualize and also time-consuming, however, a maxima of 0.8 was found to be at 0.5nm Cr/ 1.9µm CP1/ 3nm Cr/ 2µm CP1/ 500nm Al. The schematics of the two coatings we developed are illustrated in Figure 2.7.

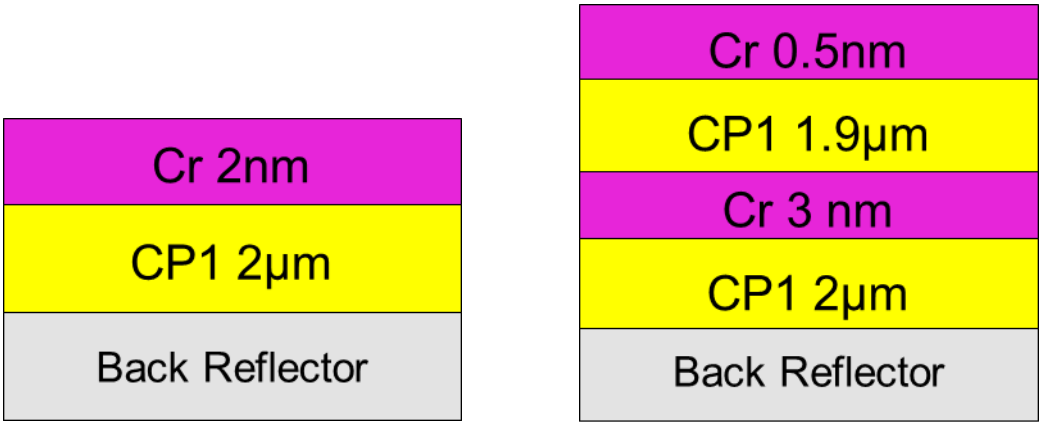

(a) (b)

Figure 2.7. Final Thicknesses of (a) 1-layer Cr coating and (b) 2-layer Cr coating.

2.2.3. Sun-facing Coating Optimization

With some success in designing the highly emissive backside emitter under our wing, we now turn our attention to the Sun-facing emitter. As mentioned earlier, the frontside emitter needs to be emissive in the mIR spectrum, but simultaneously highly reflective in the visible spectrum in order for the frontside coating to be able to perform its job of reflecting and concentrating visible spectrum light onto the cell on the next mirror. The bottom reflector needs to continue to be silver in order to achieve this goal, while the middle dielectric layer needs to retain its thickness in order to continue being lightweight enough for space applications and also harness the Salisbury screen effect. This means our degree of freedom lies in the topside thin conductor layer. Let us consider how some different materials behave optically in both the mIR and visible spectrum in order to reach a suitable Salisbury screen that can act as the frontside emitter.

Consider the differences between n and k refractive indices between Cr and ITO as show in Figures 2.5. (a) and (b). Broadly speaking, k will describe attenuation of light travelling through the medium while n is factored into reflection at the media boundaries. If n and k are low, the material is essentially transparent. For our topside reflector, in the visible spectrum, we desire light to interact as little with the thin conductor layer and the dielectric medium, so that it may be reflected off the bottom metal reflector with as little attenuation and interference as possible. We will soon see that any reflectivity in the thin metal layer creates interference that reduces visible reflectivity. This makes materials like ITO a better choice than Cr as they are mostly transparent in the visible regime, while still having similar optical properties to Cr in the IR regime. We chose ITO as it is fairly easy to sputter, giving us good control over its thickness and in turn the final optical properties of our topside reflector. Furthermore, as we will establish later, this thickness of ITO is fairly radiation-resistance, thus suitable for our purposes as a space-based thermally emissive coating.

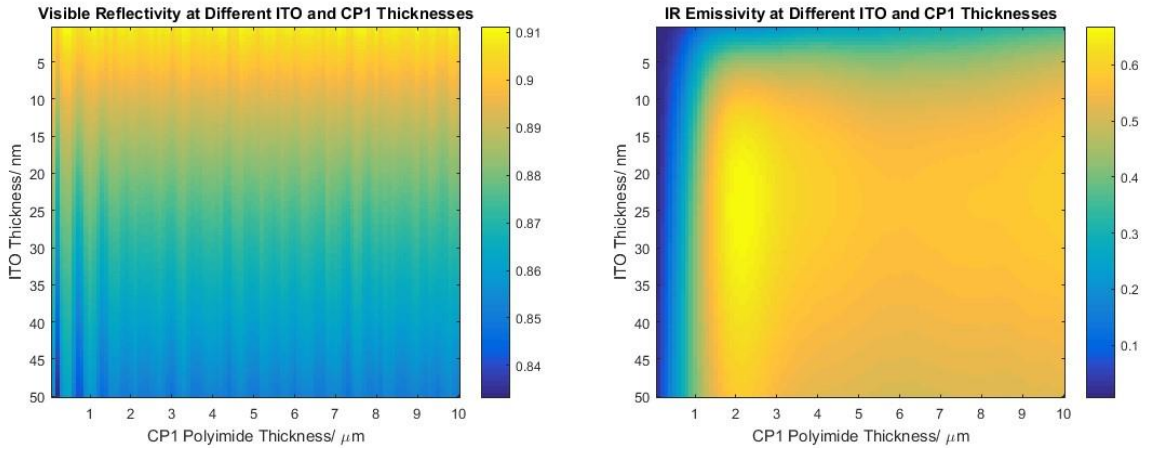

(a) (b)

Figure 2.8. Heat maps showing the variation of (a) visible reflectivity and (b) mIR absorptivity with ITO and CP1 thicknesses.

We now perform a similar optimization as we did in the earlier coating, sweeping across various CP1 and ITO thicknesses and looking at the visible reflectivity and the IR absorptivity/emissivity. This time around, in addition to maximizing IR emissivity, we must do so while paying maximizing visible spectrum reflectivity. Thankfully, from our earlier study, we know our frontside can have a mIR emissivity of 0.4 to 0.6 thanks to our backside emitter, allowing us to prioritize the visible spectrum reflectivity. Figure X plots the heat plots of these two optimization sweeps. We note a general similarity in the heat maps of the mIR emissivity in Figures 2.6. (a) and 2.8. (b). This is because Cr and ITO exhibit similar optical properties in the mIR, as seen in the n and k spectra in Figure 2.5. (b).

We consider how visible reflectivity and mIR emissivity vary with ITO thickness. From the visible spectrum heatmap in Figure 2.8. (a), we note that the coating gets less reflective in the visible as ITO thickness increases, indicating that even fairly transparent ITO attenuates light considerably at thicknesses greater than 25nm. This time round, in addition to optimizing the top conductor layer to be maximally emissive in the mIR, we must still ensure it is thin enough for the coating to be reflective in the visible. Contextualized in the case of our parabolic solar concentrators, we wish for at best a loss of 10% of reflected light and as such desire an ITO thickness of 10-15nm.

Sweeping across the thickness of the CP1 we once again find the optimal thickness around 2μm for maximum mIR emissivity. Turning to the visible spectrum heatmap, at every ITO thickness, we see fluctuating trends in the mIR emissivity as CP1 thickness increases, with regular, periodic maxima and minima in emissivity. Much like the phenomena observed in the mIR described in the earlier section, this occurs due to different resonant conditions being met at every CP1 thickness. Only now, resonant conditions are being met at much shorter thickness intervals because the wavelength of visible light is much shorter than the CP1 thickness, thus a small increase in thickness will quickly cause a flip in the λ/2 condition from being mostly destructive to mostly constructive. Numerically, for light of wavelength 300-900nm, a shift in 100-200nm thickness in CP1 will change the interference condition as that represents an extra λ/4 thickness.

We also see why our top conductor was chosen to be ITO and not a more reflective material like Cr. As established earlier, the refractive indices of ITO are low in the visible spectrum, and as such there is very little zeroth order reflection present for destructive interference to occur, maximizing reflection via first order reflection. While we just described the reflectivity to be sensitive to CP1 thickness from a scientific perspective, from an engineering perspective we note that this translates to a fluctuation in reflectivity of about 2% for a given thickness of ITO. Were a more reflective material chosen for the top conductor, more zeroth order reflection would be present to destructively interfere with the first order reflection, reducing visible spectrum reflectivity. We thus see exactly why we desired a top conductor material that was transparent in the visible and lossy in the mIR.

Figure 2.9. illustrates the schematic of the final structure optimized, as well as the thicknesses.

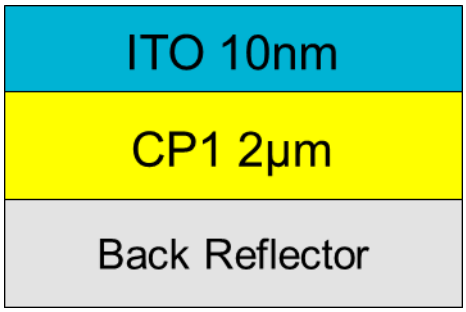

Figure 2.9. Schematic illustrating optimized thicknesses of the mirror ITO coating.

2.2.4. Electric Field Profile

So far through this study, we have concerned ourselves with optimizing for mIR emissivity and visible spectrum reflectivity, spending some effort to consider how a material's refractive indices and thicknesses affect the light propagation and interference conditions. However, what has not quite been addressed is the broadband nature of the light absorption. We thus endeavour to more deeply analyse the absorption of light at each layer, as well as the electric field profile of different wavelengths of light in these layers. These two studies will give us deeper insights into exact nature of broadband absorption of Salisbury screens.

Consider Figure 2.10. which plots for our three coatings the absorption (and thus emission) of mIR radiation at each layer. No matter how many layers, and no matter the material chosen for the top reflector, we note some similarities. The general trend is that CP1 is very absorptive within a window from 5-10 μm; exhibiting narrowband, highly resonant absorption. We understand this to be due to absorptive nature of CP1, attributable to its polymeric nature- organic materials tend to have an IR fingerprint due to the organic bonds being resonant at these wavelengths. We can see this being expressed in the refractive indices of CP1 as shown in Figure X. On the other hand, for single layer coatings, the top conductor layer expresses absorptivity in two regimes: a series of narrowband resonances in the 2-5 μm regime, and a broadband resonance in the 10-30 μm regime. We understand this to be a series of the anti-resonant effects occurring at wavelengths whose wavelengths satisfy the condition $t = (n + ½)\ \lambda/2$.

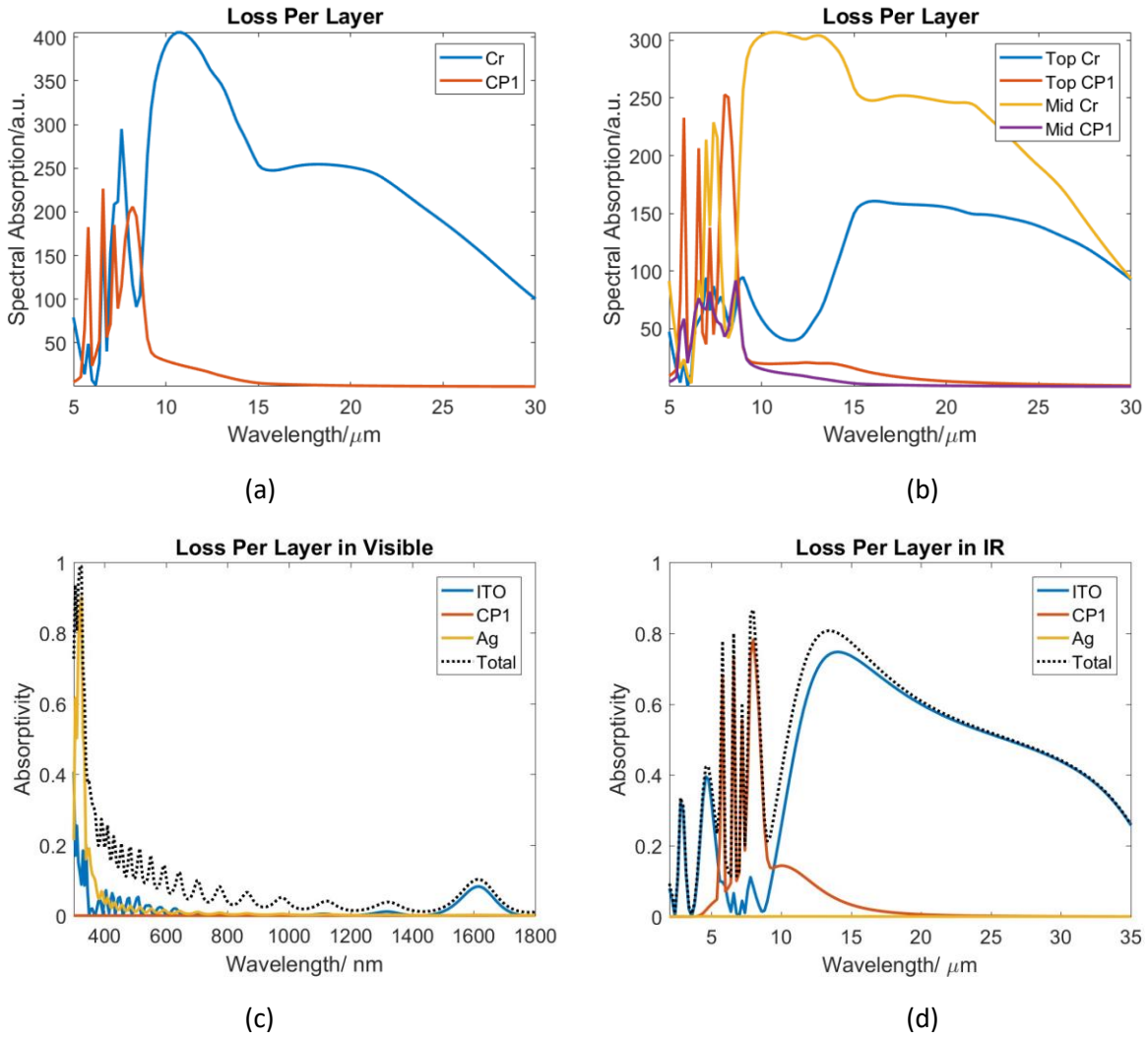

Figure 2.10. Spectral optical loss due to each layer, in arbitrary units, from (a) the single layer back Cr coating, (b) the double layer back Cr coating, (c) the fronside ITO mirror coating in the visible spectrum, and (d) the frontside ITO mirror coating in the mIR spectrum.

In the two-layer Cr coating, we see a tandem effect, and one we were hoping would be expressed in this design. We see the middle Cr layer be responsible for the 10-15 µm broadband absorption, but we also see both the middle and the top Cr layer be responsible for the 15-30 µm broadband absorption. By adding a second layer we desired to create more anti-resonant modes to allow for more emissivity and we see this being expressed when we break down the absorption per layer.

Looking to the loss per layer breakdown of the ITO in Figures 2.10. (c) and (d), we once again see that even with the slightest bit of reflectivity, simply due to the fact that ITO is a different material from the void of space and CP1, some interference occurs. We will soon see that our selection of ITO has been a good one, however it is nonetheless important to keep in mind that even with this level of frequency selectivity creating an essentially mirror coating in the visible, interference is still intrinsic to a film with this structure.

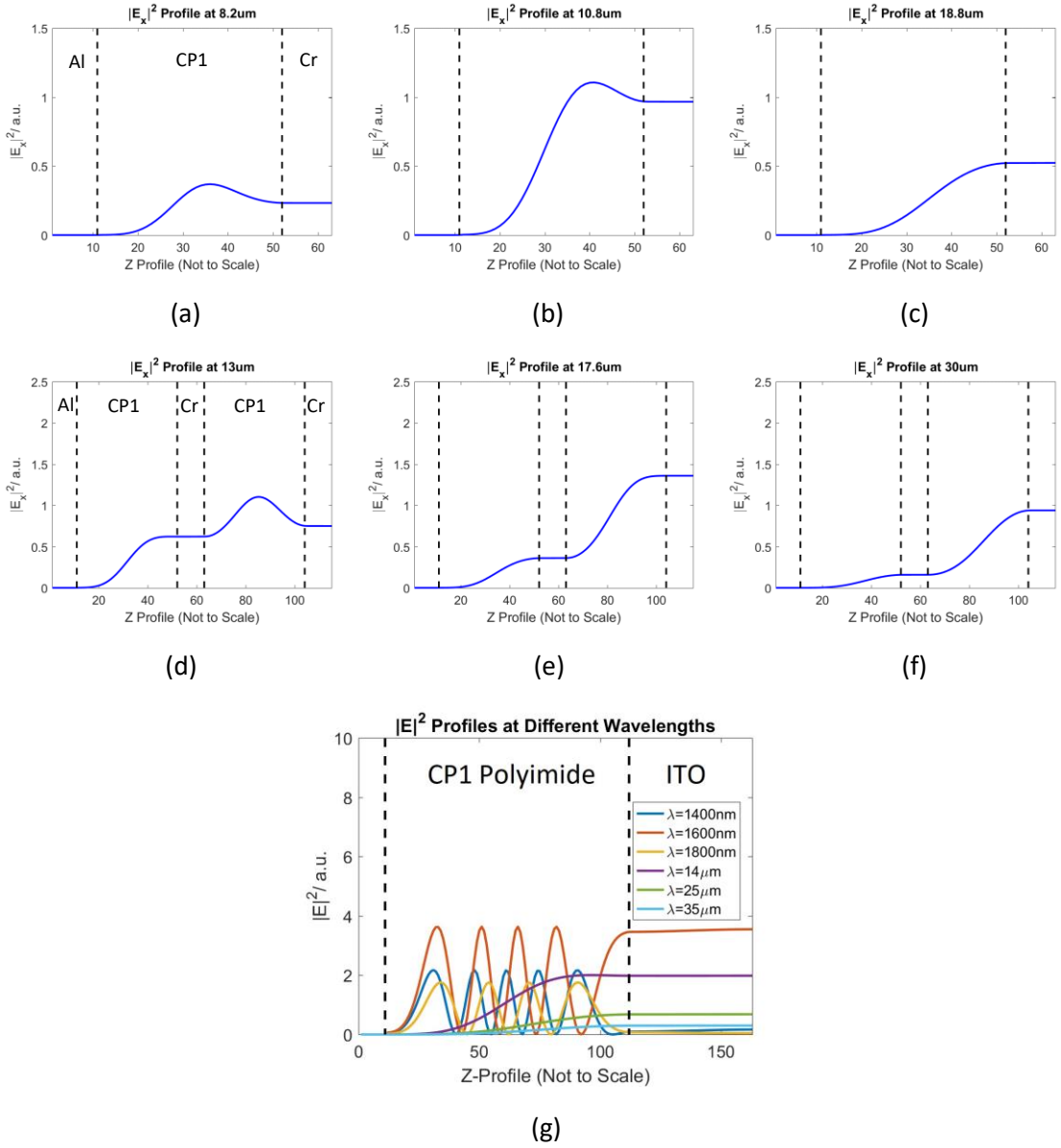

Figure 2.11. $|E|^2$ profiles of (a) single layer Cr, 8.2µm, (b) single layer Cr, 10.8µm, (c) single layer Cr, 18.8µm, (d) double layer Cr, 13µm, (e) double layer Cr, 17.6µm, (f) double layer Cr, 30µm, and (g) ITO coating at various wavelengths.

Let us now consider the steady state electric field intensity profile of light of different wavelengths that form in these films. This gives us a good understanding at the sort of standing waves and anti-resonant conditions that would be met, as light is an electromagnetic wave. Figures 2.9. shows the electric field intensity distribution across various coatings. The depth profile on the x axis is not to scale to better visualize the differences between all three layers, and progresses from the backreflector, then the dielectric spacer, then the top conductors, with the dotted lines representing boundaries between the three media. Note that no further calculations were necessary beyond the base RCWA as the electric and magnetic fields at steady state are indeed what the RCWA method calculates.

Figures 2.11. (a)-(c) plot the profiles found in the single layer Cr backside coating. The profile of three different wavelengths are sampled: a sub 10 μm wavelength, where we would expect a reflective mode, and two wavelengths greater than 10 μm where according to the simulated spectrum in Figure X, we would expect a broadband emissive mode. The key distinguishing property between the reflective mode and the broadband emissive mode is that the profile reflective mode displays a resonant mode with one wavelength worth of standing waves set up at steady state. We can tell this because at the CP1/Cr interface, there is an electric field intensity minima. On the other hand, the two profiles at the broadband emissive regime have about half a wavelength of standing waves set up, with an electric field intensity maxima at the CP1/Cr interface. Summarily, resonant $|E|^2$ modes result in reflection, while anti-resonant $|E|^2$ modes result in emission. Here we truly see why our coating is emissive across a wide range of wavelengths: a lot of wavelengths in the mIR regime are able to meet the emissive condition. That is the elegance of designing a cooling surface for a device in the ~350K regime. The corresponding blackbody mIR regime of 2-30 μm means a coating with a dielectric spacer of about 2-2.5 μm will easily fulfil the emissive condition for a broad band of wavelengths beyond $\lambda = 4t$ (about 10 μm).

Figures 2.11. (d)-(f) plot the $|E|^2$ profiles for the double layer Cr backside coating, and drive home our earlier point that the second layer of Salisbury screen exists to increase the number of emissive/absorptive modes where the destructive interference condition is met. Across all these wavelengths, at least one CP1/Cr interface displays the profile of an anti-resonant mode and thus the material is more emissive.

Figure 2.11. (g) plots the $|E|^2$ profile for the ITO Sun-facing coating. We sample some visible spectrum wavelengths to show how interference forms. In a corollary to the earlier point we made where a slight change in thickness of a 2 μm film will change the most intense visible-spectrum wavelength from being reflective to absorptive, we note here that a small change in the wavelength by 200nm causes the $|E|^2$ profile to alternate between resonant and anti-resonant modes.

2.3. Fabrication and Characterization

In order to have some control over the thickness of CP1, we began by spincoating various solutions of CP1 in diglyme, diluted to different ratios. We let these solutions rest overnight to allow the viscous CP1 resin to mix fully with the diglyme solvent. We spincoated these solutions on Si wafers at 1000 rpm and cured them on a hot plate at 110°C for 10 minutes. Thicknesses were evaluated using a profilometer. Figure 2.13. plots the dependence of thickness on the levels of dilution of the CP1 resin.

We fabricate the Cr/ CP1/ Al single Salisbury screen coating using the following method: we evaporate 300nm of Al using electron beam evaporation at a rate of 1 Å/s. We use CP1 diluted with diglyme in a ratio of 7:3 and spin coat this solution on top of the Al back reflector at a rate of 1000 rpm for 1 minute, and proceed to cure it on a hot plate at 110°C for 10 minutes. The thickness of this CP1 layer has been previously verified using profilometry. We then deposit the top 5nm Cr layer via electron beam evaporation at a rate of 0.5 Å/s. Immediately after this step, we evaporate 10nm of SiO_2 on top of it via electron beam evaporation without taking it out of the chamber. This is a passivating layer that prevents Cr from oxidizing upon exposure to air. Cr is known to form a thin layer of spinel oxide that is a few atoms thick [CITE] when exposed to air, and with a film thickness of 5nm, a substantial thickness of the film will have different optical properties that affect the final performance unless it is passivated.

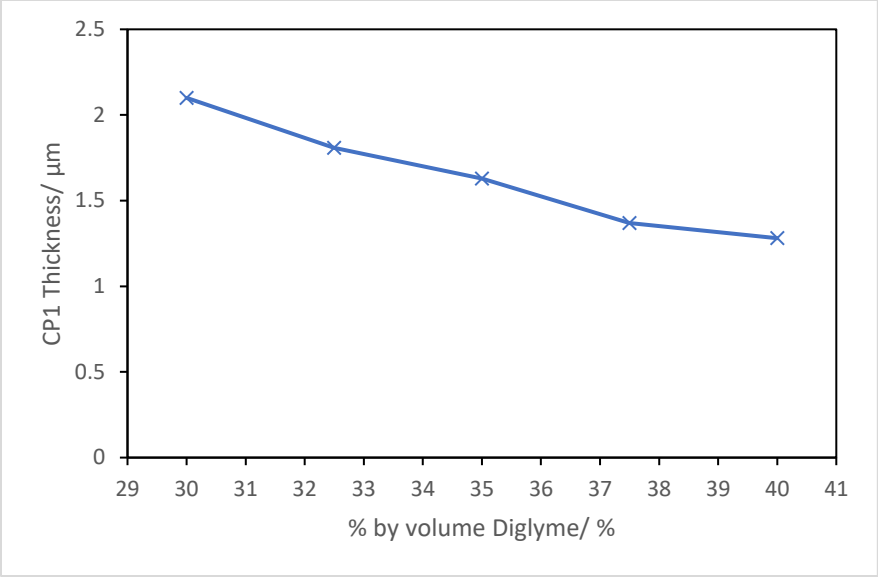

Figure 2.12. Plot of resultant thickness of CP1 film vs level of dilution of CP1 resin.

For the double layer Salisbury screen, we fabricated the Cr/ CP1/ Cr/ CP1/ Al screen using a similar method. We deposited 300nm of Al via electron beam evaporation at 1 Å/s. On top of that, 2.1µm of CP1 was deposited via spincoating of CP1:diglyme ratio 7:3 at 1000rpm for 1 minute, followed by curing at 110°C for 10 minutes. Then 5nm of Cr was deposited at 0.5 Å/s using electron beam evaporation followed by 10nm of SiO_2 at a rate of 1 Å/s. On top of this, 1.5µm of CP1 was deposited via spincoating 6.75:3.25 of CP1 in diglyme at 3000rpm for 1 minute, followed by curing at 110°C for 10 minutes, and Cr and SiO_2 were deposited in a similar manner to what has been described prior.

With the ITO/CP1/Ag screen, Ag was evaporated via electrom beam evaporation at 1 Å/s and CP1 were once again deposited from a CP1:diglyme 7:3 solution in a similar fashion. 10nm of ITO was deposited via sputtering at a rate of 1nm min^{-1}, flowing a mix of Ar and O_2 gas at 0.5 sccm alongside a primary flow of Ar gas at 20 sccm. Once again, in order to avoid oxidation of the top conductor, 60nm of SiO_2 was deposited on top of the ITO layer.

The mIR reflectivity experiments were conducted by performing reflectivity measurements at incident angles from 30° to 80° at 10° intervals using a 2-theta setup on a mIR ellipsometer using the reflection mode. The visible spectrum reflectivity of the Cr Salisbury screen coatings were recorded using a similar setup on a UV-vis ellipsometer in reflection mode at 30°, while that of the ITO Salisbury screen was recorded in an integrating sphere from 15° to 75° at 15° intervals. More attention was given to the visible response of the ITO Salisbury screen coating as we require very strict visible spectrum properties to be met fort his screen, whereas the visible spectrum properties of the Cr are not as important, having no metric that needs to be met.

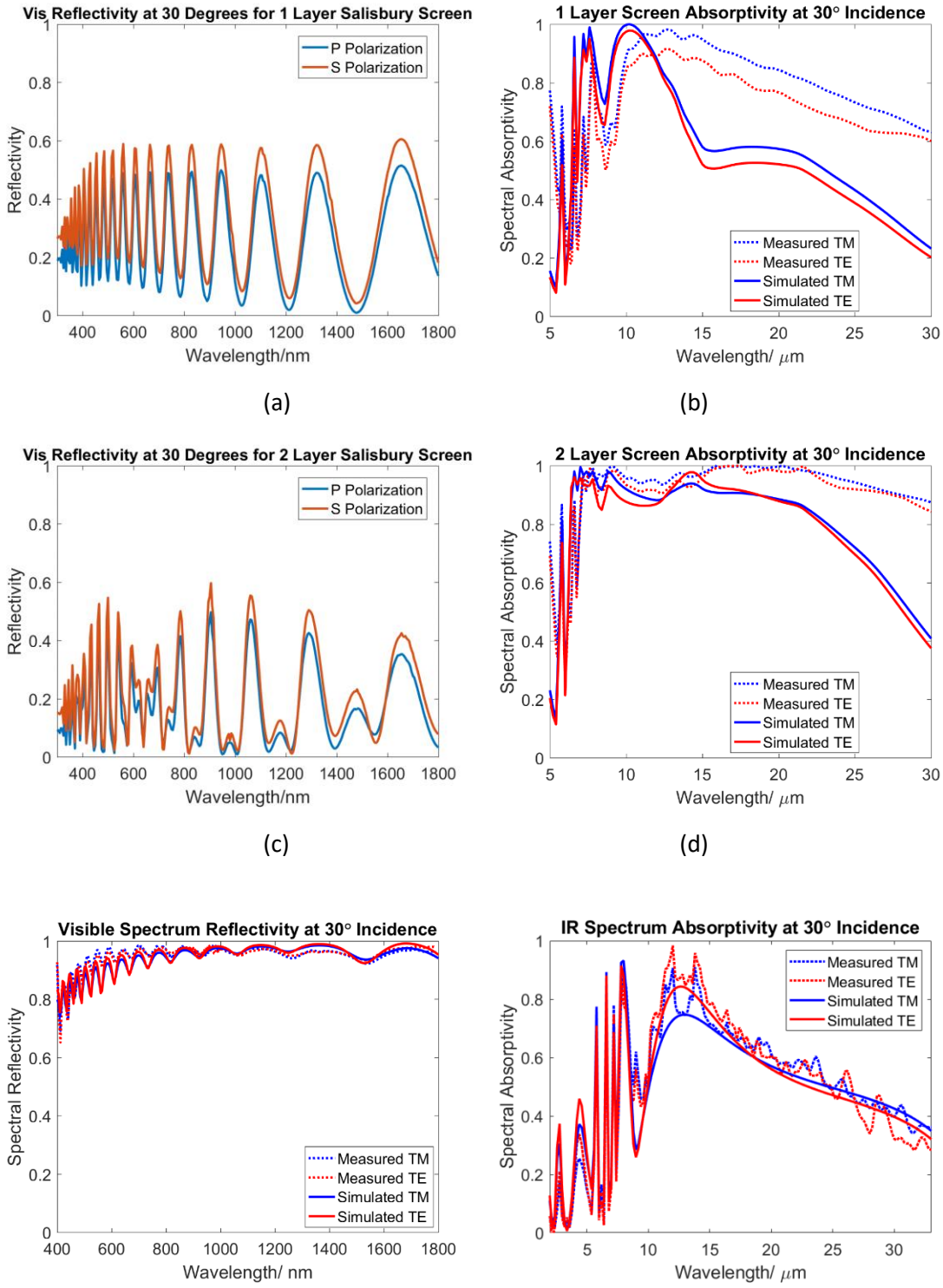

Figure 2.13. Characterizing the coatings and comparing them against their predicted values. (a) Visible spectrum reflectivity and (b) IR spectrum absorptivity of the 1-layer Cr coating; (c) visible spectrum reflectivity and (d) mIR spectrum absorptivity of the 2-layer Cr coating; (e) visible spectrum reflectivity and (f) mIR spectrum absorptivity of the ITO mirror coating.

The visible spectrum reflectivity and mIR spectrum absorptivity of our three films are plotted in Figure 2.13. Where possible, we plot their measured values against their calculated values. We note that the trends observed in the measured mIR spectrum absorptivity generally agree with our RCWA calculations, even though our calculations are at 0° incidence while our measurements were at 30° incidence. We will shortly see that angle insensitivity is a strong feature of our screens. Numerically, we report the spectrum integrated reflectivities and absorptivities in Table X2.1 We declare here that we have successfully met the design specifications as dictated in Section 2.1.3., having fabricated a backside coating with a mIR absorptivity of over 0.85; and a frontside coating with a visible spectrum reflectivity of 0.896 and a mIR absorptivity of 0.554. Furthermore, Figure 2.14. shows photographs of the coatings as fabricated on their wafers, all on the scale of centimeters.

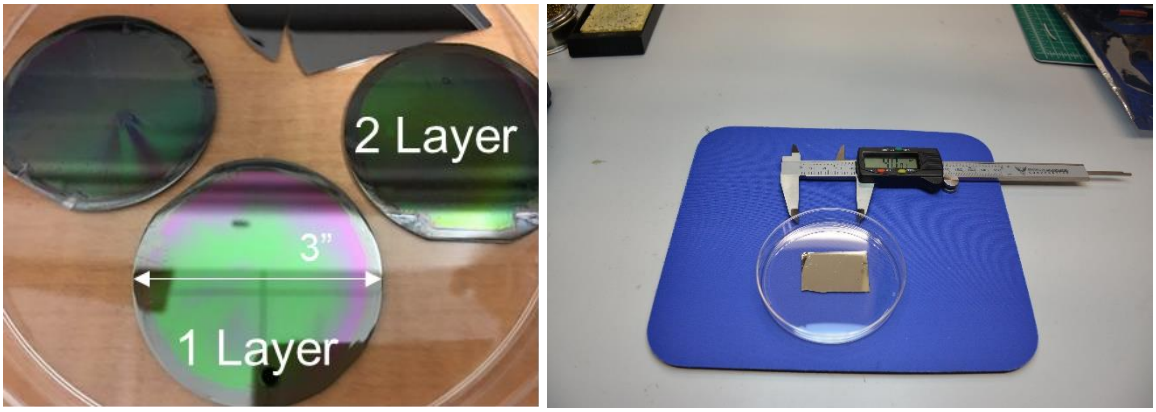

(a) (b)

Figure 2.14. Photographs of (a) the 1-layer and 2-layer Cr coating on 3” wafers and (b) the mirror ITO coating.

Looking to Figure 2.13. (a), (c), and (e), we compare the difference in visible reflectivity between a Cr Salisbury screen coating and an ITO Salisbury screen coating. As mentioned earlier, Cr simply reflects too much light in the visible regime, thus we observe far stronger interference effects across the visible spectrum reflectivity than with the ITO Salisbury Screen coating.

Coating Type	**Calculated Reflectivity**	**Measured Reflectivity**	**Calculated Absorptivity**	**Measured Absorptivity**	**Areal Density/ gm^{-2}**
1 Layer Cr	NA	< 0.5	0.671	0.776	3.3
2 Layer Cr	NA	< 0.5	0.859	0.927	6.0
ITO	0.893	0.896	0.574	0.582	4.1

Table 2.1. Final parameters of the thermally emissive coatings.

Figure 2.15. reports the spectrum-integrated absorptivities and reflectivites of our screens at different incident angles. We note in both screens that mIR absorptivity does not change much until incident angles of 60°. Similarly, the ITO Salisbury screen coating is highly reflective across almost all incident angles.

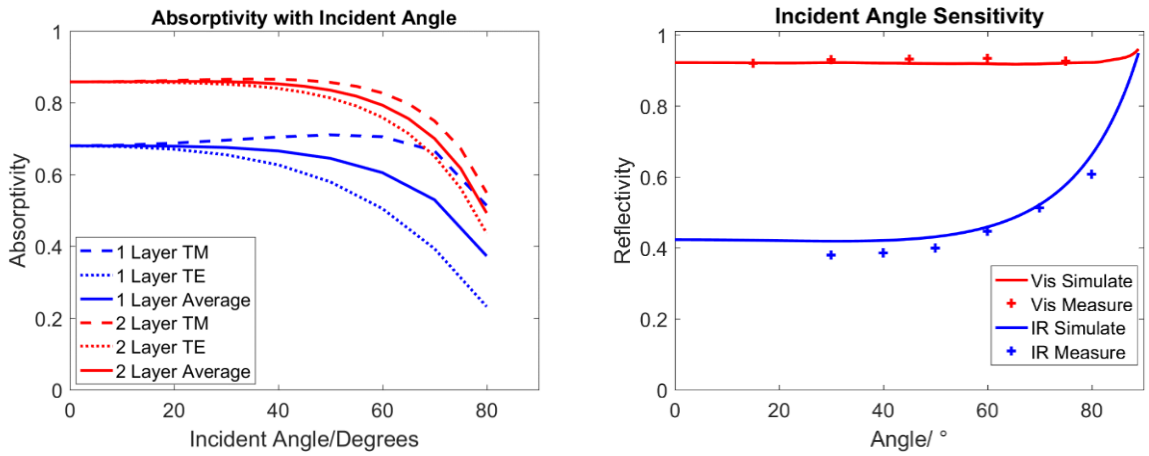

(a) (b)

Figure 2.15. Sampling optical properties at different angles of incidence. (a) Angle sensitive absorptivity of the Cr coatings and (b) Angle sensitive reflectivity (visible and mIR) of the ITO coating.

2.4. Conclusion

In summary, we considered the conundrum of heat loss of solar cells in space and developed broadband IR emissive surfaces to maintain our solar cells at a working temperature of below 80°C. Leveraging thermal simulations done in a previous work, we set out to design frontside and backside coatings for our solar concentrators. We used the Salisbury screen, known to be lightweight and broadband absorptive, as our core platform for designing these structures. Using the RCWA method, we optimised 1-layer Cr/CP1/Al and 2-layer Cr/CP1/Cr/CP1/Al backside coatings, paying special attention to material choices and maximising mIR spectrum absorptivity. With this same eye for material detail, we found the material ITO was suitable for use as a top conductor layer in the frontside mirror coating, and similarly optimized ITO/CP1/Ag structures, this time paying attention to both visible spectrum reflectivity and mIR spectrum absorptivity. Delving deeper into the $|E|^2$ profile in each layer of these coatings yielded key insights as to why such a broadband emissive behaviour was predicted. Finally, these structures were fabricated and measured, and found to agree with the theoretical calculations. A backside emitter coating that was 0.927 emissive in the mIR with areal density 6.0 gm^{-2} was successfully fabricated, as was a frontside mirror emitter coating with visible reflectivity of 0.896 and a mIR emissivity of 0.582 with areal density 4.1 gm^{-2}, successfully meeting the requirements for thermal management of concentrated photovoltaics as set out under our project.

Chapter 3: Perovskite Fabrication Methods and Properties

3.1. A Perovskite-Based Flat Panel Module for SSPP

So far, we have designed technologies for a parabolic concentrator module. We adopted a parabolic concentrator module because launch costs are expensive, yet current common photovoltaic cells must be encapsulated in thick, heavy layers of radiation shielding to block radiation damage from protons and electrons. Concentrated photovoltaics is one way to reduce the heavy mass per unit area taken up by radiation shielding by reducing the amount of cell per unit area that needs to be used. That has been our approach thus far to reduce mass per unit area in our endeavour to lower launch costs. However, there is another philosophy that could be taken to reduce the amount of radiation shielding. If we can find radiation hard photovoltaic cells that need little to no radiation shielding and that can be fabricated on ultralight substrates, we can cut down on over 60% of our mass per unit area easily, and achieve our desired goal of > 10W/g.

We turn to the family of hybrid organic-inorganic organo-lead halide perovskites (OLHP) as a potential candidate. This family of perovskites have seen a lot of study in recent years as a candidate for photovoltaics owing to their favourable properties. In this section we shall expound on not only these exciting properties, but also cover their radiation hardness and ability to self-recover, two properties that make lead halide perovskites an excellent candidate for SSPP.

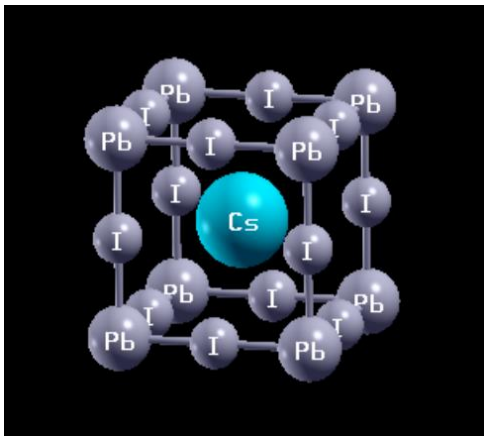

Figure 3.1. Unit cell of a common Perovskite Crystal.

Perovskites refer to a large family of crystal structures of varying chemical compositions and structures. In general, any material with the stoichiometry of ABX_3, where A is a cation of charge n+, B is a cation of charge 2n+ and X is an anion of charge n- qualifies for a perovskite. For instance, the common perovskite CaTiO3 features Ca^{2+}, Ti^{4+} and O^{2-} ions. They adopt a general structure shown in Figure 3.1. In the case of organo-lead halide perovskites, we work with an APbI3 chemistry, where lead is in the Pb^{2+} state, the iodide anion has a charge I^- and A is a small cation of charge 1+. There are three common species used for the A^+ ion: organic molecule methylammonium (MA), $CH_3NH_3^+$; organic molecule formamidinium (FA), $CH(NH_2)_2^+$, and cesium ion Cs^+. In dedicated OHLP studies, very often researchers will use a mix of these three cations to achieve various properties such as improved stability, better bandgaps, and so on, resulting in many reports formulating fairly complicated $(MA_{1-x-y}FA_xCs_y)PbI_3$ stoichiometries [41]. This class of materials offers properties that make themselves very favourable to photovoltaics as well as SSPP.

This stoichiometry and crystal structure lends perovskites some interesting properties. The first of these is a good and tuneable bandgap. $MAPbI_3$ has a bandgap of about 1.6 eV [42], $FAPbI_3$ has one of around 1.48 eV [43] and $CsPbI_3$ has a bandgap of around 1.73 eV [44]. That makes this family of perovskites very close to the ideal bandgap of a single junction cell- 1.4eV under Shockley-Quessier theory [45]. Furthermore, these materials have been predicted to have a direct bandgap during absorption but also an indirect bandgap nearby which prevents easy recombination [46], making OLHPs very ideal absorbers for photovoltaics on a base level. Not only that, but their bandgap is also fairly tuneable. A number of studies have investigated mixing up the A stoichiometry, but more success has been met mixing the I^- species with Br^- to successfully achieve bandgap tuning [47]. These combine for a material that can absorb light close to the theoretical limit.

A favourable bandgap is an excellent starting point for any potential photovoltaic absorber material, but just as important are its charge transport properties, which dictate how fast this photogenerated, mobile electrons and holes can be separated into useful energy. Perovskites feature high carrier mobility of up to 10 $m^2V^{-1}s^{-1}$ [48] as well as long diffusion lengths on the order of microns [49], giving them very good charge transport properties. On top of this, one of the strongest advantages to their charge transport properties lies in the fact that they feature soft and mobile lattices. What this means is that thermodynamically, only shallow traps have been found to occur easily in the bulk [50]. These favourable charge transport properties, together with the excellent absorptive properties, make OLHPs a family of materials who have rivalled silicon in terms of single-junction efficiency, boasting records of 25.7% as verified by NREL [51].

On top of this, OHLPs are fairly easy to fabricate. All the species are easily soluble in common solvents such as dimethylformamide (DMF) and dimethyl sulfoxide (DMSO) into a precursor solution, and form their structure at an anneal temperature of around 370K [52]. In terms of the semiconductor industry, this is a fairly low temperature, as Si and GaAs technologies can require fairy high processing temperatures [53] [54]. It also means they are easily incorporated into roll-to-roll fabrication via similarly low-cost processing techniques such as spincoating, slot-die deposition, gravure printing and chemical vapor deposition, all of which have been demonstrated to produce working perovskite solar cells [55]. This makes them easy and cheap to fabricate, and more importantly, more easily fabricated on a flexible substrate.

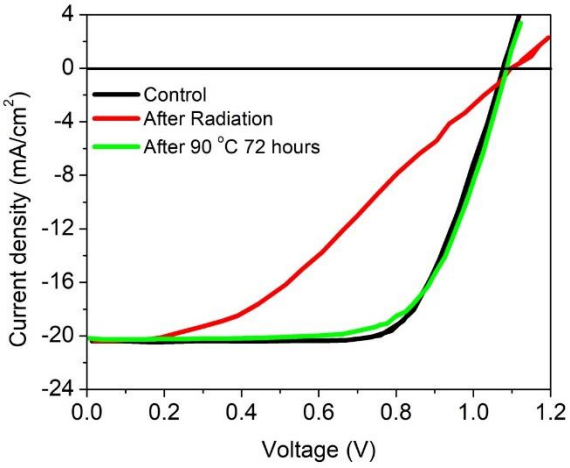

Figure 3.2. JV curve demonstrating anneal recovery of OHLP cells damaged by protons [56]. © 2011 IEEE.

Finally, in favour of this case we make for OHLPs as a material for SSPP, they have been demonstrated to be resistant to electron radiation and proton radiation, two common sources of radiation damage found in outer space. There is plenty of existing literature on how OHLP solar cells are little affected when exposed to a ten-year fluence of 1 MeV electrons [24], and a decent amount of data demonstrating OHLPs to be resistance to protons in the keV to MeV energy range [56]. In particular, OHLP cells subject to degrading fluences of proton irradiation were still demonstrated to be able to recover the performance lost this way, as seen in Figure 3.2. [56]. This means that OHLP cells are either hard against radiation, or are able to recover the damage sustained from radiation, making them an exciting candidate for SSPP applications.

In this chapter, we report some of the work we have done in regards to the fabrication, evaluation and calculation of perovskites. In doing so we wish to shed light on the practices, considerations, and experiences of working on OHLPs. They are a nuanced, yet accessible class of material that are sensitive to fabrication processes, testing methods and storage conditions. Many insights are quickly gleaned from a simple optimisation study of the fabrication process of these devices, and many a nugget of wisdom must be accrued before one can begin producing high-quality, stable perovskites.

3.2 The Perovskite Cell

OHLP cells are heterolayer p-i-n devices comprising several materials stacked on top of a superstrate, through which light usually passes. Figure 3.3. shows the three common architectures these structures usually take. The first, most common stack features a transparent conducting oxide (TCO) on top of the superstrate, upon which a film of electron transport layer is deposited (ETL), followed by the perovskite, then a hole transport layer (HTL) and finally top contacts. The second uses this same stacking order, but now the ETL is mesoporous to allow for improved surface area. We call this a mesoporous n-i-p stack. The third structure is a thin film stack very much like the first, but the HTL is at the bottom and the ETL is at the top. The community commonly refers to this p-i-n stack as the inverted structure, to be distinguished from the standard, more common n-i-p stack [57].

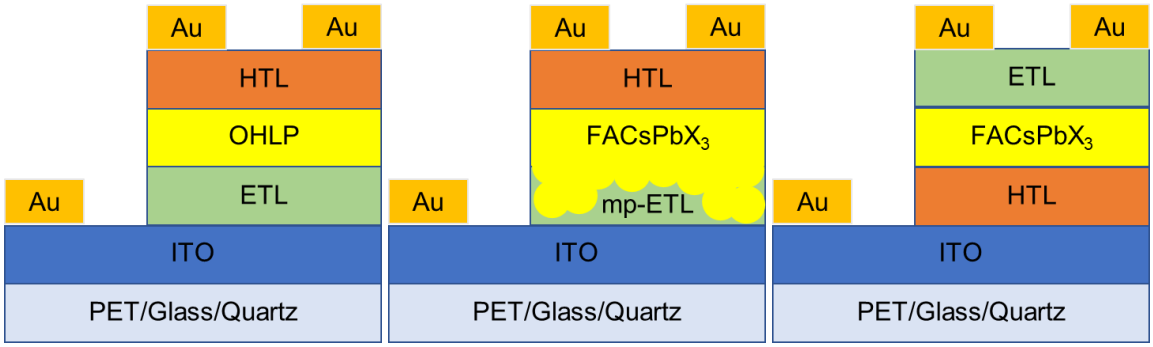

Figure 3.3. Different configurations of OHLP cells. (a) The common n-i-p thin film device, (b) the mesoporous n-i-p device architecture and (c) the inverted p-i-n architecture.

At first glance, it is easy to dismiss these different types of architectures as perhaps somewhat trivial, as they all still follow a common Electrode/ETL/OLHP/HTL/Electrode composition. However, this dichotomy arises because of restrictions surrounding the OHLP layer's deposition. OHLPs are easily soluble in polar solvents [58] and degrade under temperatures beyond 400K [59]. As such, the transport layer deposited

above the OHLP film must not use a solvent that would dissolve the OHLP, nor must it involve a high temperature anneals or be evaporated in a way that excessively thermalizes the stack. In general, this usually means the top transport layer is dictated by the choice of the bottom transport layer, and is usually restricted to organic semiconductors deposited via organic solvents with low temperature cure/anneal steps, or semiconductors that can be gently thermally evaporated onto the substrate.

The top transport layer usually has more freedom of material selection. If the bottom layer is an ETL, it is usually TiO_2, commonly deposited by high temperature spray pyrolysis [60] or SnO_2, commonly deposited via water-based reactions [61]. If the bottom layer is a HTL, it is usually NiO_x, deposited commonly via water-based solgel process above 600K [62] or PEDOT, also deposited from polar solvents with a high cure temperature [63].

In this section, we cover work done on devices using two formulations of OHLPs. We will report various fabrication techniques used, the motivation behind attempting these techniques and through basic IV sweeps, show the direct effect of these different techniques on our devices. As an overview statement, it is important to stress that we work with no less than 5 different active materials in a single OHLP solar cell, and we will soon see that even the slightest change to the processes of one of these materials often dictates some changes to that of the other materials. For this study, we shall try and limit the variations to the ETL and HTLs used, focusing instead on optimizing the general process as well as the perovskite recipe. We shall use the inverted p-i-n structure, opting for NiO_x as our bottom HTL and C_{60}-PCBM as our top ETL. This structure is one our group is familiar with, and one that has been demonstrated to yield good results [64].

3.3. Fabricating $MAPbI_3$ Devices

We begin our fabrication study with the most straightforward and prolific OHLP so far, $MAPbI_3$. NiO_x and PCBM are known to favourably align with the bandgap of $MAPbI_3$, as can be seen in the band diagram in Figure 3.4. [64]. Both materials also have solution-processed recipes, with fairly simple fabrication steps, as we shall shortly see. This makes for an easy device to begin our fabrication study on. Contextually, this study represents our first foray into the fabrication and characterisation of these devices. As we will see, there are some shortcomings and glaring missing studies intrinsic to this work that would otherwise elevate it greatly. As a more experienced researcher, it important when reviewing this data to address these shortcomings, and we will tackle these mistakes as part of this discussion.

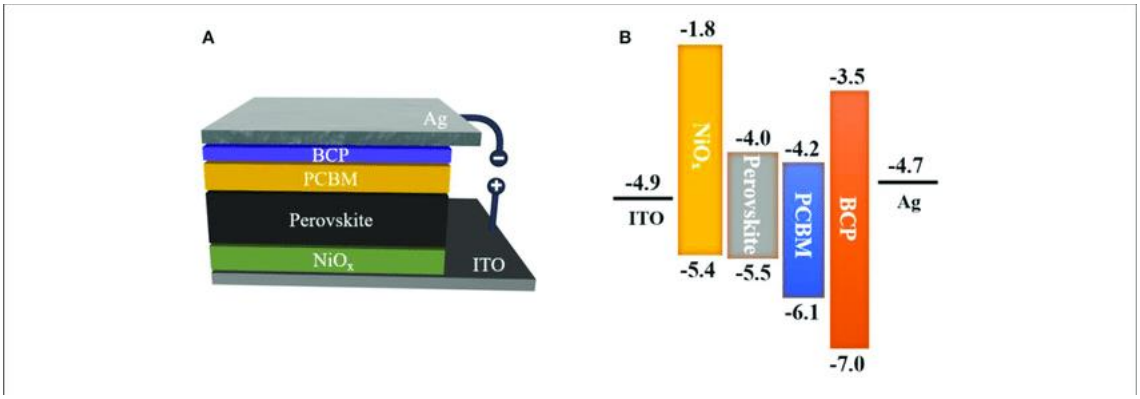

Figure 3.4. Band alignment diagram of NiO_x/$MAPbI_3$/PCBM [64]. © 2018 He, Zhang, Zhao, Lin and Ye.

Our recipe is as follows: one day prior, three precursor solutions were mixed. For the NiO_x precursor, in a cleanroom fume hood, 248 mg of nickel (II) acetate tetrahydrate ($(CH_3COO)_2Ni \cdot 4H_2O$) was mixed with 0.06 ml of ethanolamine ($NH_2CH_2CH_2OH$) and dissolved in 10 ml of ethanol and sat overnight, resulting in an ocean green solution. For the $MAPbI_3$ solution, in a nitrogen-filled glovebox, 461 mg of lead (II) iodide (PbI_2) was mixed with 159 mg of methylammonium iodide (MAI) and dissolved in a solution of 0.2 ml DMSO and 0.8 ml of DMF. The solution was stirred overnight to achieve a clear yellow solution. For the PCBM, also in a glovebox, two recipes were attempted, as will be covered shortly. In the first recipe, 400 mg of PCBM was dissolved in 20 ml of chlorobenzene (CB) and stirred overnight. In the second, 16 mg of the surfactant cetrimonium bromide (CTAB- $CH_3(CH_2)_{18}NH_3Br$) was added to 400 mg of PCBM and 20 ml of CB in an attempt to improve electrical properties and wettability of the PCBM film [65]. The solution was also stirred overnight.

On the day of fabrication, we begin by ultrasonicating 2.5cm x 2.5 cm ITO-on-glass substrates in three consecutive solutions: first, a solution of 0.5 g of alconox in 300 ml of DI water for 10 minutes; second, acetone for 10 minutes and third, isopropyl alcohol for 10 minutes. After each step, the substrates were rinsed in the next step's medium, and on the final step, the substrates were gently blown dry with N_2 gas. The slides were then cleaned in a UV-ozone cleaner for 10 minutes. All these steps ensure our substrates are clean and contaminant-free.

The NiO_x film was first deposited on these slides. In the same fume hood in the cleanroom, 50 µl of the NiOx precursor solution was spincoated on the slides at 3000 rpm for 60 s. These slides were then annealed at 300°C for 60 min on a hotplate in a fume hood. They were then transferred into the nitrogen-filled glovebox where the $MAPbI_3$ and PCBM precursors were stored. There, 50 µl of $MAPbI_3$ precursor solution was spincoated in a two-sep process: first at 1000 rpm for 10 s to allow the precursor to spread evenly across the surface, then at 4000 rpm for 30s. 10 s into the 4000 rpm step, 250 µl of CB antisolvent was pipetted quickly and steadily (within 1 s) onto the slide. This is a common step used to help remove the DMF and DMSO solvent to aid in heterogeneous nucleation via supersarutation. This is known to result in better OHLP grain size and quality [66]. At this point, the slides were a translucent yellow due to the $MAPbI_3$ precursor. The slides were then annealed at 50°C on a hotplate for 3 min until they turned dark brown, then they were transferred onto a 100°C and annealed at a further 20 min. At the end of this process, the perovskite films were black with a smooth, shiny finish, indicative of the film's excellent light absorptive properties.

From there, three recipes were attempted to make 4 slides worth of perovskite devices. In the recipe 1, the first solution of PCBM in CB was drawn and passed through a 0.45 µm PTFE syringe filter. Via this method, about 0.1 ml of this precursor was spincoated onto the device at 1000 rpm for 60 s. The device was then allowed to dry in the glovebox. The samples were then removed from the glovebox, a portion of the film was scratched off to expose the bottom ITO contact, resulting in a top-down perspective as seen in Figure X. 100nm of silver contacts were then thermally evaporated onto the device at 2 Å s^{-1}. In recipe 2, the CTAB + PCBM in CB solution was filtered and spincoated under similar conditions as described in recipe 1, and 100nm silver contacts were thermally evaporated at a rate of 1 Å s^{-1}. In recipe 3, instead of silver, copper was used as the literature suggests silver degrades the perovskite layer by interacting with the iodide content [67]. Furthermore, recipe 3 was repeated in recipe 4, but with newly bought chemicals as opposed to the existing stock of chemicals used in recipe 3. The resultant devices are summarized in Figures 3.5. (a), (b) and (c), with the general schematic of these devices illustrated in Figure 3.5. (d). Note that because lateral transport is very poor across the HTL, ETL and OHLP layers, in general,

with these devices, the active area of each cell is the overlap of the top metal electrode with the bottom ITO film, where charge can be laterally separated and transported to each electrode.

The cells were measured under an ABET solar simulator calibrated against an Si solar cell to AM1.5. Cells were measured in a forward sweep from -0.2V to 1V using a Keithley voltammeter. This is a shortcoming and bad form, and we would address this bad practice subsequent experiments where we conducted both a forward and reverse sweeps. As we will see in the next section, omitting the reverse sweep leaves out a very crucial feature intrinsic to perovskites. Figure 3.5. (e) plots the IV sweeps of the four devices we made for each recipe, and in Table X we summarize the power conversion efficiency (PCE), fill factor (FF), open circuit voltage (V_{oc}) and short circuit current density (J_{sc}) obtained from this IV data for each cell.

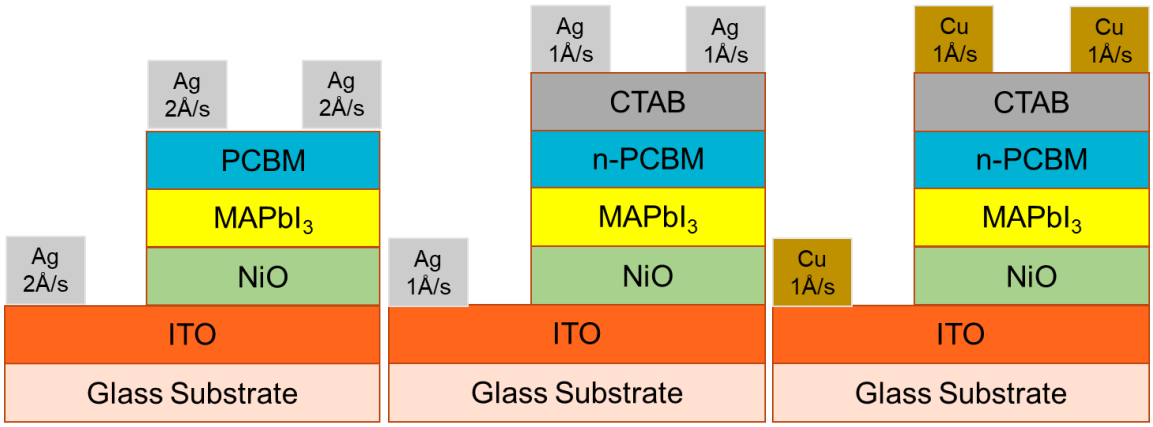

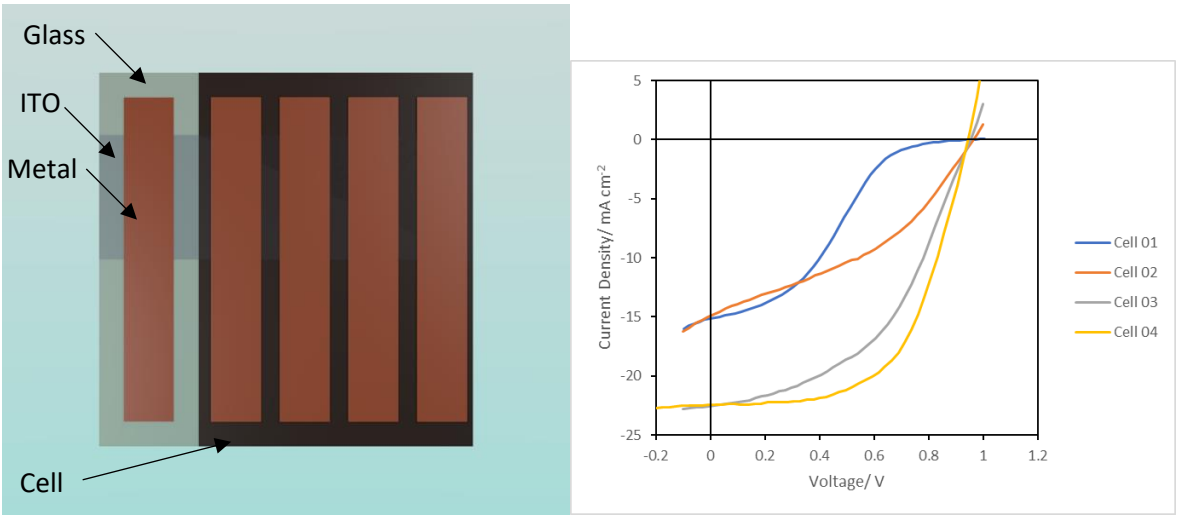

Figure 3.5. The cross sectional schematics of devices made under (a) recipe 1, (b) recipe 2, (c) recipes 3 and 4, as well as (d) how those cells appear from a top-down perspective. Their IV characteristics are summarized in (e).

Referring to Table 3.1. and Figure 3.5. (e), cells 1, 2, 3, and 4 are champion cells from the slides made under recipes 1, 2, 3, and 4, respectively. It is clear to see that our overall performance improves as we

make adjustments to our recipe. As such, we will begin comparing the changes made from one recipe to the next and consider, to first order, their immediate effect on the IV curve and cell performance.

Cell	PCE/ %	FF/ %	V_{oc}/ mV	J_{sc}/ mA cm^{-2}	Architecture	Notes
1	4.04	28.1	951.9	15.12	ITO/NiO/$MAPbI_3$/PCBM/Ag	Ag deposition 2Å/s
2	5.56	34.0	954.7	13.99	ITO/NiO/$MAPbI_3$/PCBM+CTAB/Ag	Ag deposition 1Å/s
3	10.17	47.2	954.3	22.56	ITO/NiO/$MAPbI_3$/PCBM+CTAB/Cu	Cu deposition 1Å/s
4	12.41	58.7	944.4	22.43	ITO/NiO/$MAPbI_3$/PCBM+CTAB/Cu	New chemicals

Table 3.1. Summary of $MAPbI_3$ cells fabricated and the iterative changes used to improve each step.

The key differences between recipes 1 and 2 were that a surfactant CTAB was added to help wetting of the PCBM layer on the OHLP film, and the silver deposition rate was reduced from 2 Å s^{-1} to 1 Å s^{-1}. From Figure X, we note cell 1 displaying an S shaped kink that gets eliminated in cell 2, resulting in a fill factor-driven improvement in PCE of 1.5%. While this improvement is small and this data is fairly simple, it tells us quite a fair bit. S-shaped kinks in the IV curve are known to occur in organic solar cells and are generally attributed to mobility mismatch [68] [69]. One way to express what is happening in cell 1 is this: as the external forward bias is applied to the illuminated cell, an extra diodic response is observed before the V_{oc} point. One could easily be influenced to postulate that a second depletion region, somewhere else in the cell, is being overcome. In fact, it has been shown that if the HTL is several orders of magnitude better at conducting holes than the ETL is at conducting electrons, then simple drift-diffusion models predict this S-kink [70]. If one carrier is being extracted at a higher rate than another, it stands to reason that a secondary depletion region could easily form across the device during illuminated operation. It is clear that adding CTAB to our PCBM solution improves the electronic properties of PCBM. In fact, CTAB is known to n-dope PCBM [65], clearly offering a boost to PCBM's electron mobility.

The difference in recipes 2 and 3 was that Cu was used in place of Ag at the top contact. The performance increase was must more drastic and photocurrent current-driven. We see Jsc increase from 13.99 mA cm^{-2} to 22.56 mA cm^{-2} resulting in an increase in PCE of about 4.6% to 10.17%. Of note is that this current density is close to literature records [64] [65]. At zero bias, we are generating more photocurrent using Cu contacts as opposed to using Ag contacts. Although both Ag and Cu contacts are known to have detrimental effects on the OHLP layer [67], it is possible that Cu impinges the film more gently than Ag and thus does not immediately damage the film as Ag would. As the PCBM layer is an organic layer often within thicknesses of 20-50 nm [71], it is very easy for energetic, evaporated Ag species to interact with the iodide content of the MAPbI3 layer to form AgI precipitate, reducing the ability of the absorber layer to generate photocurrent. As we can see, no such issue occurs with Cu contacts, resulting in much better photocurrent generation from a higher quality OHLP film.

From recipe 3 to recipe 4, a refresh of inventory was performed. The old chemicals used in recipe 3 were purchased over one year prior to fabrication, while the new chemicals used in recipe 4 were purchased. This resulted in an increase in PCE of 2%, pushing our champion PCE over what was a very important milestone for our own progress at the time, as it is now within range of that 15% we used in our assessment of flat panel SSPP. This increase is mostly due to in increase in FF, something that has been mostly increasing in the background as our cell quality increased across the previous recipes, but is now

the primary driver. It can be tricky to attribute any one aspect of the cell to a fill factor improvement based exclusively off light-IV data, as almost everything affects FF from series and shunt resistances to recombination processes. However, somewhat generally, it can be said that using fresh materials results in a better overall solar cell simply because the newer materials are less degraded than the older materials, and should result in better absorber layers, ETLs and HTLs.

There is some pause for reflection here. As mentioned at the start of this section, chronologically, this was one of our first forays into work on OHLP solar cells. As such one might note that this study was almost solely focused on the forward-swept light-IV characteristics. Although quite a bit of insight could be gleaned from a basic light-IV trend analysis, towards the end it is clear that the sole focus on light-IV becomes somewhat limiting. External quantum efficiency measurements could help elucidate the differences between cells 2 and 3, while dark IV, ptoholuminescence (PL) and time-resolved photoluminescence (TRPL) measurements in particular could help elucidate additional insights regarding the differences between cells 3 and 4 as these measurements could shed light on important parameters such as recombination mechanisms. Scanning electron microscopy could yield important insights into the microstructure of the OHLP films, which ideally aim to be 300-500 nm thick with grain sizes of 300-500 nm in diameter [CITE]. While such methods will be touched on in future sections, they were outside the scope of this initial study, which was to get accustomed to and improve basic PCE performance.

Of note is that through this study, many of these methods were attempted, especially PL and TRPL, however owing to poor film quality, useful data relevant to these discussions were unable to be gleaned from these studies. Nonetheless, we will report them in Appendix A.

Overall, through this simple, preliminary study where basic elements such as ETL additives and contact materials were varied, we can see that fabricating a successful OHLP cell requires very intimate understanding of every process in the recipe. Varying the materials and techniques of even two layers, and doing something as simple as refreshing one's chemical inventory to use only the highest quality materials, makes a huge bearing on the final cell efficiency. We take this knowledge into our next study, where we tackle the perovskite absorber layer itself.

3.4. Fabricating $(FA1\text{-}_xCs_x)PbI_3$ Mixed Cation Devices

In this next section, we attempt fabricating MA-less OHLP devices. We seek MA-less formulations because amongst MA, FA and Cs species, MA-based OHLPs have been studied to be the most volatile OHLPs and most ready to degrade as MA is smaller, lighter and more reactive than FA and Cs [72]. A mix of FA and Cs must be attempted because either alone is unable to achieve performances found in MA-based OHLPs. FAPbI3 simply does not have a stable black photoactive phase, while Cs cannot easily form the desired bandgap [73]. When mixed together however, some successful, high-efficiency results have been reported [74].

Whenever one attempts to mix two different crystals together to form a solid solution, there is always the question of what band of ratios are permissible for the solid solution to exist, and what ratios cause either crystal to precipitate out, unable to thermodynamically exist in the same phase. Regarding perovskites in general, thankfully, this range is well-known. In fact, there is a theoretically predicted range for this solid solution that will form the black phase, expressed as the tolerance factor of the solid solution [75]. This range is expressed in Figure 3.6. For an FA-Cs system of OHLPs, the best ratios generally do not exceed FA:cs ratios of 70:30 [75].

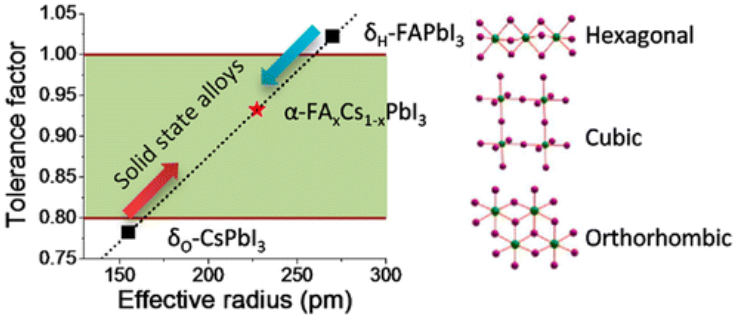

Figure 3.6. Perovskite tolerance factor for a FA-Cs OHLP system. Reprinted with permission from [75]. © 2016, American Chemical Society.

Regarding the specific recipe, even with a known stoichiometry, there are still optimisation questions one could spend entire years of study on and still not reach a satisfactory answer on, such as optimum concentrations, solvent and antisolvent ratios, spincoat timings and speeds and anneal temperatures and times. Thankfully, science is not conducted in a vacuum, and we have some outstanding research done by the OHLP community to refer to. Reviewing the literature, we found three recipes that we found promising and compatible with our own research equipment, and it is these recipes that we will cover in this next study.

The three recipes we used employ different precursor solutions. For all other steps, the recipe for NiO_x as laid out in section 3.2.2. was used, and the CTAB + PCBM recipe in recipe 2 of section 3.2.2. was used. In the first recipe [76], in a nitrogen-filled glovebox, 646.8 mg of PbI_2, 240 mg of FAI, and 18.2 mg of CsI were dissolved in 0.2 ml DMSO and 0.8 ml of DMF and stirred at 60°C for at least 2h, achieving an FA:Cs ratio of 0.95:0.05 in a concentration of 1.4 M. This precursor solution was deposited on the NiO_x-deposited film via two-step spincoating first at 1000 rpm for 15s and then at 4000 rpm for 45s. 15s into the second step, 200 µl of CB was drop-cast onto the film. The film was then annealed at 100°C for 3 min. Films 1, 2 and 3 on Figure 3.7. (a) show the physical appearance of these films. In the second recipe [77], 507.1 mg pf PbI_2, 163.4 mg of FAI and 13.99 mg of CsI were dissolved in 0.2 ml DMSO and 0.8 ml of DMF and stirred overnight, achieving an FA:Cs ratio of 0.95:0.05 and a concentration of 1M. The solution was deposited on the NiO_x-deposited film in a two-step spincoating process at 1000 rpm for 10s and then 4000rpm for 20s, with 200µl of CB drop cast at the start of the second step. The film was then annealed at 100°C for 10 min, and photos of the films can be seen in slides 4, 5, and 6 on Figure 73.7. (a). Finally, now that concentration was varied, stoichiometry was varied in recipe 3 [78]. Here, in a nitrogen-filled glovebox, 576.3 mg of PbI_2, 182.7 mg of FAI and 48.71 mg of CsI were dissolved in 0.2 ml DMSO and 0.8 ml of DMF and stirred overnight, achieving an FA:Cs ratio of 0.85:0.15 in a concentration of 1.25 M. This precursor solution was spincoated on the NiO_x-deposited films also via a one-step spincoat process at 6000 rpm for 30s, with 80µl of CB drop cast at the 10^{th} second. The films were then annealed at 110°C for 15 min, achieving slides 7, 8 and 9 on Figure 3.7. (a).

From there, the CTAB-doped PCBM solutions were deposited on slides 2, 3, 5, 6, 7, and 9, leaving slides 1, 4 and 8 for scanning electron microscopy (SEM) with the intention of gleaning information of their microstructures. Figure 3.7. (b) shows the slides with the full HTL/OHLP/ETL layers on them, before Cu contacts were deposited via thermal evaporation at a rate of 1 $Å s^{-1}$.

As mentioned earlier, slides 1 (recipe 1), 4 (recipe 2), and 8 were used for SEM imagine. They were loaded on a chuck holder as shown in Figure 3.7. (c) and SEM images of these samples were taken and shown in Figures 3.7. (d), (e), and (f), respectively. An ABET solar simulator fitted with an AM1.5 filter was calibrated to AM1.5 with a Si solar cell. The cells were illuminated and light IV data was recorded on a Keithley voltammeter via both forward and backward sweeps from -0.2V to 1.0V and back. The IV data is plotted in Figure 3.8, with the PCE, FF, J_{sc} and V_{oc} data summarized in the tables in Table 3.2.

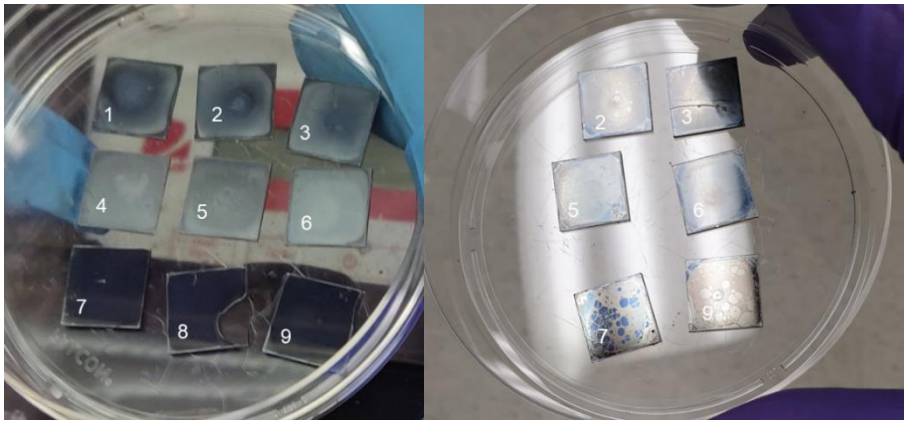

(a) (b)

(c)

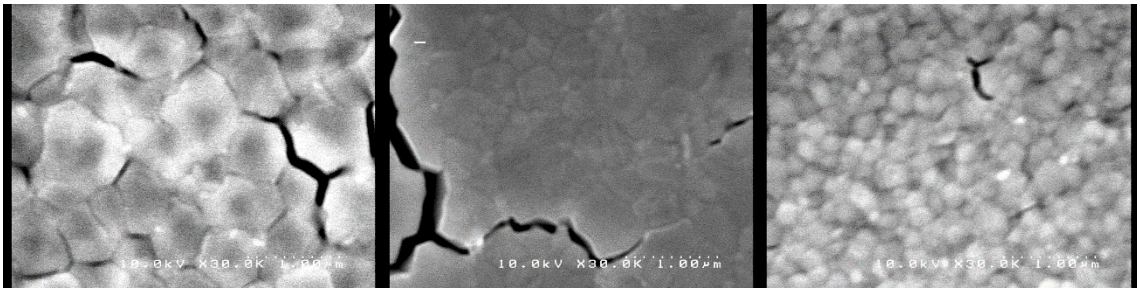

(d) (e) (f)

Figure 3.7. Documentation of the FA-Cs fabrication process (a) spincoated FACs films, (b) with CTAB doped PCBM deposited (c) slides 1, 4 and 8 mounted on an SEM chuck and SEM photos of (d) slide 1, (e) slide 4, and (f) slide 8.

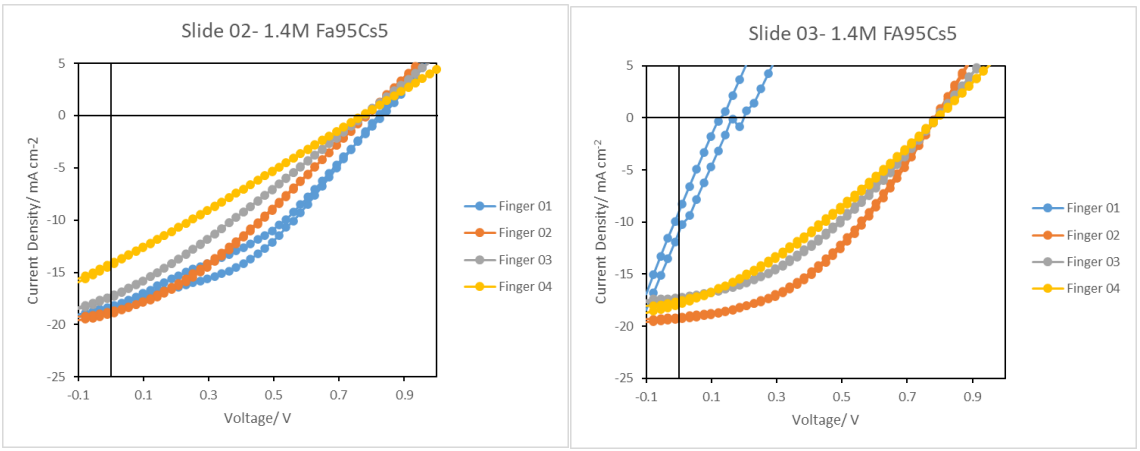

(a)

(b)

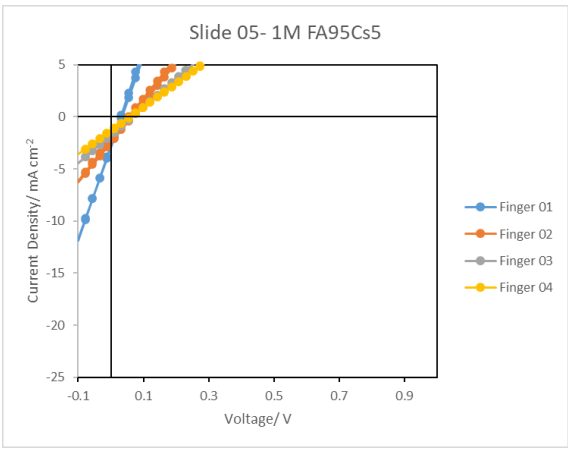

(c)

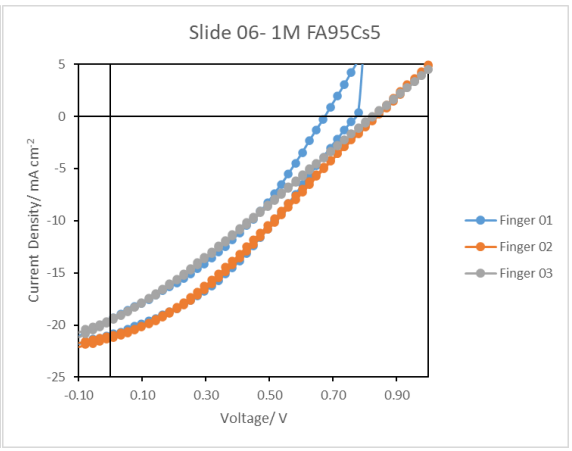

(d)

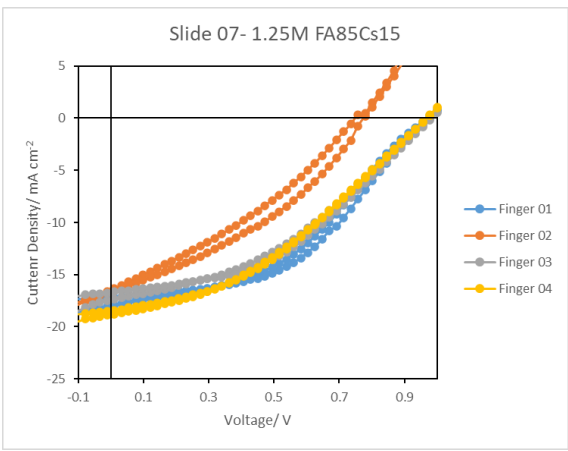

(e)

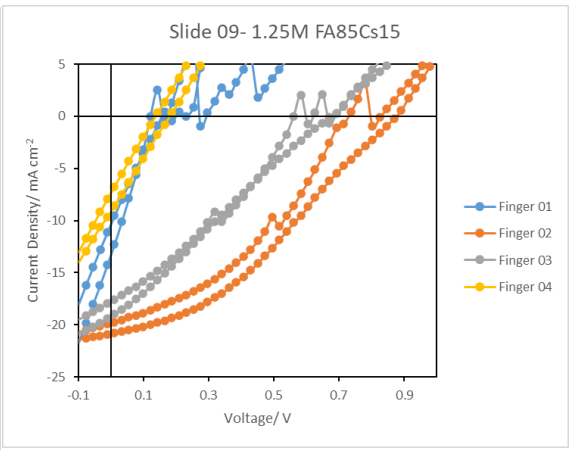

(f)

Figure 3.8. Light IV curves for cells made from precursor solutions of (a), (b) 1.4M $FA_{0.95}Cr_{0.05}PbI_3$, (c), (d) 1M $FA_{0.95}Cs_{0.05}PbI_3$, (e), (f), 1.25M $FA_{0.85}Cs_{0.15}PbI_3$.

Slide 02	1.4M FA95Cs5			
Finger	PCE/%	FF/%	Voc/mV	Jsc/mA cm^-2
F1F	5.44	35.6	833.6	18.22
F1R	5.99	4.1	819.7	18.25
F2F	4.65	31.3	784.8	18.94
F2R	4.73	32.3	782.0	18.74
F3F	3.75	27.8	776.8	17.38
F3R	3.75	28.0	774.2	17.26
F4F	2.85	25.9	770.1	14.30
F4R	2.86	26.1	771.5	14.16
Average	4.25	26.4	789.1	17.16
Std Dev	1.15	9.6	24.0	1.90

(a)

Slide 06				
Finger	PCE/%	FF/%	Voc/mV	Jsc/mA cm^-2
F1F	5.63	35.0	770.4	20.91
F1R	4.55	34.6	675.2	19.49
F2F	5.36	30.0	839.0	21.27
F2R	5.54	31.7	829.4	21.03
F3F	4.36	26.9	826.9	19.63
F3R	4.44	27.7	823.6	19.48
F4F	2.65	26.4	733.6	13.69
F4R	2.17	27.5	729.4	13.52
Average	4.34	30.0	778.4	18.63
Std Dev	1.30	3.4	60.7	3.18

(b)

Slide 05	1M Fa95Cs5			
Finger	PCE/%	FF/%	Finger	PCE/%
F1F	Shunted			
F1R				
F2F				
F2R				
F3F				
F3R				
F4F				
F4R				
Average	N/A			
Std Dev				

(c)

FF/%

Slide 06				
Finger	PCE/%	FF/%	Voc/mV	Jsc/mA cm^-2
F1F	5.63	35.0	770.4	20.91
F1R	4.55	34.6	675.2	19.49
F2F	5.36	30.0	839.0	21.27
F2R	5.54	31.7	829.4	21.03
F3F	4.36	26.9	826.9	19.63
F3R	4.44	27.7	823.6	19.48
F4F	2.65	26.4	733.6	13.69
F4R	2.17	27.5	729.4	13.52
Average	4.34	30.0	778.4	18.63
Std Dev	1.30	3.4	60.7	3.18

(d)

Slide 07	1.25M FA85Cs15			
Finger	PCE/%	FF/%	Voc/mV	Jsc/mA cm^-2
F1F	7.32	42.0	967.7	18.00
F1R	7.80	46.6	974.0	17.18
F2F	4.00	32.4	750.4	16.46
F2R	4.68	36.3	775.1	16.61
F3F	6.48	37.9	980.6	17.42
F3R	6.92	42.1	983.5	16.70
F4F	6.63	36.4	966.6	18.85
F4R	6.73	37.7	968.6	18.46
Average	6.32	38.9	920.8	17.46
Std Dev	1.30	4.4	98.0	0.89

(e)

Slide 09				
Finger	PCE/%	FF/%	Voc/mV	Jsc/mA cm^-2
F1F	Shunted			
F1R				
F2F	6.33	34.7	874.2	20.85
F2R	5.47	37.9	727.8	19.83
F3F	3.22	24.9	673.6	19.18
F3R	3.43	34.9	560.0	17.74
F4F	Shunted			
F4R				
Average	4.61	33.10	708.90	19.40
Std Dev	1.53	5.66	130.51	1.30

(f)

Table 3.2. Light IV data for cells made from precursor solutions of (a), (b) 1.4M $FA_{0.95}Cr_{0.05}PbI_3$, (c), (d) 1M $FA_{0.95}Cs_{0.05}PbI_3$, (e), (f), 1.25M $FA_{0.85}Cs_{0.15}PbI_3$.

From the light IV data, it is immediately apparent that the best cells come from the $(FA_{0.85}Cs_{0.15})PbI_3$ (FA85-Cs15) recipe. Intuitively, based on the visual inspection of the films as seen in Figure X (a), this makes sense as only the $(FA_{0.85}Cs_{0.15})PbI_3$ (FA95-Cs5) recipe resulted in OHLP films that were dark and reflective, as opposed to the matte finish observed in the $(FA_{0.95}Cs_{0.05})PbI_3$ recipes, which usually indicates the film is of higher crystalline quality. We note higher V_{oc} in the FA85-Cs15 as well as slightly better FF compared to the FA95-Cs5 cells which once again points to overall better crystalline quality as a more crystalline film yield better semiconductor response.

From the SEM images, we note the grains appear smaller in the FA85-Cs15 recipe than the FA95-Cs5. The grain sizes in the FA95-Cs5 films appear around 500nm to 1µm, while those in the FA85-Cs15 films appear

to be less than 250nm. This is somewhat contrary to the literature, which generally suggests larger grain sizes yield better performance [79]. Unfortunately, all we can say here is that the FA95-Cs5 recipes yield larger grain sizes than the FA85-Cs15 recipe. While microstructure can be an indicator of film quality and cell performance, it is clearly not always the case, and visual film quality and light IV characteristics are more important.

Finally, we note our efficiencies are far below the champion efficiencies achieved with the $MAPbI_3$ recipe. There is a very telling reason for this. Consider the film quality of the PCBM as photographed in Figure X (b). We note very poor wetting, especially with the FA85-Cs15 recipe. The films are splotchy and poorly cover the OHLP film. This was not the case with the $MAPbI_3$ films. It is clear that while CTAB helps the wetting of PCBM on the $MAPbI_3$ surface, now instead it hinders the wettability of PCBM on the FA85-Cs15 surface. The FA^+ ion is very similar in structure to the MA^+ ion, thus one might postulate that it is the presence of the Cs^+ ions on the surface of the OHLP films that reduces the efficacy of CTAB as a surfactant. Either way, this informs our next set of experiments where we consider CTAB-less PCBM.

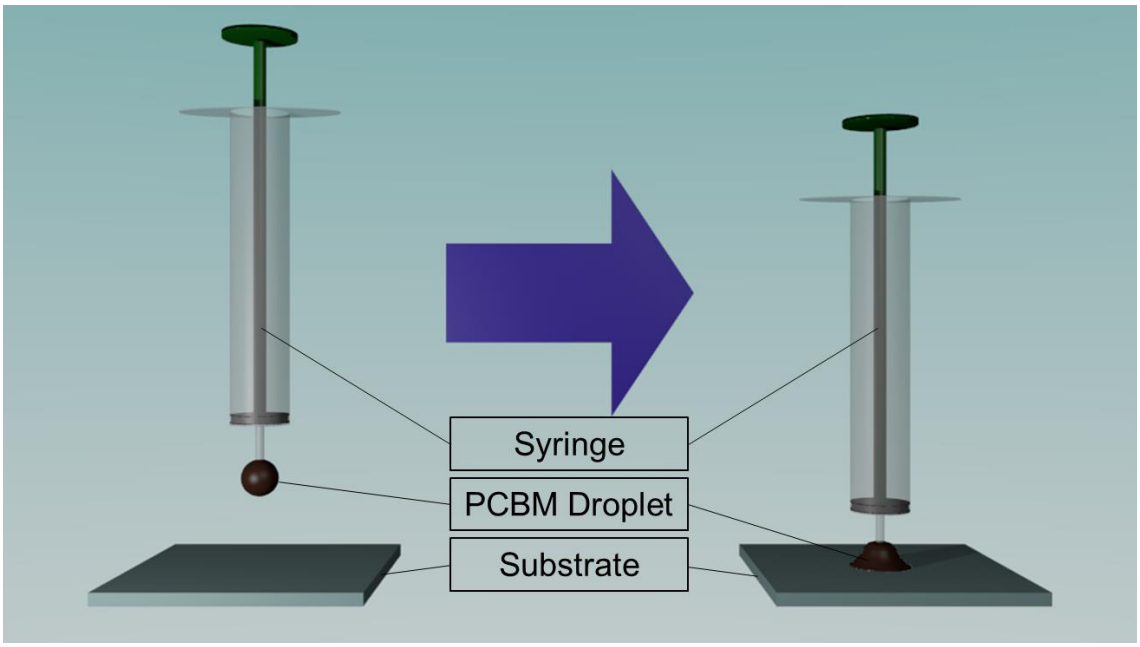

Figure 3.9. Detailing a more careful method of depositing PCBM. Contact of the droplet is made to the slide instead of letting it drip off the syringe tip onto the slide.

In these next two recipes, we consider more carefully how to deposit PCBM on FA85-Cs15 OHLP films. Our first modification to recipe 3 for FA85-Cs15 is to remove the CTAB additive from the PCBM precursor solution. Furthermore, there is some consideration to be had over the dropcast technique when depositing PCMB on the OHLP film. On intuition, we shall consider two, dichotomized possibilities: under the first method, we shall allow a droplet of PCBM precursor solution to fall from the tip of the syringe onto the OHLP film. In the other, we shall avoid the droplet from falling- instead, as depicted in Figure 3.9, we shall allow the droplet of PCBM precursor to form at the tip of the syringe and let that droplet contact the film surface and spread smoothly until it coats the film. We shall refer to these two techniques at the drip technique and the contact technique. The biggest apparent difference is the splash caused by the first method. Light IV data is taken in a similar fashion to the earlier FACs study, and the IV curves are plotted in Figure 3.10., with PCE, FF, V_{oc} and J_{sc} for the forward and reverse sweeps tabulated in Table 3.3.

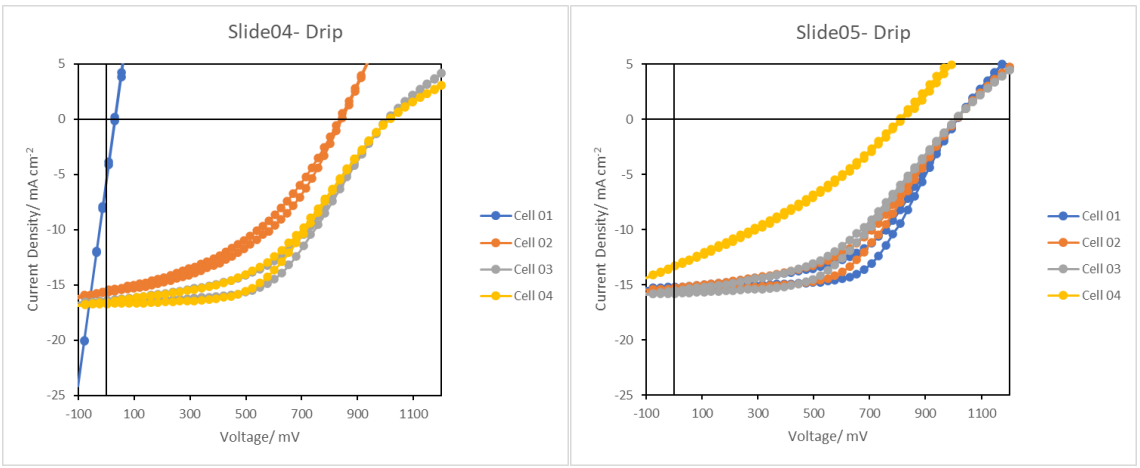

(a)

(b)

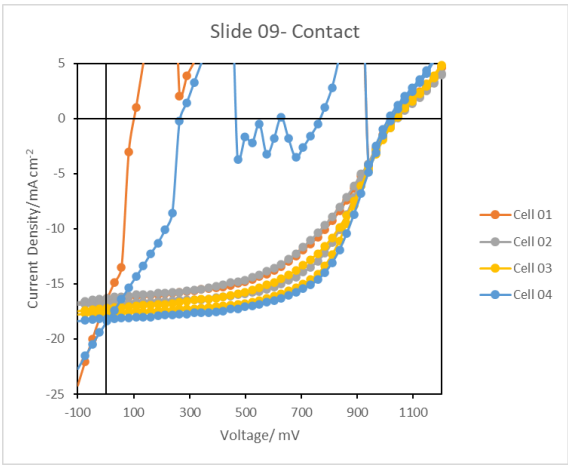

(c)

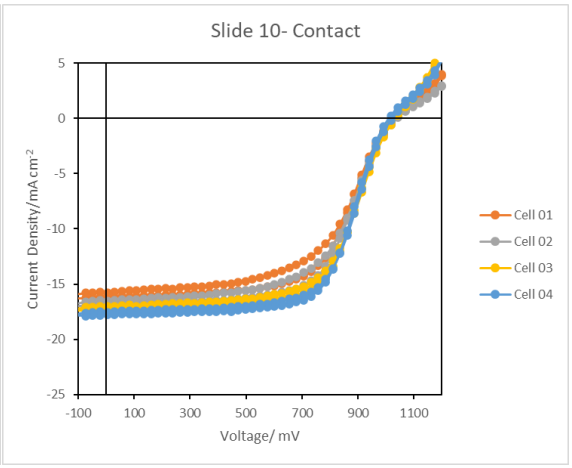

(d)

Figure 3.10. Light IV curves of $FA_{0.85}Cs0.05PbI_3$ cells fabricated with (a), (b) the drip PCBM method and (c), (d) the contact PCBM method.

Referring to the IV data, our first observation to make is that undoped PCBM yields better, more consistent photovoltaic cells than CTAB-doped PCBM when fabricated on our FA85-Cs15 OHLPs. We note higher average and champion PCEs from the undoped PCBM recipes even using the drip method, as well as less shorting compared to the 1.25M FA85-Cs15 cells manufactured with CTAB doped PCBM from the previous experiment (Slides 07 and 09 in Table 3.2. (e) and (f), and Figure 3.8. (e) and (f)). It is clear that CTAB is incompatible with FA85-Cs15 surfaces. However, there are nuances to the elimination of the CTAB. Inspecting the two groups of data, the pure PCBM recipes feature on average higher FF and V_{oc}, but lower J_{sc} than the CTAB-doped PCBM recipes. Furthermore, the S-kinking in the IV curve, absent from all the CTAB-doped PCBM recipes so far, makes a comeback in all the IV curves of the pure PCBM recipes, as seen in Figure X. It is clear that the presence of CTAB is causing poor band diagram alignment, hence the lowered Voc, while the poor PCBM film quality appears to be causing more recombination as well, resulting in a lower fill factor. Yet CTAB is clearly still doing its work as dopant, and its absence is affecting charge mobility in the pure PCBM devices. Though our devices work better, there is a tradeoff in charge extraction.

Putting our focus on comparisons within this experiment, we notice that the contact method (Slides 09 and 10 in Figure 3.10. (c) and (d), and Tables 3.3. (c) and (d)) results in on average a higher performance across the board compared to the drip method (Slides 04 and 05 in Figures 3.10. (a) and (b) and Tables 3.3. (a) and (b)). It is a small step, but a meaningful one. It means that the rheology of the PCBM precursor is relevant to the fabrication process and the final parameters of the device. It is better to allow as little force and impact to be applied to both the precursor and the OHLP surface, and instead it is more favourable to allow the precursor solution to slowly spread across the OHLP surface before spincoating to form the film. It would be very exciting to undertake a rheological study of the PCBM precursor to have a scientific explanation for this phenomenon, unfortunately it lies outside the scope of this work.

Slide 04	Drip Technique			
Finger	PCE/%	FF/%	Voc/mV	Jsc/mA cm^-2
F1F	SHUNTED			
F1R				
F2F	5.45	42.0	835.1	15.54
F2R	5.89	44.6	843.3	15.64
F3F	7.76	46.9	1007.5	16.40
F3R	8.72	52.5	1007.0	16.51
F4F	7.48	44.6	1014.0	16.56
F4R	8.23	48.6	1013.5	16.71
Average	7.26	46.5	953.4	16.23
Std Dev	1.19	3.37	80.83	0.46

(a)

Slide 05	Drip Technique			
Finger	PCE/%	FF/%	Voc/mV	Jsc/mA cm^-2
F1F	7.97	51.4	1012.1	16.32
F1R	9.27	60.1	1014.3	15.21
F2F	7.36	47.6	1010.1	15.30
F2R	8.39	53.8	1011.3	15.41
F3F	6.92	44.2	1008.2	15.51
F3R	7.95	47.7	1008.5	15.78
F4F	3.55	32.6	816.5	13.35
F4R	3.42	31.9	806.1	13.32
Average	6.81	46.2	960.9	14.90
Std Dev	2.03	9.19	86.42	0.92

(b)

Slide 09	Contact Technique			
Finger	PCE/%	FF/%	Voc/mV	Jsc/mA cm^-2
F1F	8.48	50.2	1036.2	16.32
F1R	SHUNTED			
F2F	8.34	49.0	1042.5	16.32
F2R	9.88	56.7	1038.0	16.79
F3F	9.41	52.5	1040.4	17.24
F3R	10.20	58.5	1034.0	17.70
F4F	11.08	59.5	1023.7	18.18
F4R	SHUNTED			
Average	9.57	54.4	1035.8	17.09
Std Dev	4.85	25.5	479.5	7.94

(c)

Slide 06	Contact Technique			
Finger	PCE/%	FF/%	Voc/mV	Jsc/mA cm^-2
F1F	9.13	55.9	1037.7	15.25
F1R	10.15	60.8	1032.1	16.18
F2F	9.93	57.9	1040.0	16.50
F2R	10.77	61.5	1035.6	16.91
F3F	10.95	62.2	1035.0	17.01
F3R	11.40	64.4	1025.8	17.26
F4F	11.58	64.5	1024.1	17.53
F4R	11.81	63.5	1011.8	17.80
Average	10.72	61.3	1030.3	16.81
Std Dev	0.92	3.1	9.3	0.82

(d)

Table 3.3. Light IV data of $FA_{0.85}Cs0.05PbI_3$ cells fabricated with (a), (b) the drip PCBM method and (c), (d) the contact PCBM method.

Anecdotally, successful fabrication of OHLP cells even at a lab scale requires careful process control over seemingly irrelevant aspects such as this PCBM deposition technique. Conversing with various other groups, other factors that have been alerted to our attention include whether all the fabrication was conducted in a single, large glovebox train or as is our case, some of it was conducted in atmospheric air over several rooms. Another insight gleaned from conversations with the community is the global and local temperatures of the glovebox- the heat of the hotplates can affect the spincoating process if these processes occur too close to each other. It is difficult to commit these ideas to academic and peer-reviewed publications as they are often extraneous details that might also be confidential, yet they are crucial to the fabrication of high performing OHLPs. The intention of this simple PCBM experiment is to highlight the importance of resources detailing technical practices for OHLP fabrication.

Throughout both FA-Cs studies we have been careful to include a reverse sweep in our light-IV characterizations, something we failed to do in the previous MA study. It is important to do this for OHLP devices because they exhibit hysteresis. This is a known phenomenon commonly attributed to the fact that ionic species and defects are highly mobile in OHLP films, and drift under an applied electric field, causing the OHLP device to exhibit different light-IV curves on the reverse sweep as opposed to the forward [80]. Indeed, we observe in both Figure 3.8. and Figure 3.10. that the forward and reverse sweeps of all cells exhibit hysteresis and sometimes even break down into noise on the reverse sweep. Film quality is of utmost importance in the fabrication of OHLPs in order to minimize hysteresis. In particular, it is known that migrating ions and vacancies like to accumulate at grain boundaries, which is why having a good grain size to minimize grain boundaries is important [81].

In conclusion, in optimizing our FA-Cs-based OHLP devices, we were able to conduct this study over a larger number of devices, using different formulations and adjusting out methods as necessary, achieving a champion cell efficiency of 11.81%. The fabrication of OHLP devices is highly process-sensitive, right down to practices that can sometimes seem insignificant, and the top transport layer is often dictated by its deposition compatibility with the OHLP surface. Overall, our studies of MA and FA-Cs OHLPs focused on the effects of recipe formula as well as experimental technique, with our primary focus on the effects these methods had on light-IV performance. This was conducted with the intention of developing good fundamentals of fabrication, before delving into the finer scientific phenomena occurring within these devices.

3.5. Modelling the S-kink

Thus far, we have noticed the S-kink fluctuate in and out of the IV curves of our device as we change the recipe of the PCBM and active layer. In this section we attempt to use the open-source time dependant drift-diffusion code General Purpose Photovoltaic Device Model (gpvdm) to capture this S-kink [82] [83] [84]. This code is particularly well-suited towards modelling OHLP devices as it accounts for ion migration by performing time dependant drift-diffusion modelling. It does so by assigning parameters for mobile ion concentration and mobility, allowing an internal electric field to evolve over time as an external voltage is applied.

In our experiments, we note the presence of an S-kink when CTAB is absent from the PCBM later, and its absence when CTAB is added to the PCBM precursor. We know from literature that CTAB acts as a dopant, and as such the main variable we will change is the dopant concentration. We refer to the literatures as well as the gpvdm default model for our density-of-states parameters, which we summarize in Table 3.4. Our device is 100nm ITO/ 50nm NiO/ 300nm OHLP/ 50nm PCBM/ 100nm Ag, and a schematic is shown in Figure 3.11 (a). The green arrows indicate the direction of incident sunlight. Figure 3.11 (b) plots the band diagram for such a device. For this device, a 1-dimensional simulation will suffice as charge transport in OHLP cells is primarily vertical.

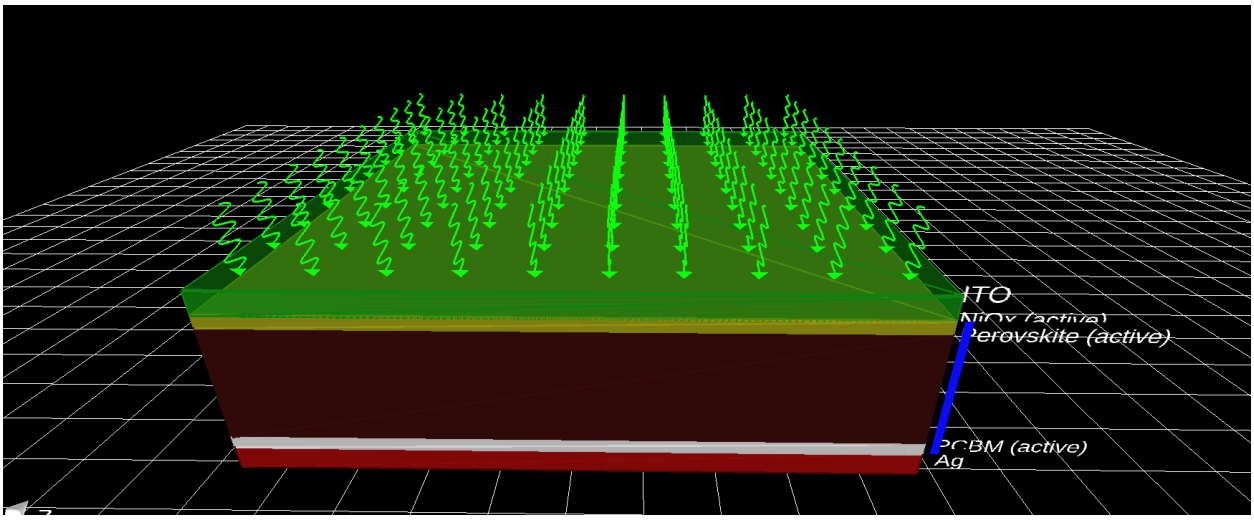

(a)

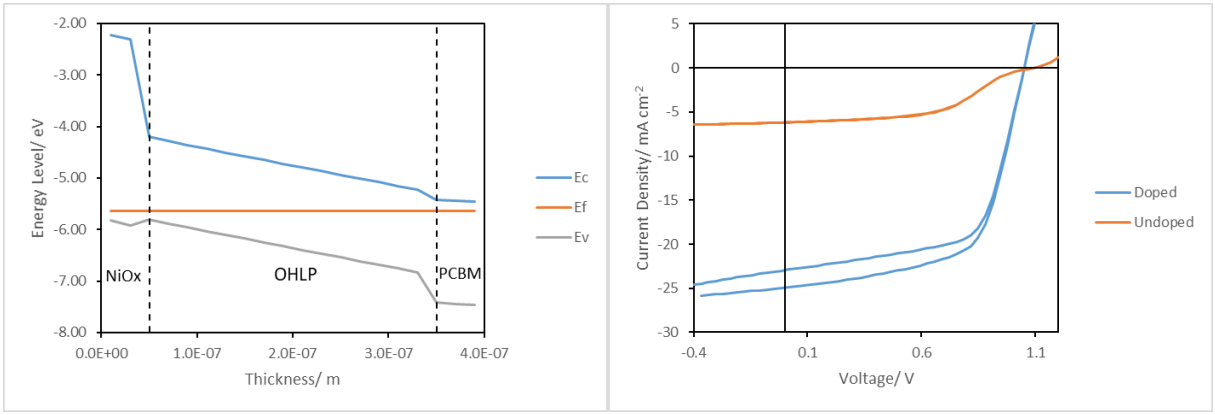

(b) (c)

Figure 3.11. The simulated device's (a) schematic, (b) equilibrium band diagram, and (c) predicted iv curves.

We varied the donor concentration between 1 x 10^{23} m^{-3} and 1x 10^{22} m^{-3} to simulate the effects between a doped layer and a comparatively undoped layer, respectively. The predicted IV curves are plotted in Figure 3.11. (c). We note a lot of similarities between our predicted model here and our experimental findings in Figure 3.5. (e). The doped cell exhibits a lot of similar IV properties to Cells 3 and 4 and more importantly, as a sanity check, exhibits the sort of hysteresis expected out of OHLP devices, proving to us that our model is adequately capturing the ion migration in these cells. More importantly, by reducing the donor concentration by a factor of ten, current density drops drastically, and the S-kink is evidently present. Just like the S-kink in Cell 1 of Figure 3.5. (e), it causes a reduction in fill factor by reducing the voltage at maximum power point. ETL donor concentration clearly plays a big role in ensuring good IV behaviour, so it makes sense that CTAB and other PCBM additives commonly have beneficial effects on the layer. Empirically, we also notice that the S-kink is present in FACs OHLP devices that lack CTAB, like all the drip vs contact PCBM samples in Figure 3.10., while when CTAB was added, although the IV performance was lower, the S kink was noticeably absent from the initial FACs formulation devices in Figure 3.8.

Parameter	NiO	OHLP	PCBM
Thickness/ nm	50	300	50
Electron Trap Density/ $m^{-3}eV^{-1}$	1×10^{25}	1×10^{20}	1×10^{25}
Hole Trap Density/ $m^{-3}eV^{-1}$	1×10^{25}	1×10^{20}	1×10^{25}
Electron Tail Slope/ eV	0.06	0.06	0.06
Hole Tail Slope/ eV	0.06	0.06	0.06
Electron mobility/ $m^2V^{-1}s^{-1}$	1×10^{-7}	1×10^{-4}	1×10^{-6}
Hole mobility/ $m^2V^{-1}s^{-1}$	1×10^{-7}	1×10^{-4}	1×10^{-6}
Relative permittivity	11.75	6.5	4.0
Number of Traps/ bands	5	5	5
Free e to Trap e/ m^{-2}	1×10^{-20}	1×10^{-20}	1×10^{-20}
Trap e to Free h/ m^{-2}	1×10^{-22}	1×10^{-22}	1×10^{-15}
Trap h to Free e/ m^{-2}	1×10^{-22}	1×10^{-22}	1×10^{-15}
Free h to Trap h/ m^{-2}	1×10^{-20}	1×10^{-20}	1×10^{-20}
Eff DoS Electron/ m^{-3}	1×10^{26}	1×10^{26}	1×10^{26}
Eff Dos Hole/ m^{-3}	1×10^{26}	1×10^{26}	1×10^{26}
Ionization Energy/ eV	2.1	3.8	3.9
Band Gap/ eV	3.6	1.6	2.0
Recombination Rate/ m^2s^{-1}	0	1×10^{-15}	0
Acceptor Concentration/ m^{-3}	1×10^{23}	-	-
Donor Concentration/ m^{-3}	-	-	Varied
Mobile Ion Concentration/ m^{-3}	-	1×10^{25}	-
Mobile Ion Mobility/ $m^2V^{-1}s^{-1}$	-	1×10^{-15}	-

Table 3.4. Electrical parameters used in gpvdm time-dependant drift diffusion simulations.

3.6. Conclusion

Through this chapter, we have investigated OHLPs on two levels. Through the first, we focused on the fabrication of OHLP devices, using characterization methods such as light-IV response to ascertain good fabrication recipes and practices to yield devices with champion efficiencies of 12.41% for the MA-based OHLP devices and 11.81% for the FA-Cs-based OHLP devices. We found that beyond the OHLP layer stoichiometry and quality, just as important was the qualities of the precursor solution being deposited on top of the OHLP. Qualities such as wettability and rheology, and their compatibility with the OHLP surface affect the ultimate quality of the top transport layer which affect the final device performance.

Chapter 4: Radiation Tolerance of Perovskites

4.1. Radiation Tolerance of Perovskites

We have shed some light on the manufacture of OHLPs, giving us some understanding of how we may want to incorporate them into flat panel SBSP. Now we seek to characterize them in ways meaningful to flat panel SBSP. As mentioned earlier, a large part of our study on OHLPs is influenced by the literature which has demonstrated OHLPs to be tolerant to both electron and proton irradiation [56]. This makes them an ideal candidate to be used in ultralight, unshielded flat panel photovoltaics for SBSP. On principle, informed with this, we should proceed with ensuring our cells are also radiation hard. However, in our investigations, we have noticed interesting behaviours of our cells when exposed to certain types of radiation, and thus endeavour to pursue testing with this type of radiation damage to shed light on how proton degradation may happen within a perovskite cell.

So far when proton tolerance has been demonstrated in OHLP cells, we note several qualities to these experiments. The energy is in the MeV range, and/or the fluence is below 10^{13} $p^{+}cm^{-2}$ [85] [86] [87]. This is done to simulate the expected 10-year lifetime exposure of the most damaging proton radiation a solar cell should expect, which for the MeV range should be around 10^{12} $p^{+}cm^{-2}$ [88]. This is of course, important in determining whether a cell is able to withstand reasonable time in the radiative background of space. However, it does not capture the full picture of what is going on. In other studies, we note that in fact, low energy protons within the 50keV range are capable of damaging the OHLP cells at fluences of above 10^{12} $p^{+}cm^{-2}$ [56] [89]. Even if anneal recovery can be demonstrated, it is still worth noting that significant degradation is observed in these cells first. As such, it is of considerable interest to us to study the degradation of OHLP cells under ~50keV range at high fluences.

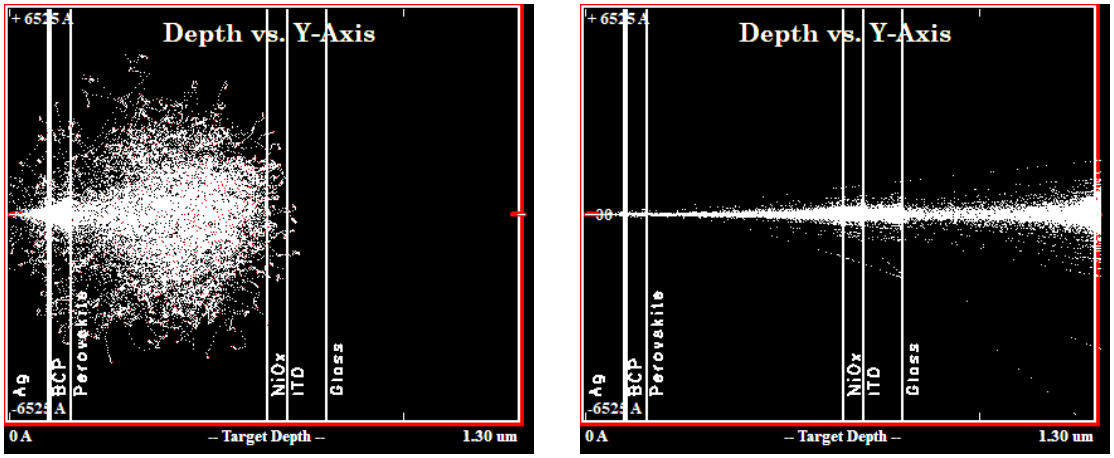

(a) (b)

Figure 4.1. Proton penetration depth profile at (a) 50keV and (b) 100MeV.

Being a little more specific, there is a key phenomenon we hope to investigate by focusing on this energy range of protons. Consider the plots in Figure 4.1. These are predicted depth profiles of proton impingement calculated using the Monte Carlo-based code Stopping Range of Ions in Matter [90]. Two different energies are shown: 50keV and 1MeV. Protons are irradiated incident on the back contacts to better show how far through an unencapsulated cell the protons will be deposited. ~50keV protons are seen to be deposited mostly in the OHLP layer while 1MeV protons pass through and are deposited in the

glass substrate layer. There is a hypothesis to be formed here. Damage to the OHLP device seems most pronounced when protons are deposited in the OHLP layer itself. As such, in investigating high fluence, low energy proton radiation, we seek not to qualify the OHLP solar cell for SBSP, but rather to investigate the nature of proton degradation on OHLP cells by pushing them to further fluences. Doing so will deepen our understanding of how an OHLP cell is damaged by protons, giving us a clearer picture of the full design space when designing OHLP cells for flat panel SBSP.

In addition, as we covered in Chapter 3, an OHLP solar cell does not comprise the OHLP film alone, but instead is a heterostructure comprising at least 4-5 different films of material. In deepening our understanding of OHLP device degradation, it is important to characterize the degradation of the individual materials. By observing the degradation of key parameters such as resistivity and optical transmissivity under increasing fluences of proton radiation, we can firstly assess if they are suitable candidates for the unshielded space conditions we wish for our flat panel SBSP, and secondly we may take those parameters and calculate their theoretical effects on the solar cell. Materials we wish to focus on are the ETLs, HTLs and transparent conducting layers (TCLs) used at the top electrode. Specifically the ETLs and HTLs we have chosen are used in devices we will actively be testing, as well as other materials commonly used in OHLP devices. The ETLs we will study are PCBM and perylenetetracarboxylic diimide (PTCD-i). The HTL we will study is NiOx and the TCLs we will study are ITO and poly(3,4-ethylenedioxythiophene) (PEDOT).

4.2. Stopping Range of Ions in Matter

Earlier we presented two Monte Carlo simulations predicting the different depth profiles of proton deposition using two different energies. We also made mention of our intention to subject not only the OHLP solar cell to ~50keV radiation, but also its constituent HTLs, ETLs and TCLs. In this section, we conduct calculations on all these structures so we may visualize what sort of damage to expect from our proton irradiation experiment. For this simulation, we have selected 30keV and 75keV as the two low energies we wish to study. It will be useful to have a second low energy profile to study, and we have existing 30keV data from a previous study [56]. We will eventually see that choosing these two energies will pay off in our discussion of the final results as well.

Figure 4.2. presents the depth profiles of the OHLP cells in visual form as well as graph form of each of our desired materials as well as the OHLP cell we will be using, for each energy level. We repeat these simulations for the other thin films as well, but for brevity we will put these in the Appendix B. Note that in the pictorial plot a simulation with 10^3 protons was used while in the graphical plots a simulation with 10^4 protons was used. The former was chosen for the pictorial visualization to keep the number of proton trajectories low, allowing for easier visualization of the interaction volume. The letter was chosen for the graphical plot in order to sample more trajectories for a better statistical view.

Scanning across these plots, we note that most of our desired conditions will be met. Bulk of the protons will indeed be deposited in the OHLP for the full cell testing, and for the individual films, a decent proportion of protons will still be deposited in them while majority still pass through them- something that also seems to be happening to the HTLs, ETLs and TCLs in the OHLP cell itself. We consider these conditions to be satisfactory to begin giving us a picture of whatever may be happening.

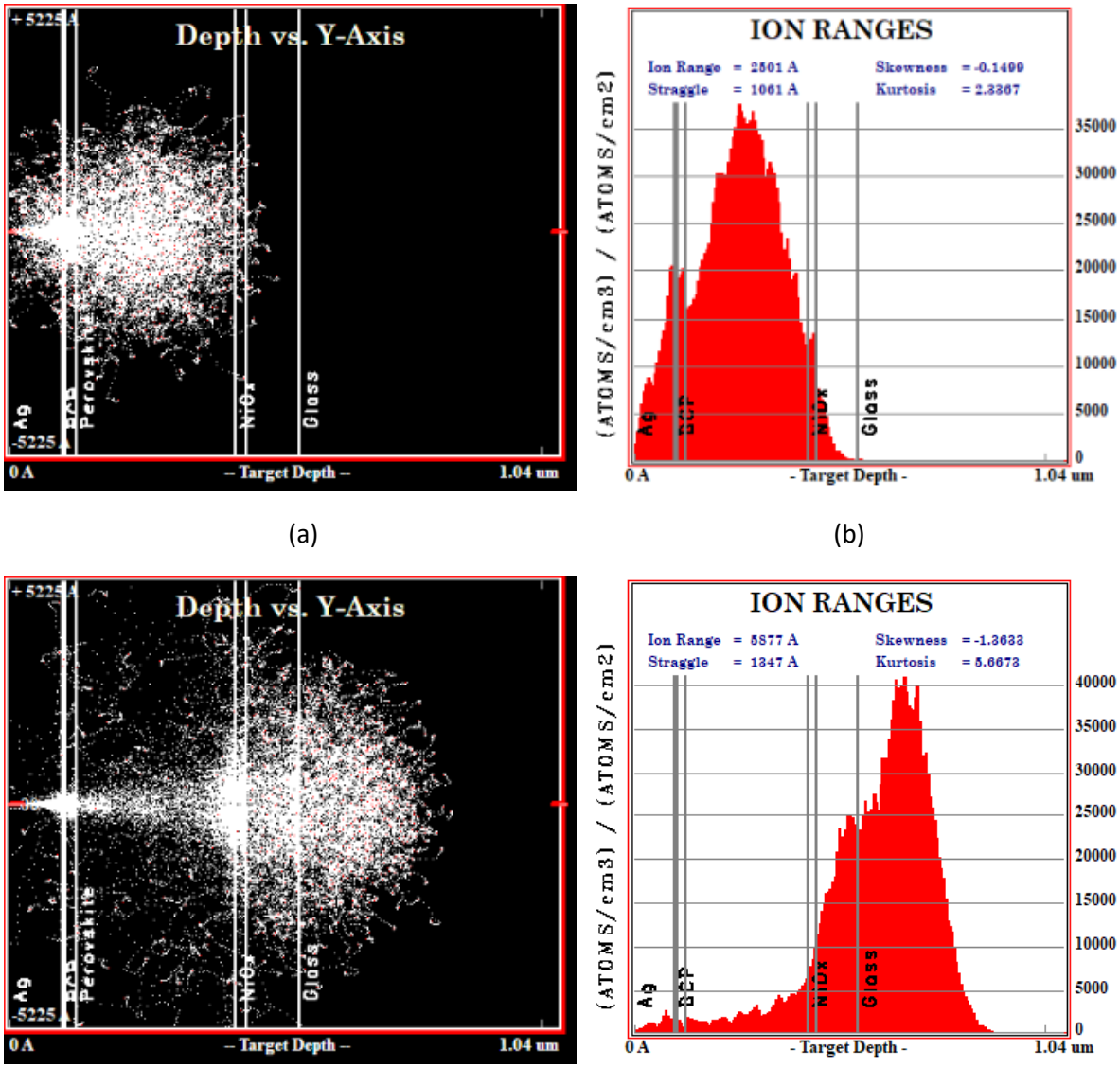

Figure 4.2. SRIM calculations predicting proton depth profiles of (a), (b) 30keV protons and (c). (d) 75keV protons deposited.

Observing the differences between the 30keV and 75keV deposition profiles in Figures 4.1 (a) and (c), we also noted that in the case of the 30keV irradiation, most of the irradiation is deposited in the PCBM and OHLP layers, whereas in the 75keV case, most of the protons are deposited in the ITO and glass layers. This is good for us, as it should give rise to two energies that will yield different trends.

As for the rest of the single film devices, from the plots in Appendix B, some protons will get deposited in the films so we should see some effect on them. With this analysis complete, we proceed with the confidence that our planned modes of irradiation should indeed yield scientifically interesting results.

4.3. Thin Film Characterization

In this section, we report the methods and techniques used to characterize the ETLs, HTLs and TCLs. We also report the results of our radiation study on these materials and predict the impact the degradation of these films will have on an average OHLP solar cell's performance.

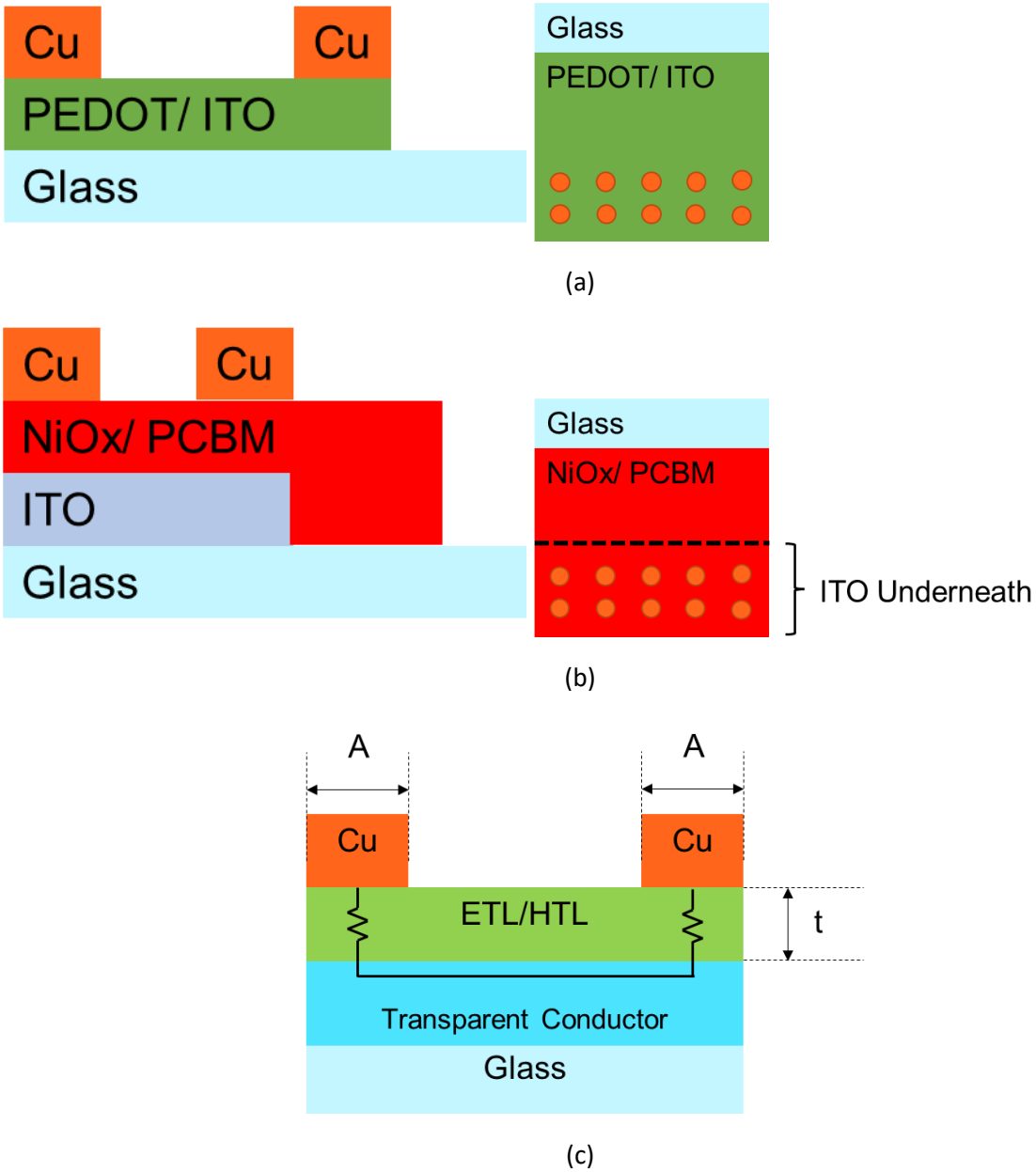

Figure 4.3. Cross sectional and top-down schematics of the testing structures used for (a) TCLs and (b) ETLs and HTLs. We also consider (c) the electrical path of the 2-point probe experiment conducted on samples in (b).

In order to effectively characterize our samples, we have developed a testing architecture that allows us to effectively and succinctly measure our samples. As mentioned earlier, two key parameters we wish to begin looking at for these individual films are electrical resistivity and optical transparency. As such, we

consider the schematics of devices illustrated in Figure 4.3. For the TCLs themselves, as they are usually thick and conductive to allow for lateral transport, we simply deposit them onto a glass slide and gate them with contacts. The regions of TCL/glass allow us to shine light through to measure their optical transmissivity, while a line of the 4 contacts allow us to measure electrical resistivity between them using a 4-point probe method. The ETLs and HTLs require a little more thought. These materials are often less than 50nm thin in the OHLP devices and thus have very little lateral transport on the order of millimeters are they are very resistive [91]. As such they will be fabricated on a glass substrate that has a strip of ITO on it. This allows for adjacent contacts to be contacted in a 2-point resistance measurement as depicted in Figure 4.3. (c), where the current passes vertically through a volume of ETL/HTL of cross-sectional area A equal to the contact pad area and thickness t, through the base ITO layer, and up through another similar volume of ETL and HTL. If the ITO thickness can be subtracted, we arrive at the resistance of a volume of material of cross-sectional area A and length 2t, which allows us to find the resistivity of the HTL/ETL. Having only a strip of Ito cover the material means there is an area of the slide which is just the material and glass, eliminating the ITO's effect on the measured transmissivity spectrum. It is via these testing structures that we will characterize our devices.

Having elaborated on the nature of these testing structures, we set about fabricating and measuring them, before and after irradiation. For the ITO samples, we obtained with 15x15mm ITO-on-glass substrates from Solarmer. These substrates featured a strip of ITO across the centre, with exposed areas of glass, allowing the glass background to be taken in isolation of the ITO and glass. We deposited 100nm Cu circular contacts on them via electron beam deposition at a rate of $1 Å s^{-1}$ through a shadow mask. For the PEDOT samples, a collaborator fabricated them on a glass substrate. For the NiO_x samples, the recipe covered in Chapter 3 was used: a NiO_x precursor of 248 mg of nickel (II) acetate tetrahydrate ($(CH_3COO)_2Ni \cdot 4H_2O$) and 0.06 ml of ethanolamine ($NH_2CH_2CH_2OH$) were dissolved in 10 ml of ethanol and aged overnight, then 50 µl of this precursor solution was spincoated on the ITO-on-glass slides at 3000 rpm for 60 s. These slides were then annealed at 300°C for 60 min on a hotplate in a fume hood. 100nm Cu circular contact were deposited using the aforementioned methodology. For the PCBM samples, a different method was used. PCBM powder was placed in a crucible and 10nm of film was thermally evaporated in a vacuum chamber. Then Cu contacts were deposited. Finally, PTCD-I was deposited on ITO-on-glass substrates from a collaborator by thermal evaporation.

Once these samples were fabricated, the ITO and PEDOT samples underwent 4 point probe resistivity testing [92] with a Keithley voltammeter. A row of 4 Cu contacts was selected, a source current was passed through the outer two contacts and the voltage across the inner contacts were measured. To the ETL and HTL film samples, from a row of 5 Cu contacts, 4 pairs of two adjacent contacts were selected and to each, a 2 point IV sweep was conducted from -1V to 1V using a Keithley voltammeter. In addition, because the ETLs and HTLs were fabricated on similar ITO-on-glass substrates, this same 2 point resistance measurement was repeated on earlier ITO samples to obtain a background resistance from contact and electrode resistance.

The optical measurement of all the samples was a lot more homogenous. For each of these samples, an area of pure exposed glass and an area that comprised the film and the glass substrate were selected and transmission measurements were taken using a Silicon photodiode. A background of air was taken, then the transmission spectra of these two areas were taken from 300nm to 1100nm. A secondary Silicon photodiode was used to record a fraction of the monochromated light, separated via a beamsplitter pre-incidence, in order to account for fluctuations in signal strength.

These samples were then sent to collaborators at Boeing Radiation Effects Labs [93] where 6 samples were subject to proton irradiation. For each material, 3 samples were subject to 30keV protons to fluences of 4.3 x 10^{13} p^+ cm^{-2}, 8.6 x 10^{13} p^+ cm^{-2} and 1.3 x 10^{14} p^+ cm^{-2}, respectively, and the other 3 samples were subject to 75keV protons to the same set of fluences. Post irradiation, all the electrical and optical measurements described before was repeated, giving us a full set of resistance, resistivity, and transmissivity measurements before and after radiation.

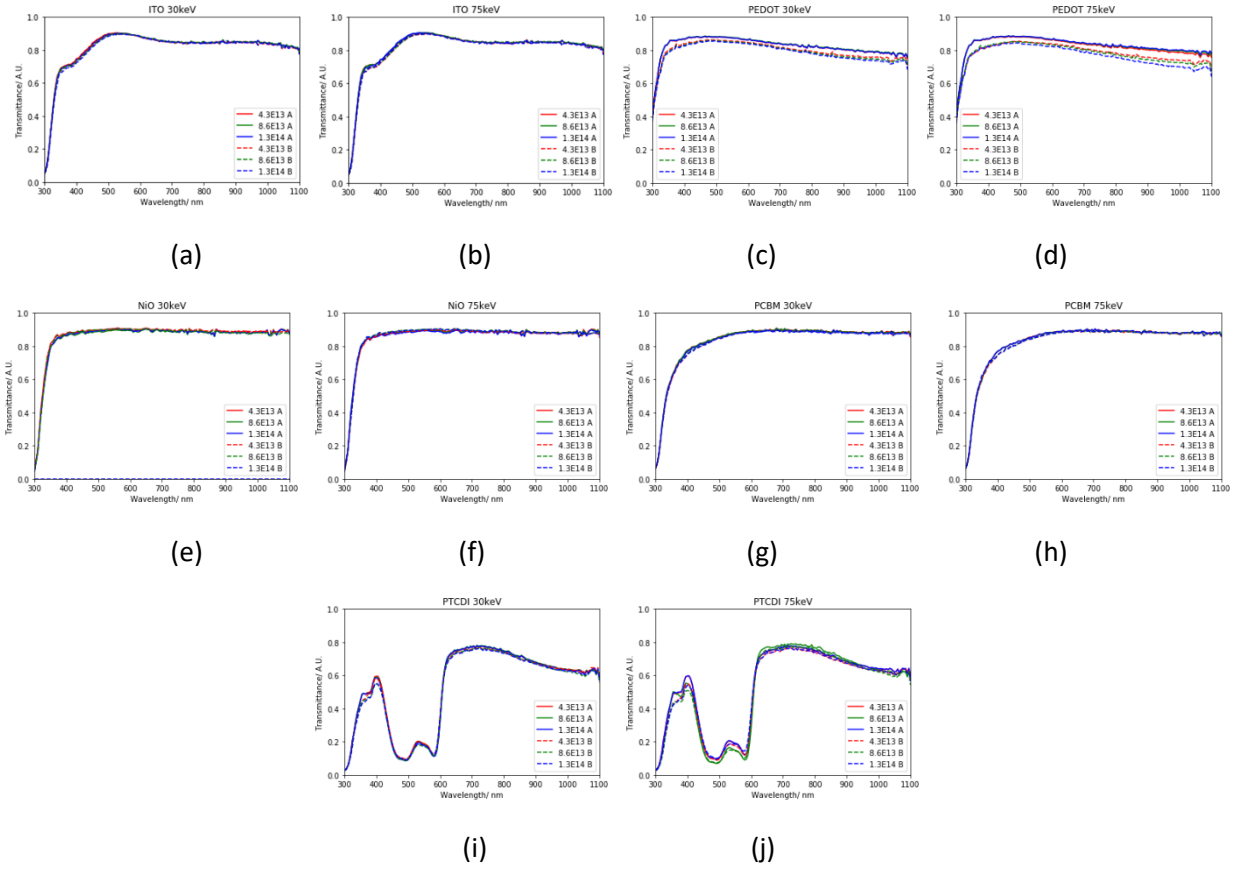

Figure 4.4. Before and after transmission spectra of films of ITO subject to protons of energy (a) 30keV and (b) 75keV, films of PEDOT subject to protons of energy (c) 30keV and (d) 75keV, films of NiO subject to protons of energy (e) 30keV and (f) 75keV, films of PCBM subject to protons of energy (g) 30keV and (h) 75keV, and films of PTCD-I subject to protons of energy (i) 30keV and (j) 75keV.

Figure 4.4. summarizes the transmission spectra of the samples before and after radiation at each proton energy level. Figure 4.5. summarizes the resistivities of ITO and PEDOT, while Figure 4.6. plots the device resistances (averaged with errorbars) of ITO, NiO_x, PCBM and PTCD-I at each proton energy level before and after radiation. We have chosen to report the device resistance instead of a post-processed resistivity for the ETL and HTL devices. Across 4 devices per sample (remembering 1 sample is exposed to 1 unique fluence), there is some variance owing to both film quality variation and contact resistance, as can be seen from the errorbars in the resistance plots, and this is also observed in the measurement of ITO. Subtracting the average base ITO resistance from the average device resistance will introduce further variance which will make for inaccurate analysis and poor data reporting.

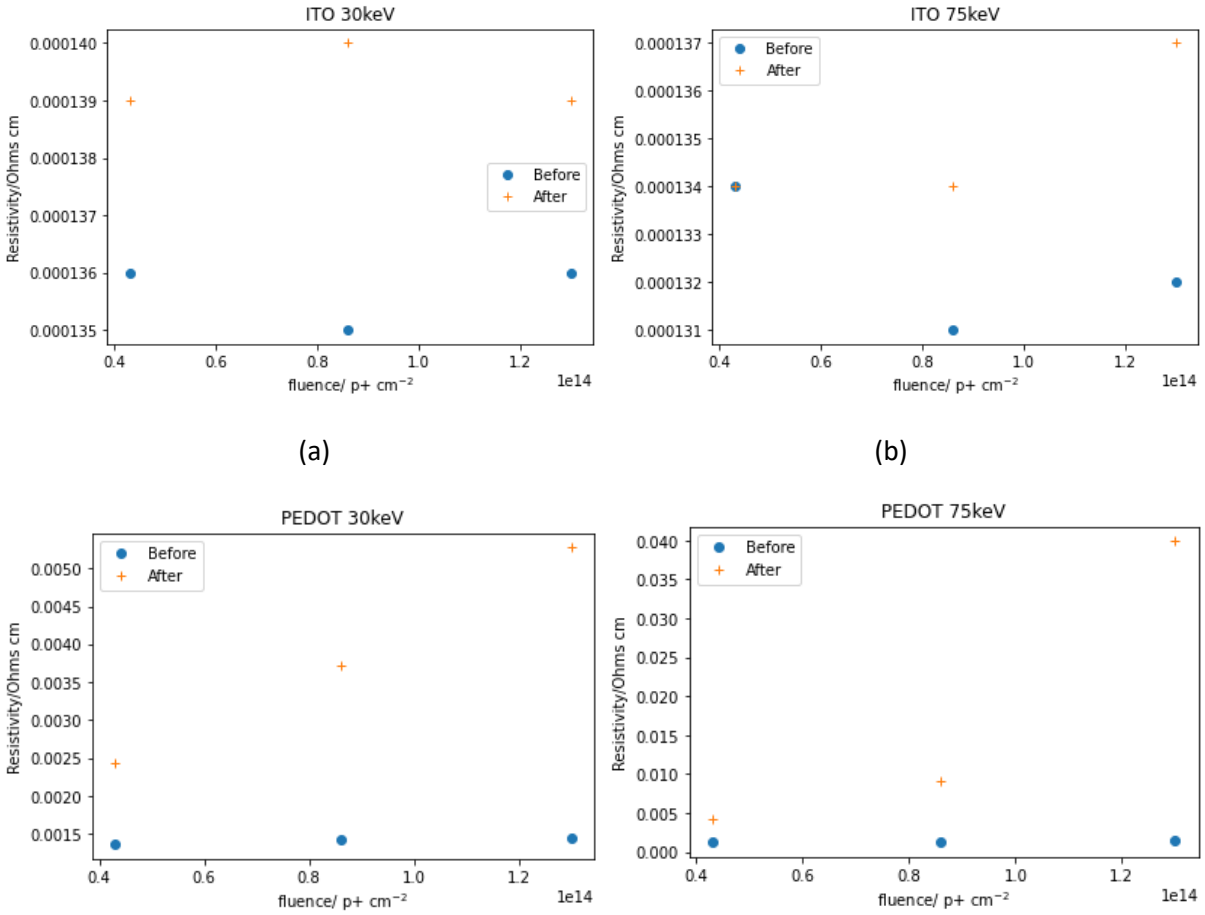

Figure 4.5. Before and after 4-point resistivity measurements for films of ITO irradiated by protons at (a) 30keV and (b) 75keV and those of PEDOT by protons at (c) 30keV and (d) 75keV.

Also somewhat unfortunately, the NiO_x sample subject to 30keV protons at fluences of 1.3 x 10^{14} p^+ cm^{-2} shattered during handling and as such we are missing a datapoint on this front.

Viewing all this data in aggregate, we note some important trends. First off, PEDOT degrades the most, both optically and electrically. The transmission spectra become notably opaquer with increasing fluence at both energies, and resistance increases by several orders of magnitudes as fluence increases. No other material experiences such a relative increase in opacity and resistivity, most of them instead only at most doubling in resistance or resistivity. PEDOT as a material degrades a lot when exposed to low energy, high fluence of protons. Amongst this roster of materials sampled, it is the least compatible material for flat panel SBSP. This is somewhat unfortunate, as PEDOT is one of the more popular TCLs for the sort of flexible OHLP cells that we intend to fabricate for flat panel SBSP. ITO is a lot more rigid and brittle in comparison [94] [95]. Moving ahead one is motivated to perform this study on more TCLs such as graphene and Ag nanoparticles to try and find a flexible, radiation resistant TCL [96].

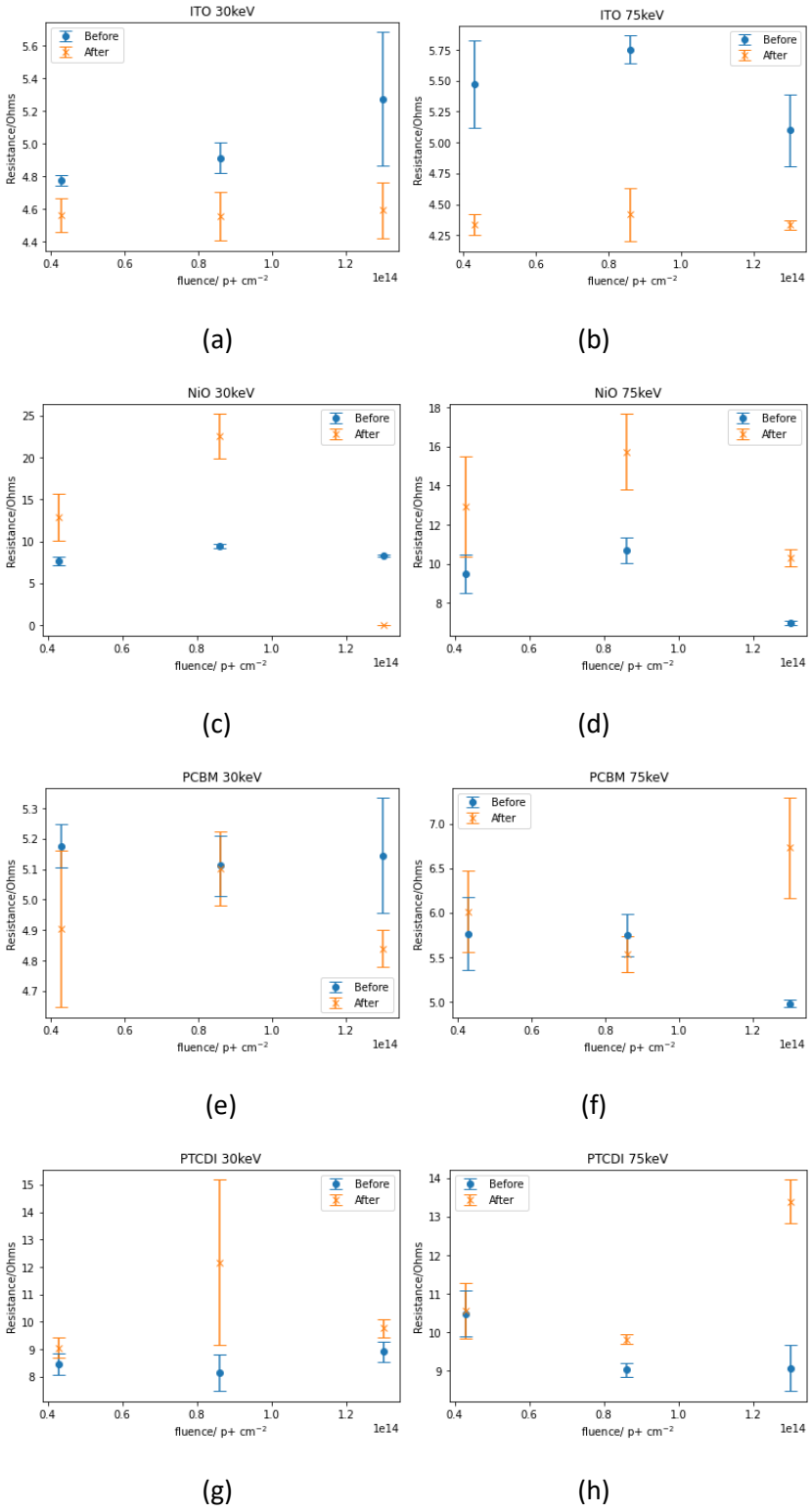

Figure 4.6. Before and after resistance measurements of gated films of ITO irradiated by protons at (a) 30keV and (b) 75keV, those of NiO_x by protons at (c) 30keV and (d) 75keV, PCBM by protons at (e) 30keV and (f) 75keV and PTCD-i by protons at (g) 30keV and (h) 75keV.

Somewhat alarming may be the transmission spectra for PTCD-i. It appears to be intrinsically very opaque. However, one need not worry too much, as PTCD-I is usually used as the bottom ETL and does not take part in active attenuation of sunlight reaching the OHLP absorber, and at best only attenuates back reflected light.

Across the board, more damage is observed at 75keV than at 30keV. On a material level, referring to the Monte Carlo simulations in Appendix B, we see that more of the protons pass through the active material film at 75keV than 30keV. In other words, the type of damage done to these thin film materials is collision-based.

We seek a way to quantify the effects of these observed degradation on the final performance of the solar cell. We will now spend some time developing two models to express these increases in resistance and transmissivity to efficiency.

Internal resistance is known to have considerable effect on a solar cell. If the transport layers are too resistive, then the photocurrent will be lost during the simple process of extracting them from the cell as holes and electrons need to pass through more resistive layers. Assuming zero shunt paths form during proton degradation, the effects of increased series resistance can be best expressed in the Shockley diode equation as written in equation 4.1 [97]. What this means for us is that we have a direct way to generate an IV curve that reflects the increase in resistance. From there we can find the change in efficiency of the cell. Mathematically, our methods are as such: we express all our materials in R·A of units Ω cm^2. For ITO and PEDOT this means multiplying the resistivity by the film thicknesses, and for the NiO_x, PCBM and PTCD-i this involves first subtracting the ITO resistance (hence the additional resistance measurements for ITO as shown in Figures 4.6. (a) and (b)), then multiplying the resistance by cross-sectional area and dividing by two (to account for the fact that a length of 2t is crossed). This somewhat contradicts our earlier mentioned hesitance to subtract the ITO background, but we are more willing to do so here as we are making predictions using theoretical models with a fair number of assumptions whereas earlier we were reporting empirical data.

With all our area resistivities assembled, we go through each materials' resistances before and after radiation for each energy level and fluence, plugging them as the series resistance in equation 4.1. to generate a theoretical IV curves before and after radiation. Note here that for each calculation we assume that the entirety of the series resistance comes from one single material. We do so in order to highlight the effect on efficiency from a single material's increase in resistance. In doing so we can conclude which material's degradation affects the cell the most. We simulate a theoretical OHLP with a J_{sc} of about 35 mA cm^{-2}, a V_{oc} of about 1.1V and efficiency of about 20%, something our own cells will later demonstrate. Figure 4.7. summarizes the predicted efficiency before, efficiency after, and normalized loss in efficiency. We note that across the graph, despite all the devices exhibiting some amount of resistance degradation in Figures 4.5. and 4.6., all this degradation will not cause a high performing OHLP to lose more than 0.01 of its initial efficiency. The code used to generate this data, and the table of results, may be found in Appendix C.

$$\mathrm{I} = I_L - I_0 \exp\left[\frac{q(V + IR_S)}{nkT}\right] \qquad 4.1.$$

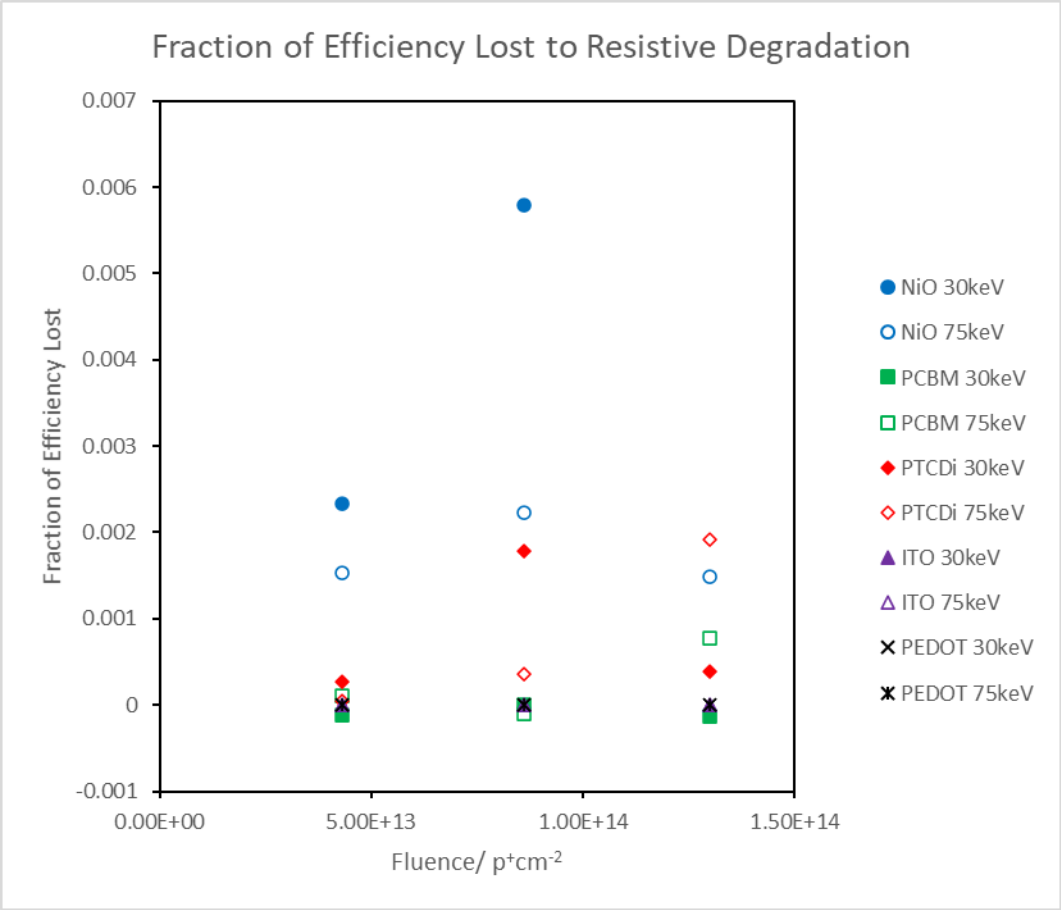

Figure 4.7. Predicted fraction of efficiency lost to resistance degradation.

We now attempt to model the optical losses. When a transport layer above the OHLP absorber darkens, it attenuates the amount of light reaching the absorber layer. Less photons at every wavelength reaching the absorber layer means that the photocurrent generated at that wavelength is lower. We know that the photocurrent is proportional to the spectrally integrated product of the photon flux and the external quantum efficiency (EQE). It is the photon flux that is attenuated when a layer darkens, as such we will multiply the photon flux by the transmissivity before and after radiation. This leads to the equation as expressed in equation 4.2. From there, since photocurrent is proportional to efficiency, the normalized difference in photocurrent is equal to the normalized difference in efficiency. For our EQE spectrum, we measure the EQE of a cell to be used for radiation later. For our solar illumination, we use an AM0 spectrum [5]. These spectra, along with the code used to perform these calculations and results, may be found in Appendix D. We thus tabulate the normalized loss in a similar fashion in Figure 4.8. This is where we see more pronounced effects from PEDOT's degradation, reducing efficiency as much as 0.057. However, for most of the other materials, we note once again that the loss is less than 0.01.

$$J_{SC} = -q \int EQE(\lambda)\phi(\lambda)T(\lambda)d\lambda \quad 4.2.$$

$$\eta \propto J_{MPP} \propto J_{SC} \quad 4.3.$$

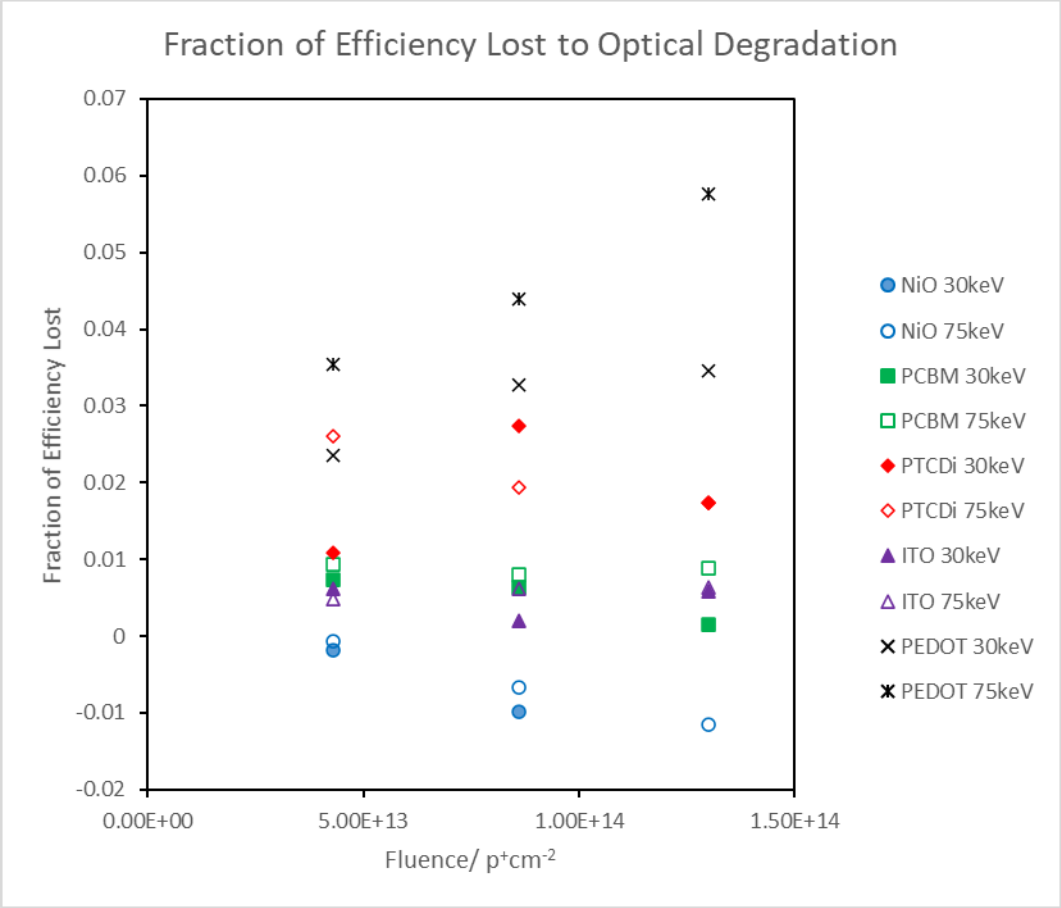

Figure 4.8. Predicted fraction of efficiency lost to optical degradation.

Through this study we surveyed a roster of ETL, HTL and TCL materials commonly used in OHLP cells to investigate their individual radiation hardness in terms of electrical resistivity and optical transmissivity. In order to quantify the effects of this degradation one should expect on a cell, we developed two models to calculate the effect on efficiency. We found with most materials one should expect degradation of less than 1%. However, with PEDOT degradation of up to 5% can be expected. This can be significant degradation, and as such PEDOT is not very suitable for flat panel SBSP applications. In the next section, we will subject full OHLP cells to low energy, high fluence proton irradiation in order to contextualize whether or not all this material degradation is significant.

4.4. Proton Irradiation of Perovskite Cells

In this section we aim to irradiate full OLHP solar cells with low energy high fluence protons. The two key characteristics we aim to see before and after irradiation are the light IV curve and the EQE. These two parameters are key performance metrics of a solar cell.

Cells were fabricated by a collaborator in Caelux Corporation. The final cell stack is Glass/ ITO/ NiO_x/ OHLP/ PCBM/ BCP/ Ag. BCP is usually very thin, about 5nm thick [98]. However, the rest of the layers are conveniently enough all layers we have examined in the previous section, allowing us to piece together the exact nature of proton degradation of OHLP cells.

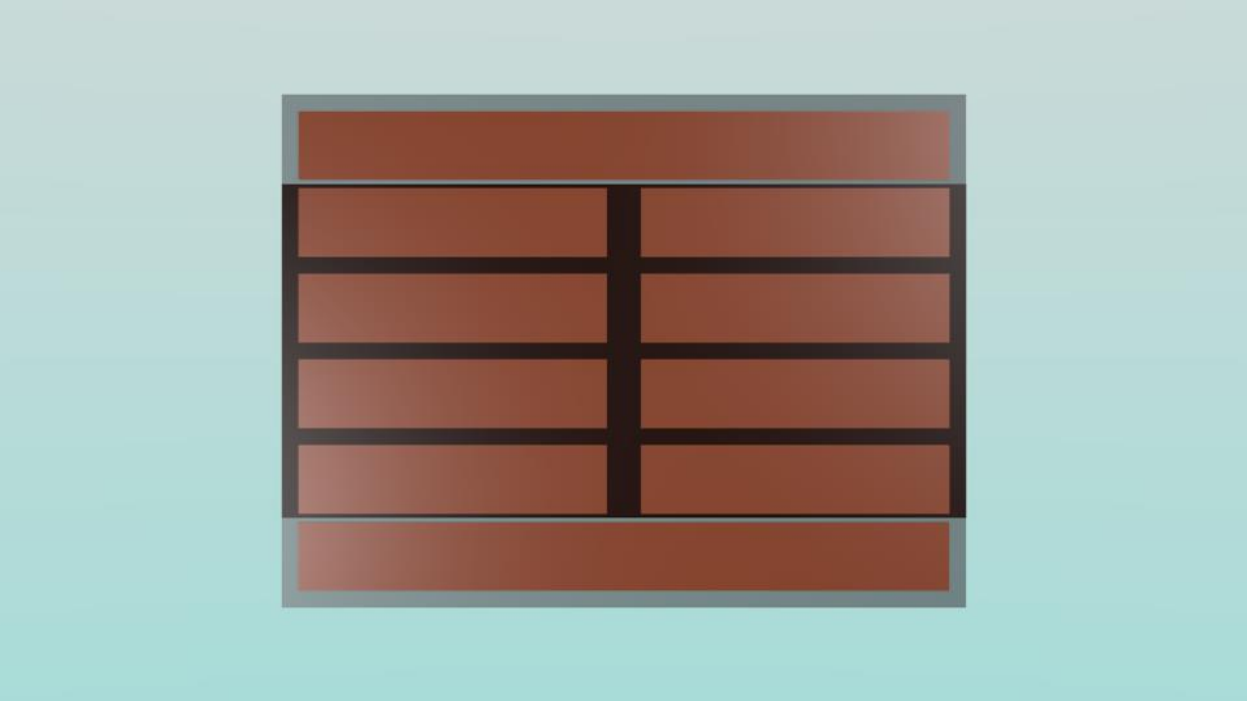

Figure 4.9. Diagram showing the schematic of the eight OHLP cells on a slide. Each cell is the cross-sectional area where the top fingers overlap the ITO film underneath.

Nine OHLP slides with the schematic shown in Figure 4.9. were subject to the following characterization. An ABET solar simulator was outfitted with an AM0 filter and calibrated to the AM0 intensity using a Spectrolab XTJ isotopes CIC-GaAs reference cell. Light IV curves of the cells were recording using a Keithley voltammeter, sweeping forward from -0.4V to 1.2V and then in reverse. The EQE spectra were measured as such. Using the light IV data, a champion cell was selected from each slide, and monochromated light was focused onto a spot on the cell. The resultant photocurrent at each wavelength was measured and normalized against the spectra of a calibrated Si photodetector under the same illumination. A single cell was selected per slide to minimized air exposure during measurement, which could take up to 20 minutes to sweep across the whole spectrum. The cells were then sent with the aforementioned thin film samples to BREL for proton irradiation. 4 samples were subject to 30keV protons to fluences of 4.3×10^{13} p^+ cm^{-2}, 8.6×10^{13} p^+ cm^{-2}, 1.3×10^{14} p^+ cm^{-2} and 1.7×10^{14} p^+ cm^{-2}, respectively, and another 4 samples were subject to 75keV protons to the same set of fluences. The final slide was used as a control to ensure all degradation observed in the other cells was due to radiation damage. When the samples came back, the same characterization was performed on them.

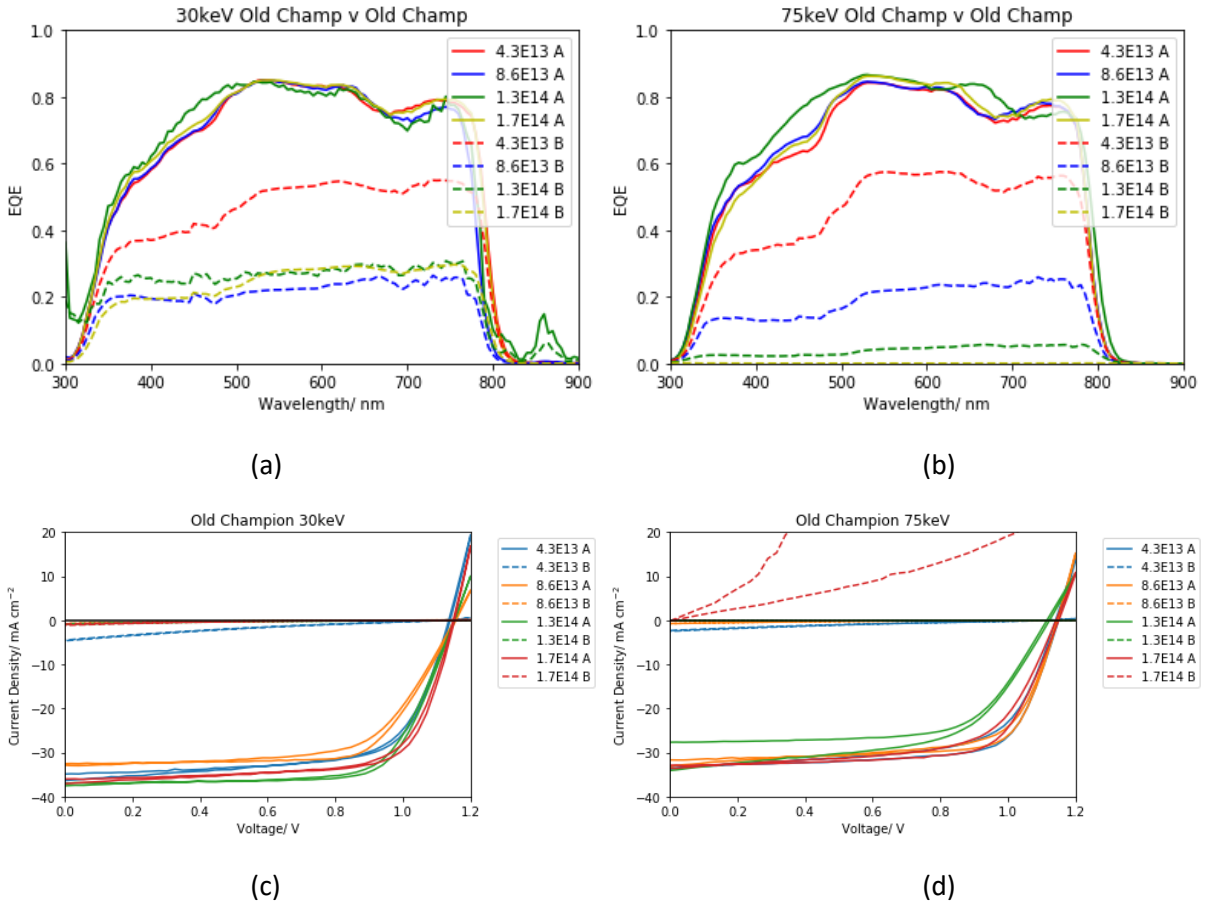

Figure 4.10. Before and after plots of light IV curves of cells subject to (a) 30keV protons and (b) 75keV protons, and of EQE spectra of cells subject to (c) 30keV protons and (d) 75keV protons. An A suffix indicates pre-irradiation, and a B suffix indicated post-irradiation.

Figures 4.10. (a) and (b) shows the light IV curves of the champion cells before and after irradiation at 30keV and 75keV proton energy, respectively. Figures 4.10. (c) and (d) show the EQE spectra of the champion cell in a similar fashion before and after irradiation at 30keV and 75keV protons, respectively. From these figures one sees immediately that increasing the fluence of protons increases the amount of degradation of OHLP cells. In order to have a clearer visualization of the degradation trends, we took the post-irradiation PCE, FF, J_{sc}, V_{oc} and spectrally integrated EQE from this dataset and normalized them against their respective pre-irradiation data and plotted them in Figure 4.11.

Reviewing these trends, we note that the curves of J_{sc} and spectrally integrate EQE against fluence take a similar shape to that of PCE against fluence. In comparison, FF and Voc do not degrade as quickly with fluence as the other two parameters. Degradation is driven by the OHLP's efficiency in absorbing photons and generating a photocurrent. We recall in Figure 4.2. where we show that at 30keV and 75keV, under proton irradiation incident on the Ag electrode side, protons are predicted to be deposited in the OHLP layer. We also note that the light IV degradation is much higher than the ~1-5% degradation predicted under our models in section 4.3. It is clear that the ETLs, HTLs and TCLs themselves are not a significant contributor. Finally, we note that the EQE spectra degrades evenly across the spectrum, with little blue-dominant or red-dominant degradation. All this evidence points towards the conclusion that bulks of the

degradation occurs due to the presence of protons being deposited in the bulk of the OHLP absorber layer, which impedes the material's ability to generate a photocurrent. The relative contribution of the other layers in this device is very small.

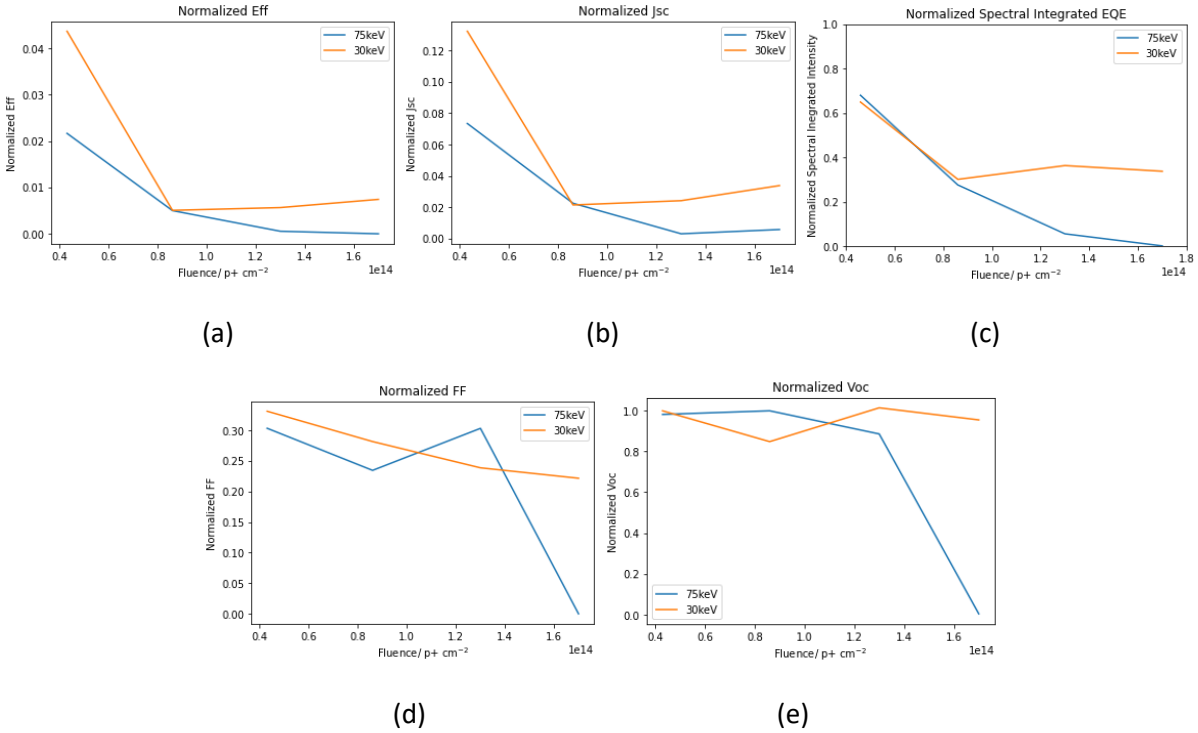

Figure 4.11. Fluence-dependant post-irradiation trends of (a) PCE, (b) J_{sc}, (c) spectrally integrated EQE, (d) FF, and (e) V_{oc} normalized against their pre-irradiation values.

Having identified the proton degradation of OHLP cells as being absorber-layer dominant and due to the presence of proton species in the bulk, we now scrutinize our data a little to delve into possible mechanisms causing this degradation. Specifically, there is an immediate discrepancy between our data. The normalized J_{sc} loss is not equal to the normalized spectrally integrated EQE. Normally this should be the case. Consider equation 4.4. which relates J_{sc} to EQE. Jsc is proportional to the spectrally integrated EQE. This makes sense, as the photocurrent extracted from a device is dependant on the material's ability to turn photons into charge carriers. In fact, in measuring EQE we are measuring the current signal generated at every wavelength of light. Ergo, normalized J_{sc} should in fact be equal to normalized spectrally integrated EQE, as shown in equation 4.5. We in fact see that this is not the case, and that J_{sc} degrades an order of magnitude more than spectrally integrated EQE. In fact, this directly contradict the usual observation in literature, where J_{sc} is usually instead higher than EQE [99]. It is important to consider reasons why this discrepancy arises, as it will inevitably inform the nature of degradation we observe.

$$J_{SC} = -q \int EQE(\lambda)\phi(\lambda)d\lambda \qquad 4.4.$$

$$\frac{J_{SC,Post\ Irradiation}}{J_{SC,Pre\ Irradiation}} = \frac{\int EQE_{Post}(\lambda)\phi(\lambda)d\lambda}{\int EQE_{Pre}(\lambda)\phi(\lambda)d\lambda} \qquad 4.5.$$

One potential reason for this discrepancy is the difference between measurement technique. When taking the EQE spectra, a low intensity, monochromated beam of light is focused onto a small spot size on the

cell, whereas when the light IV measurement is conducted, the illumination source is calibrated to be as intense as AM0 illumination and the entire area of the cell is illuminated at once. In general, sampling smaller areas of an OHLP cell usually yields a higher photocurrent than sampling larger areas of a cell, and is one of the reasons why scaleup presents a challenge [100] [101]. Charge transport in an OHLP device is very vertical in nature, with grain boundaries providing sites for recombination and loss of current. Sampling larger areas also offers more pathways for shorts to occur [100]. As such, one potential reason for this discrepancy could be due to how data is collected. However, in the literature, usually this sort of discrepancy is small and does not match up with the large differences between J_{sc} and EQE we observe.

Considering more material-intrinsic reasons for this discrepancy, one popular hypothesis is that this sort of discrepancy arises due to the ion migration phenomenon that occurs in OHLP cells. It has been suggested that when J_{sc} is observed to be higher than EQE, it is because EQE measurements take considerable amounts of time- usually 5 to 30 minutes, while light IV sweeps often take less than a minute. A longer light exposure duration means the film has more time for photodegradation to occur, and in OHLP films, this manifests in the form of mobile defects like halide vacancies that migrate to the OHLP's interfaces [99]. In our films, we note the opposite trend between J_{sc} and EQE. This suggests to us that ion migration mechanics may be different in protonated OHLP films. Suppose the formation and migration of mobile ion vacancies occurs on much faster timescales, on the order of seconds as opposed to minutes. It then makes sense for OHLP photodegradation to not be influenced by exposure time, but rather, exposure intensity, giving rise to a higher EQE than J_{sc}. The hypothesis here is thus that the presence of protons in the bulk catalyses the ion migration kinetics present in OHLP devices. Theoretically, interstitial hydrogen has been predicted to diffuse quickly through the lattice, offering pathways for this hypothesized catalysis of ion migration [102] [103].

Building on the idea that photodegradation of protonated OHLPs is intensity-dependant, we once again turn to our experimental setup. As mentioned earlier, when taking light IV, the cell is subject to AM0 levels of illumination intensity, while in an EQE measurement, the light source is monochromated, chopped up, passed through an aperture and focused to a small spot. Empirically a cell is subject to much higher levels of illumination intensity in the light IV measurement than in an EQE measurement. With that in mind let us consider how intensity is known to photodegrade OHLP cells. So far, most of the literature agrees that recoverable photodegradation is due to metastable deep trap polaron states arising from electron-ion interaction within the lattice [104] [105]. However, this metastability arises on the order of hours and dissipates on the order of minutes. Once again, it appears that if a similar metastability is giving rise to recoverable, intensity-dependant photodegradation, it must be catalysed by the presence of protons in the bulk.

So far, we have developed a rather strong understanding of the proton degradation of OHLP cells. With this experiment as well as our previous experiment, we have established that amongst the 5 films in our cell, the OHLP absorber film is indeed responsible for majority of the degradation. This degradation occurs due to the presence of protons in the bulk, as opposed to protons that pass through the film. We believe that the protons present in the bulk catalyse intensity-dependant photodegradation of OHLP. We have thus far seen that low energy, high fluence proton irradiation has elucidated meaningful results regarding how an OHLP cells degrades the most. We will wrap up this study in the next section where we attempt to perform anneal recovery on our cells, which shall fill in the final pieces of the puzzle.

4.5 Anneal Recovery of Irradiated Perovskite Cells

Having successfully characterized how OHLP cells degrade under proton irradiation, we now seek to characterize how they recover this damage. Anneal recovery of proton-degraded OHLP cells has been demonstrated in the literature before [56]. However, most studies only concern themselves with demonstrating recovery. As such we are motivated to characterize this recovery by monitoring the amounts of recovery experienced at different temperatures.

Our experimental setup is as such. We place our cells in a vacuum chamber that has a pin stage loaded inside to allow us to make electrician contact to our cells via a Keithley voltammeter. This pin stage is also wired up to a resistive heating element and a resistance temperature detector (RTD). The heating element is connected to an external power source; and that power source and the RTD are connected to a proportional-integral-differential (PID) temperature controller. Furthermore, our ABET solar simulator is once again outfitted with an AM0 filter and calibrated to AM0 intensity with a Spectrolab XTJ isotopes CIC-GaAs reference cell. The solar simulator's shutter, the Keithley and the PID controller all communicate with a computer via a Python script, allowing us to anneal the sample at desired temperatures in the dark while doing periodic light IV measurements to track their recovery. Figure 4.12. (a) shows the schematic of our setup.

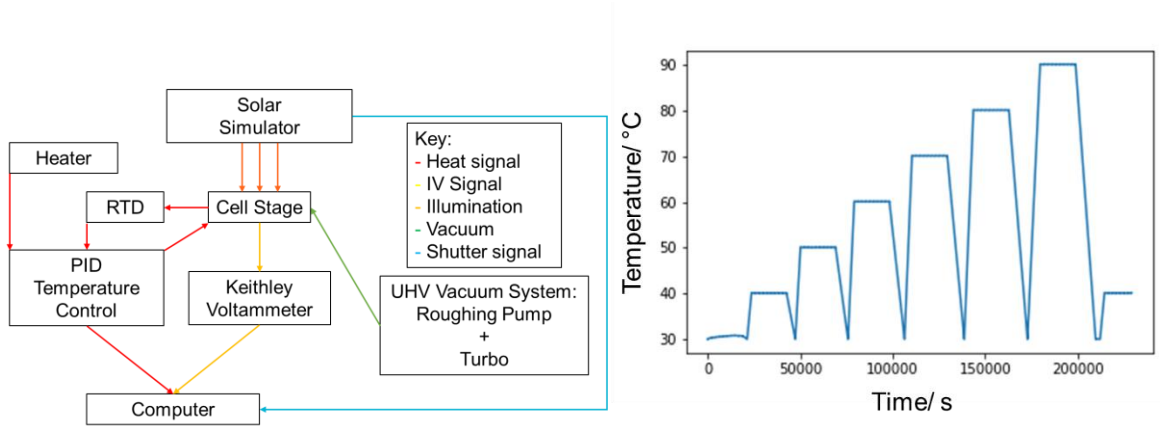

(a) (b)

Figure 4.12. Setup of anneal recovery of OHLPs. (a) Schematic showing the instruments used to characterize anneal recovery in proton-degraded OHLP cells and (b) the anneal profile this setup was used to subject cells to.

Using this setup, the experiment was conducted: proton-degraded OHLP cells were annealed in vacuum in the dark at different temperatures for 6h each temperature. The temperatures used in this experiment were 30°C, 40°C, 50°C, 60°C, 70°C, 80°C and 90°C. During each 6h anneal step, every 30 minutes, the shutter to the solar simulator was opened and light IV measurements of select, high-performance cells were recorded from -0.02V to 1.2V in both forward and reverse sweeps. Once the IV data were recorded the shutter was closed. Once each 6h anneal step was done, the cells were cooled to 30°C to ensure each anneal step began at the same base temperature. Once the cells cooled to that temperature, the shutter was opened again and additional light IV sweeps were conducted. Figure 4.12. (b) plots the temperature profile the cells were subject to in this experiment. We plot the time-evolved IV trends of the proton-degraded cells in Figure 4.12., plotting V_{oc}, J_{sc} and PCE against time.

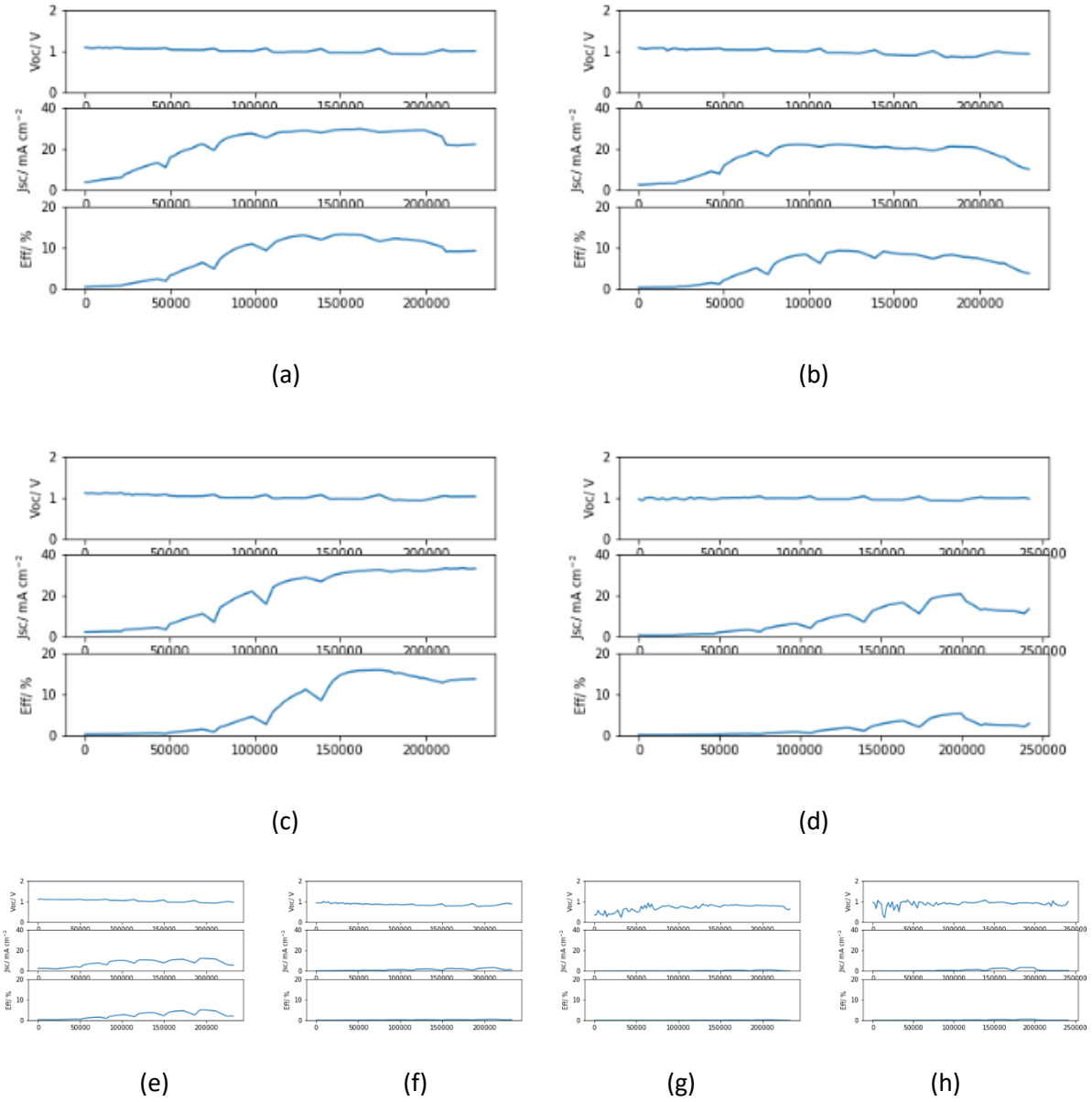

Figure 4.13. Anneal recovery profiles for cells irradiated by 30keV protons to fluences of (a) 4.3 x 10^{13} p^+cm^{-2}, (b) 8.6 x 10^{13} p^+cm^{-2}, (c) 1.4 x 10^{14} p^+cm^{-2}, and (d) 1.7 x 10^{14} p^+cm^{-2}, and cells irradiate by 75keV protons to fluences of (e) 4.3 x 10^{13} p^+cm^{-2}, (f) 8.6 x 10^{13} p^+cm^{-2}, (g) 1.4 x 10^{14} p^+cm^{-2}, and (h) 1.7 x 10^{14} p^+cm^{-2}.

Before we can begin analysing the recovery data in the context of OHLP proton degradation, there is an important parameter we must convince ourselves of: that we have been able to demonstrate temperature recovery. In an anneal experiment, two factors are at play: anneal temperature and anneal duration. We must be certain that in our experiment, we have been successful in deconvoluting the cumulative recovery from anneal time from the temperature dependence we seek to display. Experimentally, we have done our best to ensure each anneal step is deconvoluted form the last by cooling the sample down to 30°C so that every anneal step begins at the same temperature. Empirically, there is an easy way to conclude that

OHLP cell recovery is indeed temperature dependant, and that is by considering the rate of recovery. Indeed, if a cell recovers performance faster at higher temperatures, then is follows trivially that there is indeed temperature dependence. Looking to the PCE vs time trends at the bottom subplot in each figure in Figure 4.13., we see this is true. Explaining these plots a bit, every time there is a dip in the line, it signifies that the current 6h anneal step is done and the temperature has dropped back to 30°C. Reviewing the continuous lines between these dips, we not that the slope slowly increases in gradient until a critical gradient, then the gradient reduces. In other words, as temperature increases, the rate of recovery of the cells increases until the cell fully recovers. If there was no temperature-dependant recovery, the gradient would be constant throughout. However, we note that the temperature at which the gradient stops increasing is different from plot to plot. Specifically, in the case of the cells damaged by 30keV protons in Figure 4.13. (a)-(d), the higher the fluence, the higher the temperature at which maximum recovery occurs. Cell recovery is temperature dependant, but also damage dependant.

With that conviction, we now examine how different anneal temperatures has impacted OHLP anneal recovery. As mentioned earlier, recovery drops off at higher temperatures for cells subject to higher fluences of protons. In order to get a better picture of this, we turn to Figure 4.14., where we plot the light IV curves of each cell recorded at 30°C after each 6h anneal step. For reference we also include the light IV curves before and after the radiation experiment in the previous section. In addition, we have included the same anneal data for our control sample that was not irradiated. Specifically, observing the unirradiated sample, we note that a normal, undegraded OHLP sample drops in V_{oc} and FF as temperature increases. For the samples subject to 30keV, while the cell is recovering, we note that Jsc and FF increase with temperature. Once recovery is complete, the cells exhibit behaviour similar to the unirradiated samples, with the Voc and FF decreasing as temperature increases from 70°C to 90°C. This reinforces our earlier observation that anneal recovery is good up to a point. Specifically, one may conclude here that once recovery is complete, the irradiated cell behaves as a normal cell. If the damage to OHLP devices is due to the presence of protons as suggested in section 4.4, then it is clear that these protons are being annealed out of the device.

The recovery trends seen in the IV plots also corroborates with the IV-time recovery plots. For 30keV, 4.3 x 10^{13} $p^{+}cm^{-2}$, full recovery happens at 60°C to 70°C. For 8.6 x 10^{13} $p^{+}cm^{-2}$, full recovery happens at 70°C. This full recovery temperature then increases to 80°C at 1.4 x 10^{14} $p^{+}cm^{-2}$, and finally the full recovery temperature is 90°C at 1.7 x 10^{14} $p^{+}cm^{-2}$. Once again, the higher the fluence, the more damage was dealt to it, and a higher temperature and more anneal time is required to anneal bulk protons out of the device.

Throughout this discussion we have focused on the trends presented to us by the 30keV samples as they have yielded very clear trends and reasonable recovery to comment on. We however have not addressed the data from the cells subject to 75keV proton irradiation. This is because, as can be seen from the plots in both Figures 4.13. (e) to (f) and Figures 4.14. (e) to (f), there is very little recovery. There is a discrepancy here. Taking into account the radiation damage trends from Chapter 4.4, we note from that experiment that while 75keV resulted in more damage than 30keV, they were on the similar order of magnitude. However, in this recovery experiment, the recovery exhibited by cells damaged by 75keV protons are mere fraction of those from cells damaged by 30keV protons. It is clear that there is extra damage incurred by subjecting a cell to 75keV protons that cannot be easily annealed out.

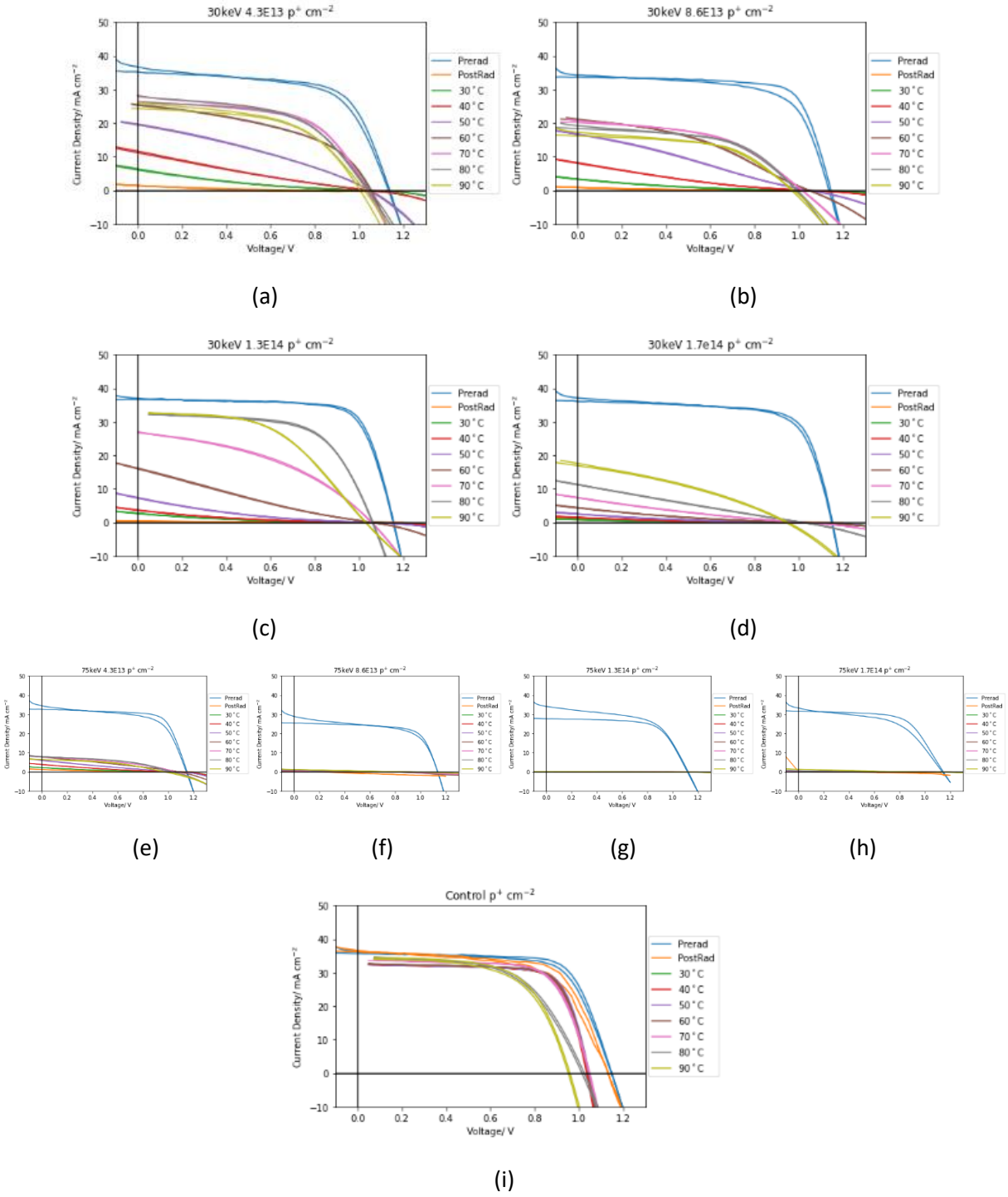

Figure 4.14. IV-curves tracking anneal recovery profiles for cells irradiated by 30keV protons to fluences of (a) 4.3 x 10^{13} p^+cm^{-2}, (b) 8.6 x 10^{13} p^+cm^{-2}, (c) 1.4 x 10^{14} p^+cm^{-2}, and (d) 1.7 x 10^{14} p^+cm^{-2}, cells irradiate by 75keV protons to fluences of (e) 4.3 x 10^{13} p^+cm^{-2}, (f) 8.6 x 10^{13} p^+cm^{-2}, (g) 1.4 x 10^{14} p^+cm^{-2}, and (h) 1.7 x 10^{14} p^+cm^{-2}, and (i) the control cell.

One can trace a possible reason for this damage by reviewing all the data we have so far. Consider the SRIM calculations in Figure 4.2. There we note that 75keV protons get deposited at the OHLP/HTL interface in much greater quantities than 30keV protons. Trusting our conclusions from sections 4.3 and 4.4, we know that protons deposited in the HTL and TCL themselves should not be responsible for this severe degradation. By the process of elimination, then, it is clear that when protons are deposited near the OHLP/HTL interface, is causes dagame to the device that cannot be easily annealed out. This is reinforced by the 30keV simulations that still show trace protons being deposited near the OHLP/HTL. We note that just like the 75keV samples, the 30keV samples also exhibited some amount of unrecovered damage, and this unrecoverable damage increased with fluence, meaning the more protons that are deposited at the OHLP/HTL interface, the ore irrecoverable damage happens. This has big implications for OHLP cell design for SSPP. It means that no matter how much radiation shielding is employed, and no matter how much anneal recovery is planned into the operating life cycle, the most crucial factor is to ensure protons do not get deposited at the OHLP/HTL interface.

4.6. Radiation Testing of Flexible Perovskites

So far we have reported some very exciting scientific results, but not all of our experiments yielded clean trends, some owing to poor signal quality. In this section, we report the proton irradiation of OHLP cells fabricated on flexible substrates. Although the outcome of this testing leaves something to be desired, this data is still very important to report as our end goal is to develop radiation resistant, lightweight, flexible OHLP devices for unencapsulated flat panel SBSP. As such this experiment represents radiation testing of potential cells that might actually see deployment in SBSP.

OHLP cells fabricated on ultralight flexible substrates were provided from a collaborator from the Kaltenbrunner group in Johannes Kepler University. For stability, these cells are mounted on an acrylic plastic frame that lines the outside of the film. These cells on principle are able to achieve the desired high specific power if they are above 15% PCE, and in fact, the group has in fact demonstrated a specific power of 23W g^{-1} in previous works [25]. We focused primarily on before-and-after IV characterisation, measuring them in a similar fashion to previous cells in this work, and also subjecting to similar energies and doses of radiation, with 4 samples were subject to 30keV protons to fluences of 4.3×10^{13} p^+ cm^{-2}, 8.6×10^{13} p^+ cm^{-2}, 1.3×10^{14} p^+ cm^{-2} and 1.7×10^{14} p^+ cm^{-2}, respectively. Figure 4.15. summarizes the before-and-after IV curves. For this experiment, as signal was difficult to acquire both before and after irradiation, we decided to report all cells no matter how poorly they turned out for illustrative purposes, plotting in each sub figure the light IV curves of all cells subject to a single fluence.

We note however that the cells as measured before irradiation were very low efficiency, and that post irradiation the cells did not yield any meaningful light IV response. More importantly, unlike the Cealux cells, the JKU control cell degraded as much as the other irradiated cells. Handling these cells can be very difficult, and a lot of degradation probably already happened just by transporting them from JKU to our laboratories and from ours to BREL where the testing happened. Further transport and proton damage seems to have killed any remnant performance. As a post-mortem, beyond improving transport methodology, it seems scientifically ideal for the cells to be fabricated, mounted onto their frames, and irradiated in the same location, regardless of logistical feasibility.

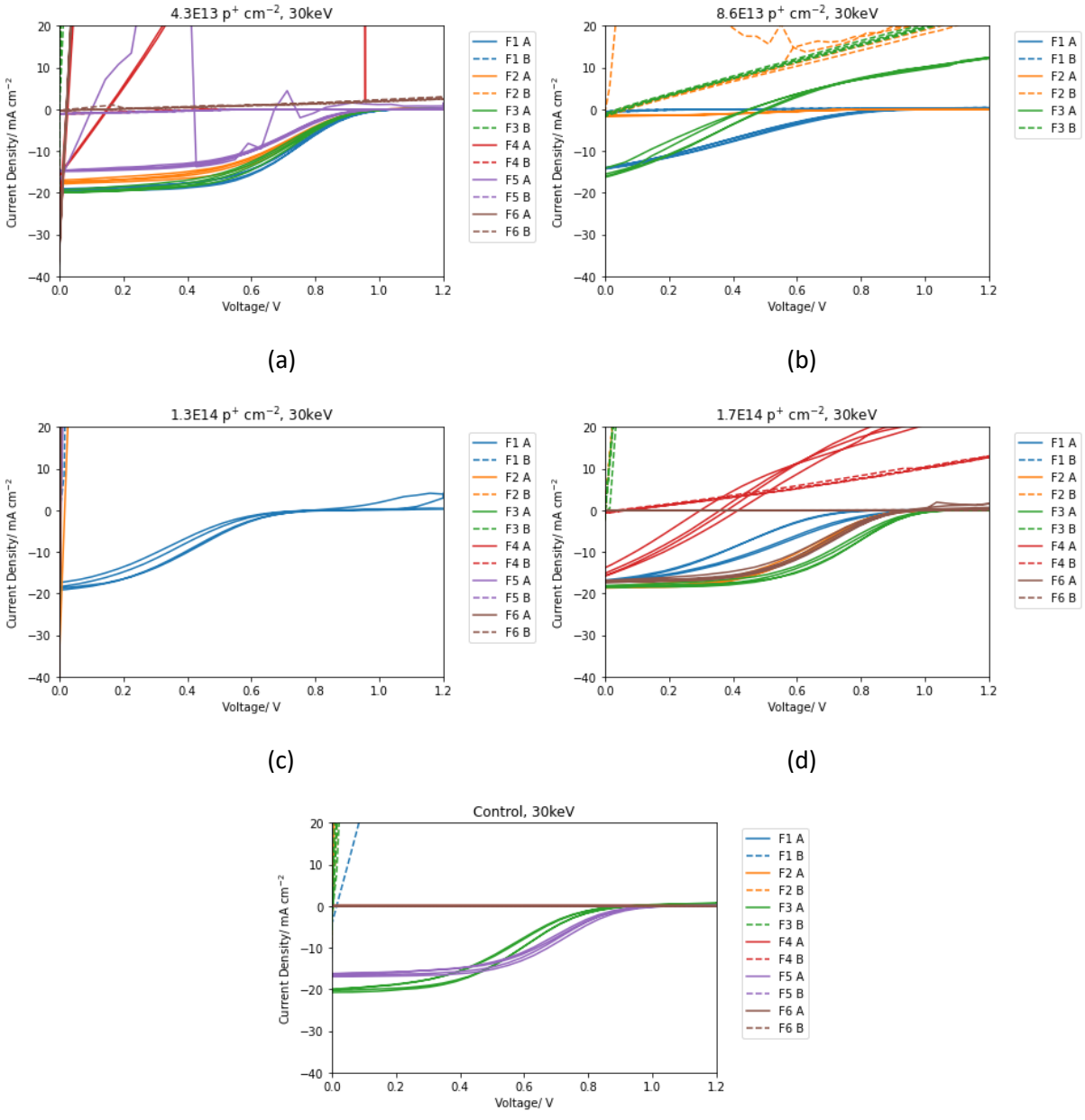

Figure 4.15. Light IV measurements of cells before and after irradiation of 30keV protons, subject to fluences of (a) 4.3 x 10^{13} p^+cm^{-2}, (b) 8.6 x 10^{13} p^+cm^{-2}, (c) 1.4 x 10^{14} p^+cm^{-2}, (d) 1.7 x 10^{14} p^+cm^{-2} and (e) the control sample; in the legend, an 'A' indicated the measurement was before radiation and a 'B' indicates that it was after radiation.

4.7. Conclusion

The effect of low energy, high fluence proton irradiation on OHLP cells was investigated. Common ETLs, HTLs, TCLs as well as the OHLP cells themselves were subject to > 10^{13} p^+cm^{-2} of 30keV and 75keV protons. We predict through some simple device physics models that the resistivity damages and optical transmission damages resulting from this radiation on common ETLs, HTLs and TCLs cause 1-5%

degradation of cells PCE, with PEDOT being the material that degrades the most, owing to optical darkening of the film. However, this is a mere fraction of the full cell deterioration that happens under this sort of irradiation. Instead, it is the bulk where most of the damage occurs.

We then scrutinized the differences between our J_{sc} and EQE measurement, as these two parameters should be equal. Contrasting our trends against literature trends, we considered ways in which photodegradation happens in cells, and came to the conclusion that the presence of protons enhances intensity-dependant photodegradation.

Finally, we annealed our samples at different temperatures and found two things. First, annealing appears to remove the protons deposited in the films, and more protons require more time and temperature to be annealed out. Once all the protons are removed, the cells behave as a normal cell would. Second, irrecoverable damage is incurred when protons are deposited near the OHLP/ETL interface.

Through this study, a good grasp of how an OHLP device degrades under proton irradiation. Instead of establishing radiation hardness and anneal recovery under a simulated ten year life cycle, we have instead identified degradation and recovery trends that allow us to have a stronger understanding of how to design OHLP cells for flat panel SBSP.

5. Photovoltaic Technologies developed for Space-Based Solar Power

5.1. Space-Based Solar Power

In this chapter, we summarize the work done in the field of photovoltaic technologies for SBSP. Three general efforts were made to advance two different forms of SBSP. In Chapter 1, we established that SBSP can overcome many key limitations behind terrestrial solar power and is a valuable asset in the pursuit of renewable energy. By harvesting energy in outer space, we find ourselves with more intense sunlight, and are at the liberty to harvest energy even at night, allowing for electricity to be harvested around the clock, and more importantly, when electricity is used the most. We identified that the mass per unit area of solar cells and power generated per unit mass were key metrics in a field where launch mass is a key driving factor and established that there was much room for improvement from the current III-V and silicon-based technologies simply because those photovoltaic technologies required heavy radiation shielding.

We then introduced two avenues to achieve lighter areal density and higher specific power. The first was to employ optical concentrators to reduce the floorspace occupied by solar cells and their heavy shielding. We introduced our parabolic concentrator array which could achieve specific powers as high as 4.1 Wg^{-1}. We also considered the possibility of unshielded ultralight flat panel photovoltaics using materials that were radiatively hard and after a quick calculation established that 10 Wg^{-1} could easily be achieved. With these two core branches of SBSP established, we began reporting work done on each front.

5.2. Radiative Cooling of Space-Based Solar Power Structures

Having introduced CPV, we quickly identified that heat management would be an issue. Beyond developing a way to conduct heat away from the cell, who would easily see as much as 10 to 20x the intensity of the Sun, it was important to transfer heat out of the body. We considered tailored IR emissive surfaces for both the frontside and backside in order to maintain a reasonable 50-80°C working temperature range. The backside was allowed to be highly emissive, as high as 0.8 across the mIR range from 2µm to 30µm, as the restriction was on the frontside emitter, which in our structure needed to simultaneously be very reflective in the visible. In essence the frontside thermal coating had to be capable of daytime radiative cooling. We established that the frontside had to be at least 0.5 emissive across the mIR regime to achieve our working temperature range.

With these parameters established we set about designing ultralight thermal coatings that could achieve these conditions. In order to maintain ultralight areal densities and also make it easy to coat centimetre scale surfaces easily, we selected the Salisbury screen as our primary architecture, a coating that was know to be lightweight and highly absorptive and emissive. Using the RCWA method, we optimised a backside single-layer coating using 2nm Cr/ 2µm CP1/ 500nm Ag that had an mIR emissivity of 0.6. Adding a second layer of this coating, we predicted that a 0.5nm Cr/ 1.9µm CP1/ 3nm Cr/ 2µm CP1/ 500nm Ag screen could achieve an emissivity of 0.8. We also optimised a 10nm ITO/ 2 µm CP1/ 500nm Ag frontside emitter which had a visible reflectivity of 0.896 and a mIR emissivity of 0.554, well within the restriction set out by the earlier thermal simulations.

Looking towards our RCWA simulations, we established that Cr and ITO were very important material choices for our devices as they were lossy enough in the mIR to allow for enough destructive interference, and ITO was above that transparent in the visible. Looking toward the $|E|^2$ field profiles through these coatings at different wavelengths, we found out that the emissive modes occur at anti-resonant profiles, and that was why our destructive interference was so broadband.

We then fabricated these structures, measured them, and found them to meet the specifications required. We thus report, as the first part of our thesis, two types of optical coatings developed for the radiative cooling of SBSP.

5.3. Fabrication and Characterisation of Perovskite Solar Cells

OHLP were introduced as a potential family of materials for unshielded flat panel SBSP. Their advantages, such as high performance, tuneability and ease of fabrication were introduced, and personal work done on fabrication was reported. Work done on two different chemistries of OHLPs were reported, and their recipes were iterated upon using empirical observations combined with knowledge gleaned from the literature. Through this work, the challenges intrinsic to OHLP solar cell fabrication were elucidated.

Iterating through $MAPbI_3$, based perovskites, we found that dopants were useful in increasing PCBM's mobility in order to remove the S-kink, and that gentle contact deposition was important to avoid damaging the OHLP layer. Doing both increased FF and J_{sc}, respectively, yielding an in-house record PCE of 12.41%. Iterating through $FA_{1-x}Cs_xPbI_3$ recipes, we found that not all OHLP surfaces are the same and that the surfactant CTAB worked better on more OHLP formulations with more organic species and less Cs content. We also found FA:Cs ratios of 85:15 to work best for us. Varying the PCBM deposition technique, we found it better when PCBM was allowed to spread over the surface of the OHLP slowly before spincoating, as opposed to being dripped down. An in-house record PCE of 11.81% was achieved. SEM and PL were attempted, however owing to inconsistent film quality, little useful conclusions could be drawn from these studies.

From this study, as well as anecdotal conversations with the community, we found that the biggest hurdles to effective OHLP solar cell fabrication lay in careful technique and observation of chamber conditions that should be more exhaustively documented in future works.

5.4. Proton Irradiation of Perovskite Solar Cells

Finally, we irradiated OHLP solar cells with 30keV and 75keV protons at high fluences of up to 1.7×10^{14} p^+cm^{-2}. These energies and fluences were chosen to cause maximum damage to the cells, allowing us to observe better degradation trends and recovery behaviour, giving us a deeper understanding of how to design OHLP solar cells for unencapsulated flat panel SBSP. In addition, the individual ETL, HTL and TCLs were also irradiated to help us deconvolute the effects of proton irradiation on the other materials present in OHLP solar cells.

Proton irradiation was observed to degrade the electrical resistivity and optical transmissivity of ITO, PEDOT, NiO_x, PCBM and PTCD-I to varying degrees. However, by carefully accounting for how these parameters affect the final efficiency of the cell, we concluded that the increase in resistance and opaqueness do not decrease cell efficiency by more than 5%. Compared to the degradation we would observe in the solar cells, this degradation is negligible.

Observing the light IV and EQE trends, we noted that cells subject to this level of radiation degraded catastrophically. Contrasting this level of degradation against the individual transport layers earlier, we concluded that majority of the degradation occurs due to deposition of protons within the bulk of the OHLP absorber layer. Scrutinizing the light IV and EQE trends, we noticed that the J_{sc} and EQE values should correspond to each other, yet they deviated greatly. Considering reasons why this might be, we came to the conclusion that no matter what the mechanism, it was evident that the presence of protons within the OHLP absorber layer was accelerating metastable intensity-dependant photodegradation.

Through our anneal recovery study, we were able to ascertain that anneal recovery of cell performance is indeed temperature-dependant. By considering how 75keV protons caused much more irrecoverable damage than 30keV protons and contrasting this data against our earlier SRIM predictions about proton penetration profiles, we concluded that irrecoverable damage must be happening when protons strike the OHLP-NiO_x interface.

Through this study, we found that the most damaging proton radiation is the type that gets deposited in the OHLP absorber layer, and also the type that impinges on the OHLP-HTL interface. When designing unencapsulated SBSP, the most important factor should be to consider how much fluence of protons get deposited in these areas over its lifetime.

5.5 Outlook

Truly interesting and novel findings have been uncovered through this study. Looking ahead, it is clear that flat panel, unencapsulated SBSP is the way to go to achieve high specific powers that make SBSP launch costs. However, much progress still needs to be made to achieve that reality. High efficiency flexible substrate OHLP solar cells capable of withstanding some amount of ruggedness during transport still needs to be achieved and irradiated to ascertain their compatibility with space environments. On top of that, while radiative cooling schemes were developed for CPV structures, they were not developed nor considered so far for flat panel SBSP. Given that we do not have a mirror coating for sun-facing cooling, another method from frontside cooling must be considered.

References

[1] "World Power Consumption," Enerdata, 2021. [Online]. Available: https://yearbook.enerdata.net/electricity/electricity-domestic-consumption-data.html.

[2] "Frequently Asked Questions," U.S. Energy Information Administration, 2021. [Online]. Available: https://www.eia.gov/tools/faqs/faq.php?id=427&t=3.

[3] "Basics of Climate Change," US EPA, [Online]. Available: https://www.epa.gov/climatechange-science/basics-climate-change.

[4] "In Depth | Sun," NASA Solar System Exploration, [Online]. Available: https://solarsystem.nasa.gov/solar-system/sun/in-depth/.

[5] American Society for Testing and Materials Technology. Committee E21 on Space Simulation and Applications of Space, "Standard solar constant and zero air mass solar spectral irradiance tables.," *ASTM International,* 2000.

[6] "The Sky's theLimit: Solar and Wind energy potential," Carbon Tracker Initiative, 23 April 2021. [Online]. Available: https://carbontracker.org/reports/the-skys-the-limit-solar-wind/.

[7] American Society for Testing and Materials G-173-03, "Standard Tables for Reference Solar Spectral Irradiances: Direct Normal and Hemispherical on 37° Tilted Surface," 2020.

[8] S. Comello, S. Reichelstein and A. Sahoo, "The road ahead for solar PV power," *Renewable and Sustainable Energy Reviews,* vol. 92, pp. 744-756, 2018.

[9] P. Glaser, "Power from the Sun: Its Future," *Science,* vol. 162, no. 3856, pp. 857 - 861, 1968.

[10] L. S. Belyaev, O. V. Marchenko, S. P. Filippov and S. V. Solomin, "Studies on competitiveness of space and terrestrial solar power plants using global energy model," *International Journal of Global Energy Issues,* vol. 1, no. 2, pp. 94-108, 2006.

[11] R. Jones, "Alternative Orbits: A New Space Solar Power Reference Design," *Online Journal of Space Communication,* vol. 9, no. 16, p. 14, 2021.

[12] H. Jones, "The recent large reduction in space launch cost.," in *48th International Conference on Environmental Systems*, 2018.

[13] E. Gdoutos, C. Leclerc, F. Royer, M. D. Kelzenberg, E. C. Warmann, P. Espinet-Gonzalez, N. Vaidya, F. Bohn, B. Abiri, M. R. Hashemi, M. Gal-Katziri, A. Fikes, H. A. Atwater, A. Hajimiri and S. Pellegrino, "A lightweight tile structure integrating photovoltaic conversion and RF power transfer for space solar power applications," in *AIAA Spacecraft Structures Conference*, 2018.

[14] P. Jaffe, J. Hodkin, F. Harrington, C. Person, M. Nurnberger, B. Nguyen, S. LaCava, D. Scheiman, G. Stewart, A. Han, E. Hettwer and D. Rhoades, "Sandwich module prototype progress for space solar power," *Acta Astronautica,* vol. 94, no. 2, pp. 662-671, 2014.

[15] K. Shimazaki, Y. Kobayashi, M. Takahashi, M. Imaizumi, M. Murashima, Y. Takahashi, H. Toyota, A. Kukita, T. Ohshima, S.-i. Sato, T. Takamoto and H. Kusawake, "First Flight Demonstration of Glass-Type Space Solar Sheet," in *IEEE 40th Photovoltaic Specialist Conference*, 2014.

[16] J. A. Carr, D. Boyd, A. Martinez, M. SanSoucie, L. Johnson, G. Laue, B. Farmer, J. C. Smith, B. Robertson and M. Johnson, "The Lightweight Integrated Solar Array and Transceiver (LISA-T): second generation advancements and the future of SmallSat power generation," in *30th Annual AIAA/USU Conference on Small Satellites*, 2016.

[17] B. E. Anspaugh, "Proton and electron damage coefficients for GaAs/Ge solar cells," in *The Conference Record of the Twenty-Second IEEE Photovoltaic Specialists Conference-1991*, 1991.

[18] J. M. Raya-Armenta, N. Bazmohammadi, J. C. Vasquez and J. M. Guerrero, "A short review of radiation-induced degradation of III–V photovoltaic cells for space applications," *Solar Energy Materials and Solar Cells,* vol. 233, p. 111379, 2021.

[19] E. C. Warmann, P. Espinet-Gonzalez, N. Vaidya, S. Loke, A. Naqavi, T. Vinogradova, M. Kelzenberg, C. Leclerc, E. Gdoutos, S. Pellegrino and H. A. Atwater, "An ultralight concentrator photovoltaic system for space solar power harvesting," *Acta Astronautica,* vol. 170, pp. 443-451, 2020.

[20] F. M. Apra, S. Smit, R. Sterling and T. Loureiro, "Overview of the Enablers and Barriers for a Wider Deployment of CSP Tower Technology in Europe," *Clean Technologies,* vol. 3, no. 2, pp. 377-394, 2021.

[21] C. Algora, E. Ortiz, I. Rey-Stolle, V. Diaz, R. Pena, V. M. Andreev, V. P. Khvostikov and V. D. Rumyanstev, "A GaAs Solar Cell with an Efficiency of 26.2% at 1000 Suns and 25.0% at 2000 Suns," *IEEE Transactions on Electron Devices,* vol. 48, no. 5, pp. 840-844, 2001.

[22] L. C. Hirst, M. K. Yakes, J. H. Warner, M. F. Bennett, K. J. Schmieder, R. J. Walters and P. P. Jenkins, "Intrinsic radiation tolerance of ultra-thin GaAs solar cells," *Applied Physics Letters,* vol. 109, no. 3, p. 033908, 2016.

[23] P. Espinet-Gonzalez, E. Barrigon, G. Otnes, G. Vescovi, C. Mann, R. M. France, A. J. Welch, M. S. Hunt, D. Walker, M. D. Kelzenberg, I. Aberg, M. T. Borgstrom, L. Samuelson and H. A. Atwater, "Radiation Tolerant Nanowire Array Solar Cells," *ACS Nano,* vol. 13, no. 11, pp. 12860-12869, 2019.

[24] Y. Miyazawa, M. Ikegami, T. Miyasaka, T. Ohshima, M. Imaizumi and K. Hirose, "Evaluation of radiation tolerance of perovskite solar cell for use in space," in *2015*, 2015 IEEE 42nd Photovoltaic Specialist Conference.

[25] M. Kaltenbrunner, G. Adam, E. D. Glowacki, M. Drack, R. Schwodiauer, L. Leonat, G. H. Apaydin, H. Groiss, M. C. Scharber, M. S. White, N. S. Sariciftci and S. Bauer, "Flexible high power-per-

weight perovskite solar cells with chromium oxide–metal contacts for improved stability in air," *Nature Materials,* vol. 14, no. 10, pp. 1032-1039, 2015.

[26] K. Nishioka, T. Sueto, M. Uchida and Y. Ota, "Detailed analysis of temperature characteristics of an InGaP/InGaAs/Ge triple-junction solar cell," *Journal of Electronic Materials,* vol. 39, no. 6, pp. 704-708, 2010.

[27] P. Espinet-Gonzalez, C. Algora, N. Nunez, V. Orlando, M. Vazquez, J. Bautista and K. Araki, "Temperature accelerated life test on commercial concentrator III–V triple-junction solar cells and reliability analysis as a function of the operating temperature," *Progress in Photovoltaics: Research and Applications,* vol. 23, no. 5, pp. 559-569, 2015.

[28] A. Shang and X. Li, "Photovoltaic Devices: Opto-Electro-Thermal Physics and Modeling," *Advance Materials,* vol. 29, no. 8, p. 1603492, 2017.

[29] A. Naqavi, S. P. Loke, M. D. Kelzenberg, D. M. Callahan, T. Tiwald, E. C. Warmann, P. Espinet-Gonzalez, N. Vaidya, T. A. Roy, J.-S. Huang, T. G. Vinogradova and H. A. Atwater, "Extremely broadband ultralight thermally-emissive optical coatings," *Optics Express,* vol. 26, no. 14, pp. 18545-18562, 2018.

[30] W. W. Salisbury, "Absorbent body for electromagnetic waves". U.S. Patent 2,599,944, 10 June 1952.

[31] H. Kocer, S. Butun, Z. Li and K. Aydin, "Reduced near-infrared absorption using ultra-thin lossy metals in Fabry-Perot cavities," *Scientific reports,* vol. 5, no. 1, pp. 1-6, 2015.

[32] E. Rephaeli, A. Raman and S. Fan, "Ultrabroadband photonic structures to achieve high-performance daytime radiative cooling," *Nano letters,* vol. 13, no. 4, pp. 1457-1461, 2013.

[33] J.-L. Kou, Z. Jurado, Z. Chen, S. Fan and A. J. Minnich, "Daytime radiative cooling using near-black infrared emitters," *Acs Photonics,* vol. 4, no. 3, pp. 626-630, 2017.

[34] K. Mizuno, J. Ishii, H. Kishida, Y. Hayamizu, S. Yasuda, D. N. Futaba, M. Yumura and K. Hata, "A black body absorber from vertically aligned single-walled carbon nanotubes," *Proceedings of the National Academy of Sciences,* vol. 106, no. 15, pp. 6044-6047, 2009.

[35] A. D. Rakic, A. B. Djurisic, J. M. Elazar and M. L. Majewski, "Optical properties of metallic films for vertical-cavity optoelectronic devices," *Applied Optics,* vol. 37, no. 22, pp. 5271-5283, 1998.

[36] A. D. Rakic, "Algorithm for the determination of intrinsic optical constants of metal films: application to aluminum," *Applied Optics,* vol. 34, no. 22, p. 475504767, 1995.

[37] H. U. Yang, J. D'Archangel, M. L. Sundheimer, E. Tucker, G. D. Boremann and M. B. Raschke, "Optical dielectric function of silver," *Physical Review B,* vol. 91, no. 23, p. 235137, 2015.

[38] R. L. Olmon, B. Slovick, T. W. Johnson, D. Shelton, S.-H. Oh, G. D. Boremann and M. B. Raschke, "Optical dielectric function of gold," *Physical Review B,* vol. 86, no. 23, p. 235147, 2012.

[39] A. K. St Clair and T. L. St Claire, “Process for preparing essentially colorless polyimide film containing phenoxy-linked diamines”. U.S. Patent 4,595,548, 17 June 1986.

[40] J. P. Hugonin and P. Lalanne, “Reticolo software for grating analysis,” Institut d'Optique, Orsay, France, 2005.

[41] L. K. Ono, E. J. Juarez-Perez and Y. Qi, “Progress on perovskite materials and solar cells with mixed cations and halide anions,” *ACS applied materials & interfaces,* vol. 9, no. 36, pp. 30197-30246, 2017.

[42] E. Vega, M. Mollar and B. Mari, “Bandgap tuning of MAPbI3−XBrx thin film perovskites for photovoltaic applications,” in *2015 3rd International Renewable and Sustainable Energy Conference*, 2015.

[43] H. Min, M. Kim, S.-U. Lee, H. Kim, G. Kim, K. Choi, J. H. Lee and S. I. Seok, “Efficient, stable solar cells by using inherent bandgap of α-phase formamidinium lead iodide,” *Science,* vol. 366, no. 6466, pp. 749-753, 2019.

[44] S. Xu, A. Libanori, G. Luo and J. Chen, “Engineering bandgap of CsPbI3 over 1.7 eV with enhanced stability and transport properties,” *Iscience,* vol. 24, no. 3, p. 102235, 2021.

[45] W. Shockley and H. J. Queisser, “Detailed Balance Limit of Efficiency of pn Junction Solar Cells,” *Journal of Applied Physics,* vol. 32, no. 3, pp. 510-519, 1961.

[46] T. Wang, B. Daiber, J. M. Frost, S. A. Mann, E. C. Garnett, A. Walsh and B. Ehrler, “Indirect to direct bandgap transition in methylammonium lead halide perovskite,” *Energy & Environmental Science,* vol. 10, no. 2, pp. 509-515, 2017.

[47] N. K. Kumawat, A. Dey, A. Kumar, S. P. Gopinathan, K. L. Narasimhan and D. Kabra, “Band Gap Tuning of CH3NH3Pb(Br1–xClx)3 Hybrid Perovskite for Blue Electroluminescence,” *ACS applied materials & interfaces,* vol. 7, no. 24, pp. 13119-13124, 2015.

[48] C. Wehrenfennig, G. E. Eperon, M. B. Johnston, H. J. Snaith and L. M. Herz, “High charge carrier mobilities and lifetimes in organolead trihalide perovskites,” *Advanced Materials,* vol. 26, no. 10, pp. 1584-1589, 2014.

[49] S. D. Stranks, G. E. Eperon, G. Grancini, C. Menelaou, M. J. Alcocer, T. Leijtens, L. M. Herz, A. Petrozza and H. J. Snaith, “Electron-Hole Diffusion Lengths Exceeding 1 Micrometer in an Organometal Trihalide Perovskite Absorber,” *Science,* vol. 342, no. 6156, pp. 341-344, 2013.

[50] B. Chen, P. N. Rudd, S. Yang, Y. Yuan and J. Huang, “Imperfections and their passivation in halide perovskite solar cells,” *Chemical Society Reviews,* vol. 48, no. 14, pp. 3842-3867, 2019.

[51] “Best Research-Cell Efficiency Chart,” NREL, [Online]. Available: https://www.nrel.gov/pv/cell-efficiency.html. [Accessed 2022].

[52] J.-H. Im, I.-H. Jang, N. Pellet, M. Gratzel and N.-G. Park, "Growth of CH3NH3PbI3 cuboids with controlled size for high-efficiency perovskite solar cells," *Nature nanotechnology,* vol. 9, no. 11, pp. 927-932, 2014.

[53] S. Xiao, S. Xu and K. Ostrikov, "Low-temperature plasma processing for Si photovoltaics," *Materials Science and Engineering: R: Reports,* vol. 78, pp. 1-29, 2014.

[54] K. J. Scmieder, E. A. Armour, M. P. Lumb, M. K. Yakes, Z. Pulwin, J. Frantz and R. J. Walters, "Effect of growth temperature on GaAs solar cells at high MOCVD growth rates," *IEEE Journal of Photovoltaics,* vol. 7, no. 1, pp. 340-346, 2016.

[55] D. Melissa and Z. Yu, "A review of flexible halide perovskite solar cells towards scalable manufacturing and environmental sustainability," *Journal of Semiconductors,* vol. 41, no. 4, p. 041603, 2020.

[56] J.-S. Huang, M. D. Kelzenberg, P. Espinet-Gonzalez, C. Mann, D. Walker, A. Naqavi, N. Vaidya, E. Warmann and H. A. Atwater, "Effects of electron and proton radiation on perovskite solar cells for space solar power application," in *2017 IEEE 44th Photovoltaic Specialist Conference*, 2017.

[57] M. I. H. Ansari, A. Qurashi and M. K. Nazeeruddin, "Frontiers, opportunities, and challenges in perovskite solar cells: A critical review," *Journal of Photochemistry and Photobiology C: Photochemistry Reviews,* vol. 35, pp. 1-24, 2018.

[58] J. Stevenson, B. Sorenson, V. H. Subramaniam, J. Raiford, P. P. Khlyabich, Y.-L. Loo and P. Clancy, "Mayer bond order as a metric of complexation effectiveness in lead halide perovskite solutions," *Chemistry of Materials,* vol. 29, no. 6, pp. 2435-2444, 2017.

[59] A. Dualeh, P. Gao, S. I. Seok, M. K. Nazeeruddin and M. Gratzel, "Thermal behavior of methylammonium lead-trihalide perovskite photovoltaic light harvesters," *Chemostry of Materials,* vol. 26, no. 21, pp. 6160-6164, 2014.

[60] Y. Wu, X. Yang, H. Chen, K. Zhang, C. Qin, J. Liu, W. Peng, A. Islam, E. Bi, F. Ye, M. Yin, P. Zhang and L. Han, "Highly compact TiO2 layer for efficient hole-blocking in perovskite solar cells," *Applied physics express,* vol. 7, no. 5, p. 052301, 2014.

[61] J. Li, T. Bu, Y. Liu, J. Zhou, J. Shi, Z. Ku, Y. Peng, J. Zhong, Y.-B. Cheng and F. Huang, "Enhanced Crystallinity of Low-Temperature Solution-Processed SnO2 for Highly Reproducible Planar Perovskite Solar Cells," *ChemSusChem,* vol. 11, no. 17, pp. 2898-2903, 2018.

[62] S. Sajid, A. M. Elseman, H. Huang, J. Ji, S. Dou, H. Jiang, X. Liu, D. Wei, P. Cui and M. Li, "Breakthroughs in NiOx-HTMs towards stable, low-cost and efficient perovskite solar cells," *Nano Energy,* vol. 51, pp. 408-424, 2018.

[63] K. M. Reza, S. Mabrouk and Q. Qiao, "A review on tailoring PEDOT: PSS layer for improved performance of perovskite solar cells," *Proceedings of the Nature Research Society,* vol. 2, no. 1, p. 02004, 2018.

[64] C. He, F. Zhang, X. Zhao, C. Lin and M. Ye, “Interface Engineering of BCP Buffer Layers in Planar Heterojunction Perovskite Solar Cells With NiOx Hole Transporting Layers,” *Frontiers in Physics,* vol. 6, p. 99, 2018.

[65] C.-Y. Chang, W.-K. Huang, Y.-C. Chang, K.-T. Lee and C.-T. Chen, “A solution-processed n-doped fullerene cathode interfacial layer for efficient and stable large-area perovskite solar cells,” *Journal of Materials Chemistry A,* vol. 4, no. 2, pp. 640-648, 2016.

[66] X. Liu, C. Xu and E.-C. Lee, “Chlorobenzene-Mediated Control of Crystallization in Perovskite Films for High-Performance Solar Cells,” *ACS Applied Energy Materials,* vol. 3, no. 12, pp. 12291-12297, 2020.

[67] C. C. Boyd, R. Cheacharoen, K. A. Bush, R. Prasanna, T. Leijtens and M. D. McGehee, “Barrier design to prevent metal-induced degradation and improve thermal stability in perovskite solar cells,” *ACS Energy Letters,* vol. 3, no. 7, pp. 1772-1778, 2018.

[68] A. Kumar, S. Sista and Y. Yang, “Dipole induced anomalous S-shape I-V curves in polymer solar cells,” *Journal of Applied Physics,* vol. 105, no. 9, p. 094512, 2009.

[69] W. Tress, K. Leo and M. Riede, “Influence of hole-transport layers and donor materials on open-circuit voltage and shape of I–V curves of organic solar cells,” *Advanced Functional Materials,* vol. 21, no. 11, pp. 2140-2149, 2011.

[70] F. J. Garcia-Sanchez, B. Rmoero, D. C. Lugo-Munoz, G. Del Pozo, B. Arredondo, J. J. Liou and A. Ortiz-Conde, “Modelling solar cell S-shaped IV characteristics with DC lumped-parameter equivalent circuits a review,” *Facta Universitatis, Series: Electronics and Energetics,* vol. 30, no. 3, pp. 327-350, 2017.

[71] J. Seo, S. Park, Y. C. Kim, N. J. Jeon, J. H. Noh, S. C. Yoon and S. I. Seok, “Benefits of very thin PCBM and LiF layers for solution-processed p–i–n perovskite solar cells,” *Energy & Environmental Science,* vol. 7, no. 8, pp. 2642-2646, 2014.

[72] Q. Fu, X. Tang, B. Huang, T. Hu, L. Tan, L. Chen and Y. Chen, “Recent progress on the long-term stability of perovskite solar cells,” *Advance Science,* vol. 5, no. 5, p. 1700387, 2018.

[73] S. Masi, A. F. Gualdron-Reyes and I. Mora-Sero, “Stabilization of Black Perovskite Phase in FAPbI3 and CsPbI3,” *ACS Energy Letters,* vol. 5, no. 6, pp. 1974-1985, 2020.

[74] K. Schutt, P. K. Nayak, A. J. Ramadan, B. Wenger, Y. Lin and H. J. Snaith, “Overcoming zinc oxide interface instability with a methylammonium-free perovskite for high-performance solar cells,” *Advanced Functional Materials,* vol. 29, no. 47, p. 1900466, 2019.

[75] Z. Li, M. Yang, J.-S. Park, S.-H. Wei, J. J. Berry and K. Zhu, “Stabilizing perovskite structures by tuning tolerance factor: formation of formamidinium and cesium lead iodide solid-state alloys,” *Chemistry of Materials,* vol. 28, no. 1, pp. 284-292, 2016.

[76] D. Yang, R. Yang, K. Wang, C. Wu, X. Zhu, J. Feng, X. Ren, G. Fang, S. Priya and S. F. Liu, "High efficiency planar-type perovskite solar cells with negligible hysteresis using EDTA-complexed SnO2," *Nature communications,* vol. 9, no. 1, pp. 1-4, 2018.

[77] S.-H. Turren-Cruz, A. Hagfeldt and M. Saliba, "Methylammonium-free, high-performance, and stable perovskite solar cells on a planar architecture," *Science,* vol. 362, no. 6413, pp. 449-453, 2018.

[78] J. Troughton, N. Gasparini and D. Baran, "Cs 0.15 FA 0.85 PbI 3 perovskite solar cells for concentrator photovoltaic applications," *Journal of Materials Chemistry A,* vol. 6, no. 44, pp. 21913-21917, 2018.

[79] X. Ren, Z. Yang, D. Yang, X. Zhang, D. Cui, Y. Liu, Q. Wei, H. Fan and S. F. Lui, "Modulating crystal grain size and optoelectronic properties of perovskite films for solar cells by reaction temperature," *Nanoscale,* vol. 8, no. 6, pp. 3816-3822, 2016.

[80] P. Liu, W. Wang, S. Liu, H. Yang and Z. Shao, "Fundamental understanding of photocurrent hysteresis in perovskite solar cells," *Advanced Energy Materials,* vol. 9, no. 13, p. 1803017, 2019.

[81] T. Niu, J. Lu, R. Munir, J. Li, D. Barrit, X. Zhang, H. Hu, Z. Yang, A. Amassian, K. Zhao and S. F. Liu, "Stable high-performance perovskite solar cells via grain boundary passivation," *Advanced Materials,* vol. 30, no. 16, p. 1706576, 2018.

[82] R. C. MacKenzie, T. Kirchartz, G. F. Dibb and J. Nelson, "Modeling Nongeminate Recombination in P3HT:PCBM Solar Cells," *The Journal of Physical Chemistry C,* vol. 115, no. 19, pp. 9806-9813, 2011.

[83] L. Sims, U. Hormann, R. Hanfland, R. C. MacKenzie, F. R. Kogler, R. Steim, W. Brutting and P. Schilinsky, "Investigation of the s-shape caused by the hole selective layer in bulk heterojunction solar cells," *Organic Electronics,* vol. 15, no. 11, pp. 2862-2867, 2014.

[84] R. MacKenzie, V. Balderrama, S. Schmeisser, R. Stoof, S. Greedy, J. Pallares, L. Marsal, A. Chanewa and E. von Hauff, "Loss mechanisms in high efficiency polymer solar cells," *Advanced Energy Materials,* vol. 6, no. 4, p. 1501742, 2016.

[85] F. Lang, G. E. Eperon, K. Frohna, E. M. Tennyson, A. Al-Ashouri, G. Kourkafas, J. Bundesmann, A. Denker, K. G. West, L. C. Hirst, H.-C. Neitzert and S. D. Stranks, "Proton-Radiation Tolerant All-Perovskite Multijunction Solar Cells," *Advanced Energy Materials,* vol. 11, no. 41, p. 2102246, 2021.

[86] B. K. Durant, H. Afshari, S. Singh, B. Rout, G. E. Eperon and I. R. Seller, "Tolerance of Perovskite Solar Cells to Targeted Proton Irradiation and Electronic Ionization Induced Healing," *ACS Energy Letters,* vol. 6, no. 7, pp. 2362-2368, 2016.

[87] V. V. Brus, F. Lang, J. Bundesmann, S. Seidel, A. Denker, B. Rech, G. Landi, H. C. Neizert, J. Rappich and N. H. Nickel, "Defect Dynamics in Proton Irradiated CH3NH3PbI3 Perovskite Solar Cells," *Advanced Electronic Materials,* vol. 3, no. 2, p. 1600438, 2017.

[88] J. Feynman, G. Spitale, J. Wang and S. Gabriel, "Interplanetary proton fluence model," *Journal of Geophysical Research: Space Physics,* vol. 98, no. A8, pp. 13281-13294, 1993.

[89] J. Barbe, D. Hughes, Z. Wei, A. Pockett, H. K. Lee, K. C. Heasman, M. J. Carnie, T. M. Watson and W. C. Tsoi, "Radiation Hardness of Perovskite Solar Cells Based on Aluminum-Doped Zinc Oxide Electrode Under Proton Irradiation," *Solar RRL,* vol. 3, no. 12, p. 1900219, 2019.

[90] J. F. Ziegler and J. P. Biersack, "The stopping and range of ions in matter," in *Treatise on heavy-ion science*, Bostan, MA, Springer, 1985, pp. 93-129.

[91] K. Rakstys, S. Paek, P. Gao, P. Gratia, T. Marszalek, G. Grancini, K. T. Cho, K. Genevicius, V. Jankauskas, W. Pisula and M. K. Nazeeruddin, "Molecular engineering of face-on oriented dopant-free hole transporting material for perovskite solar cells with 19% PCE," *Journal of Materials Chemistry A,* vol. 5, no. 17, pp. 7811-7815, 2017.

[92] F. Smits, "Measurement of sheet resistivities with the four-point probe," *Bell System Technical Journal,* vol. 37, no. 3, pp. 711-718, 1958.

[93] Boeing, "Boeing: Radiation Effects Laboratory," Boeing, [Online]. Available: https://www.boeing.com/specialty/radiation-effects-laboratory/index.page. [Accessed 2022].

[94] X. Zheng, L. Zuo, F. Zhao, Y. Li, T. Xhen, S. Shan, K. Yan, Y. Pan, B. Xu, C.-Z. Li, M. Shi, J. Hou and H. Chen, "High-Efficiency ITO-Free Organic Photovoltaics with Superior Flexibility and Up-Scalability," *Advanced Materials,* p. 2200044, 2022.

[95] X. Lu, Y. Zhang and Z. Zheng, "Metal-Based Flexible Transparent Electrodes: Challenges and Recent Advances," *Advanced Electronic Materials,* vol. 7, no. 5, p. 2001121, 2021.

[96] M.-R. Azani, A. Hassanpour and T. Torres, "Benefits, problems, and solutions of silver nanowire transparent conductive electrodes in indium tin oxide (ITO)-free flexible solar cells," *Advanced Energy Materials,* vol. 10, no. 48, p. 2002536, 2020.

[97] W. Shockley, "The Theory of p-n Junctions in Semiconductors and p-n Junction Transistors," *Bell System Technical Journal,* vol. 28, no. 3, pp. 435-489, 1949.

[98] C. Chen, S. Zhang, S. Wu, W. Zhang, H. Zhu, Z. Xiong, Y. Zhang and W. Chen, "Effect of BCP buffer layer on eliminating charge accumulation for high performance of inverted perovskite solar cells," *RSC advances,* vol. 7, no. 57, pp. 35819-35826, 2017.

[99] M. Saliba and E. Lioz, "Current density mismatch in perovskite solar cells," *ACS Energy Letters,* vol. 5, no. 9, pp. 2886-2888, 2020.

[100] A. D. Sheikh, A. P. Patil, S. S. Mali, C. K. Hong and P. S. Patil, "New insights into active-area-dependent performance of hybrid perovskite solar cells," *Journal of Materials Science,* vol. 54, no. 15, pp. 10825-10835, 2019.

[101] W. S. Yang, B.-W. Park, E. H. Jung, N. J. Jeon, Y. C. Kim, D. U. Lee, S. S. Shin, J. Seo, E. K. Kim, J. H. Noh and S. I. Seok, "Iodide management in formamidinium-lead-halide–based perovskite layers for efficient solar cells," *Science,* vol. 356, no. 6345, pp. 1376-1379, 2017.

[102] Y. Liang, X. Cui, F. Li, C. Stampfl, S. P. Ringer and R. Zheng, "Atomic and Molecular Hydrogen Impurities in Hybrid Perovskite Solar Cells," *The Journal of Physical Chemistry C,* vol. 126, no. 4, pp. 1721-1728, 2022.

[103] D. A. Edgar, L. Kronik and A. M. Rappe, "Theory of hydrogen migration in organic–inorganic halide perovskites," *Angewandte Chemie International Edition,* vol. 54, no. 42, pp. 12437-12441, 2015.

[104] G. Nan, X. Zhang and G. Lu, "Self-healing of photocurrent degradation in perovskite solar cells: The role of defect-trapped excitons," *The Journal of Physical Chemistry Letters,* vol. 10, no. 24, pp. 7774-7780, 2019.

[105] W. Nie, J.-C. Blacon, A. J. Neukirch, K. Appavoo, H. Tsai, M. Chhowalla, M. A. Alam, M. Y. Sfeir, C. Katan, J. Even, S. Tretiak, J. J. Crochet, G. Gupta and A. Mohite, "Light-activated photocurrent degradation and self-healing in perovskite solar cells," *Nature communications,* vol. 7, no. 1, pp. 1-9, 2016.

[106] D. Prochowitz, R. Runjhun, M. M. Tavakoli, P. Yadav, M. Saski, A. Q. Alanzi, D. J. Kubicki, Z. Kaskur, S. M. Zakeeruddin, J. Lewinski and M. Gratzel, "Engineering of Perovskite Materials Based on Formamidinium and Cesium Hybridization for High-Efficiency Solar Cells," *Chemistry of Materials,* vol. 31, no. 5, pp. 1620-1627, 2019.

[107] J.-W. Lee, S.-G. Kim, S.-H. Bae, D.-K. Lee, O. Lin, Y. Yang and N.-G. Park, "The interplay between trap density and hysteresis in planar heterojunction perovskite solar cells," *Nano letters,* vol. 17, no. 7, pp. 4270-4276, 2017.

Appendix A. Photoluminesce Measurements of OHLP Films

A film of FACsPbI3 was fabricated on glass with the intention of carrying out time resolved photoluminescence. Figure A-1 shows said TRPL measurement. However, when compared to the literature in Table A-1, it is clear this film falls short. As a post mortem, we realized that carrying out PL and TRPL measurements of OHLP films in ambient atmosphere was bad as it degraded the films quickly, but were unable to get a hermetically sealed chamber to do PL in a short enough a notice.

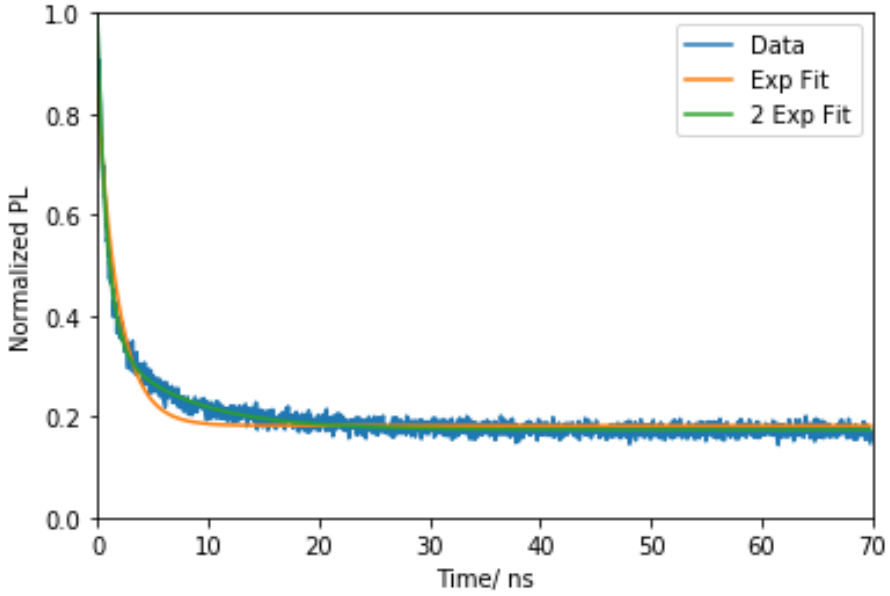

Figure A-1. TRPL measurement of OHLP film.

	τ_1/ ns	τ_2/ ns	τ_{Eff}/ ns
1 Exp Fit	1.908	----	1.908
2 Exp Fit	0.831	7.161	0.745
Literature 1 [106]			38.6
Literature 2 [107]	558.2	5.2	

Table A-1. Predicted carrier lifetimes of OHLP film under two different fits contrasted against literature values.

Appendix B. SRIM Calculations of the Individual Thin Films

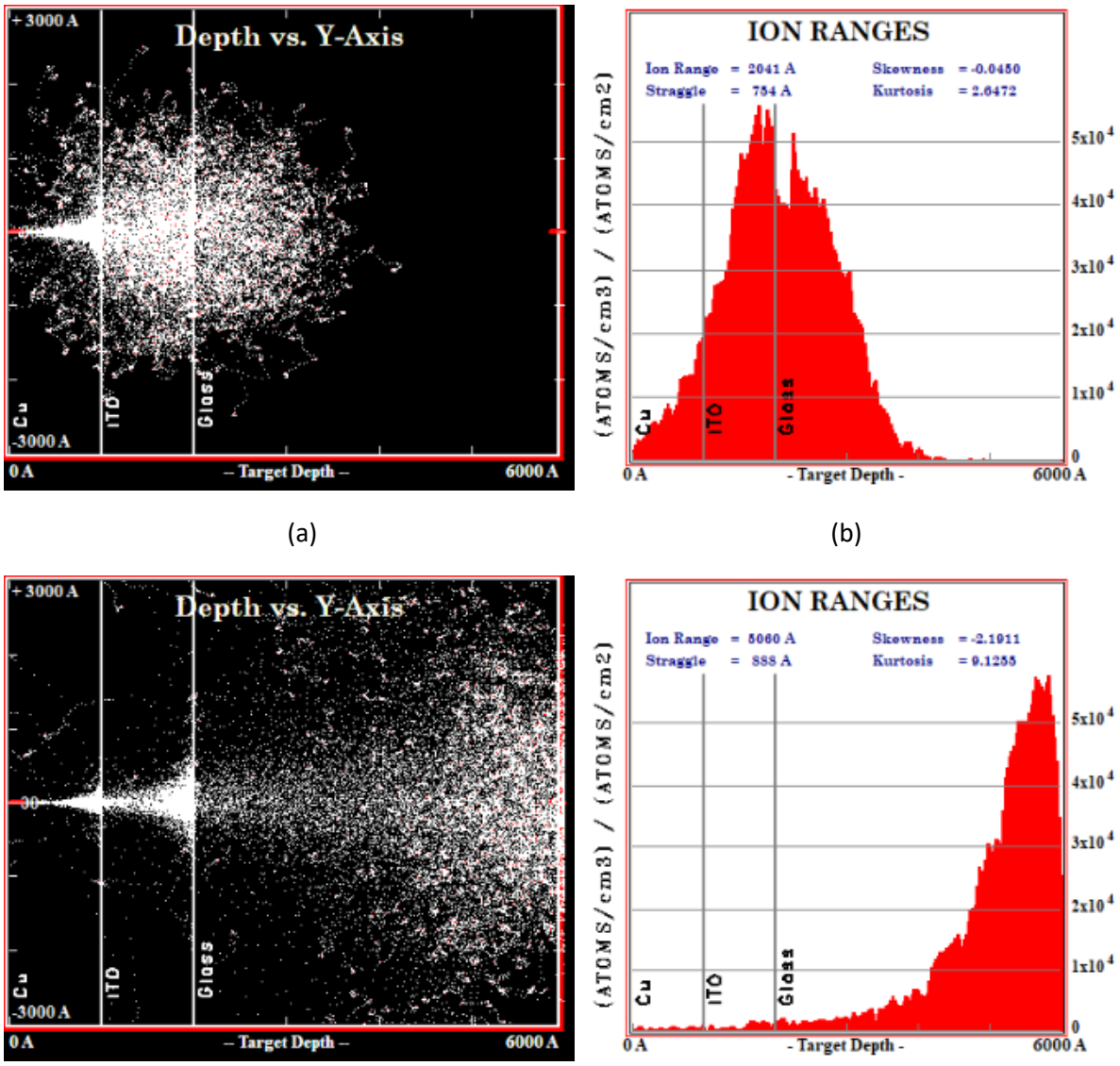

(a) (b)

(c) (d)

Figure B-1: ITO SRIM Calculations for (a) (b) 30keV and (c) (d) 75keV protons.

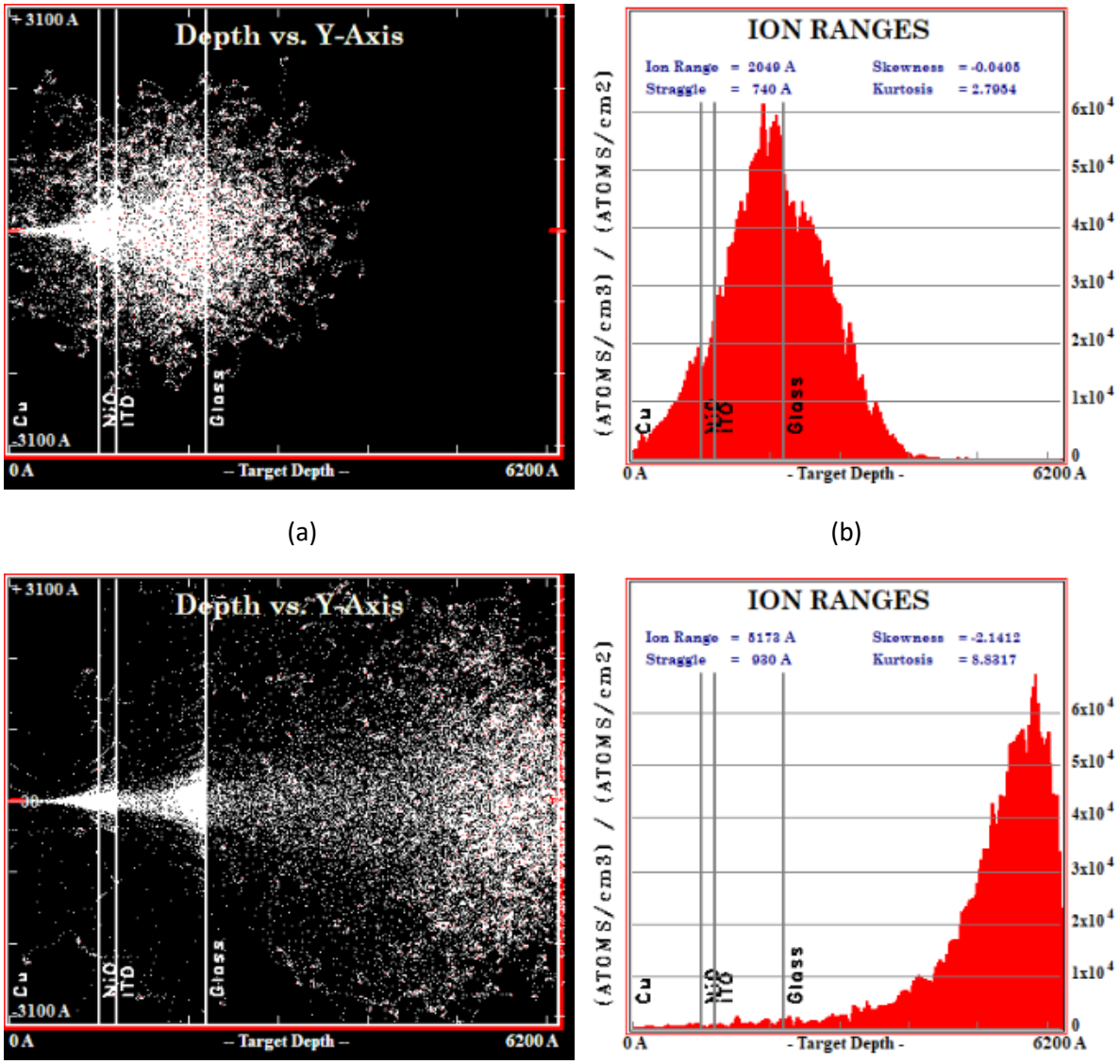

Figure B-2: NiO SRIM Calculations for (a) (b) 30keV and (c) (d) 75keV protons.

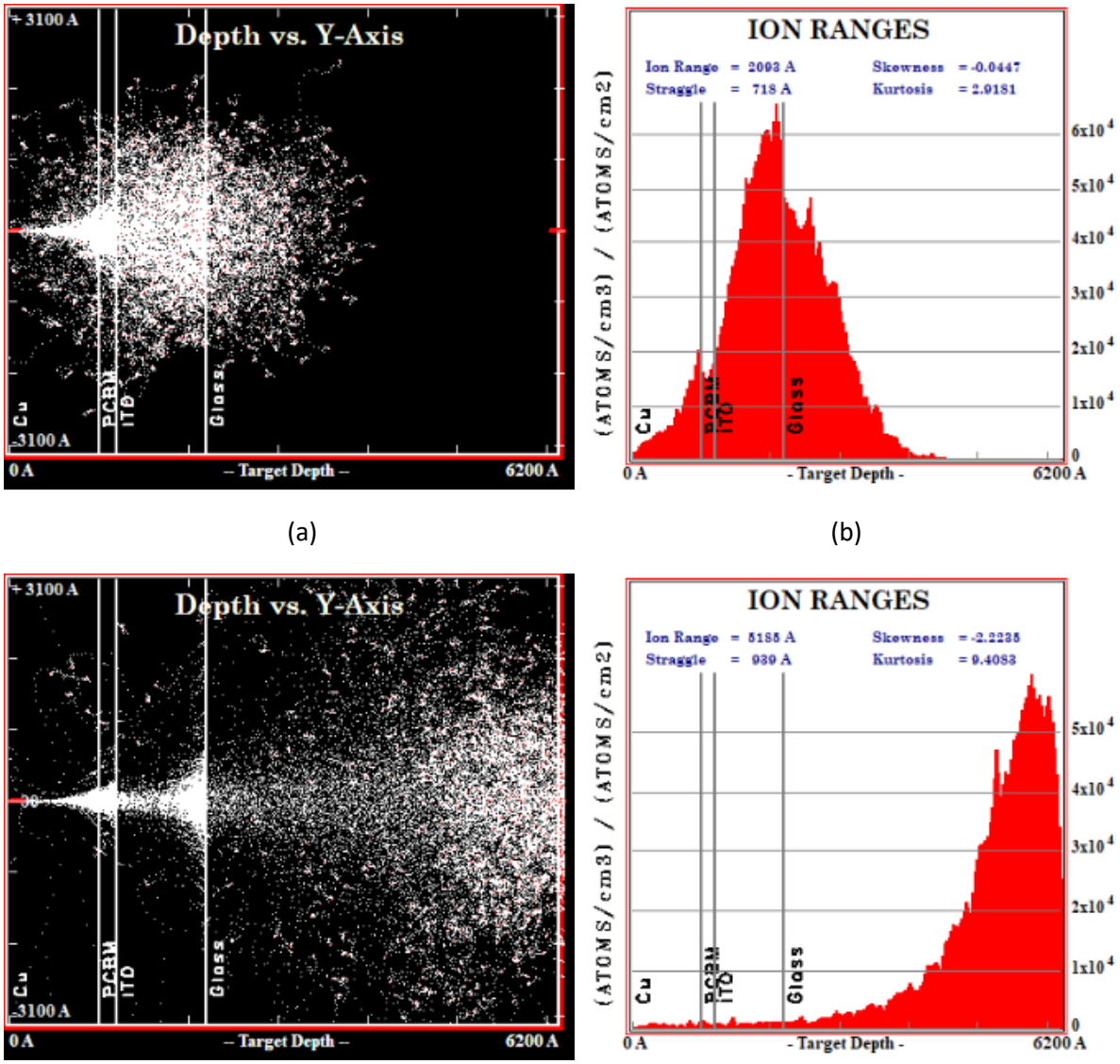

(a) (b)

(c) (d)

Figure B-3: PCBM SRIM Calculations for (a) (b) 30keV and (c) (d) 75keV protons.

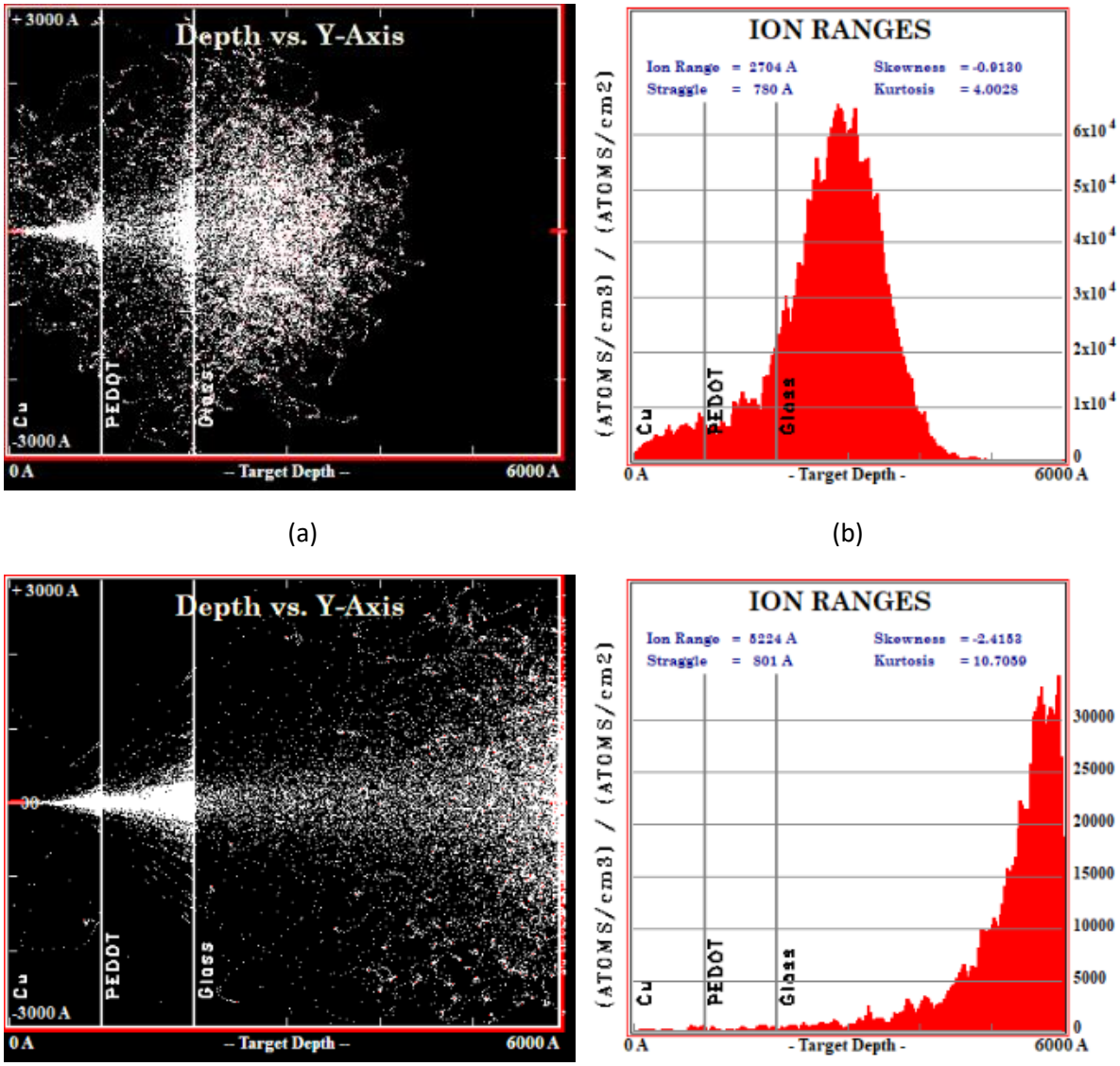

(a) (b)

(c) (d)

Figure B-4: PEDOT SRIM Calculations for (a) (b) 30keV and (c) (d) 75keV protons.

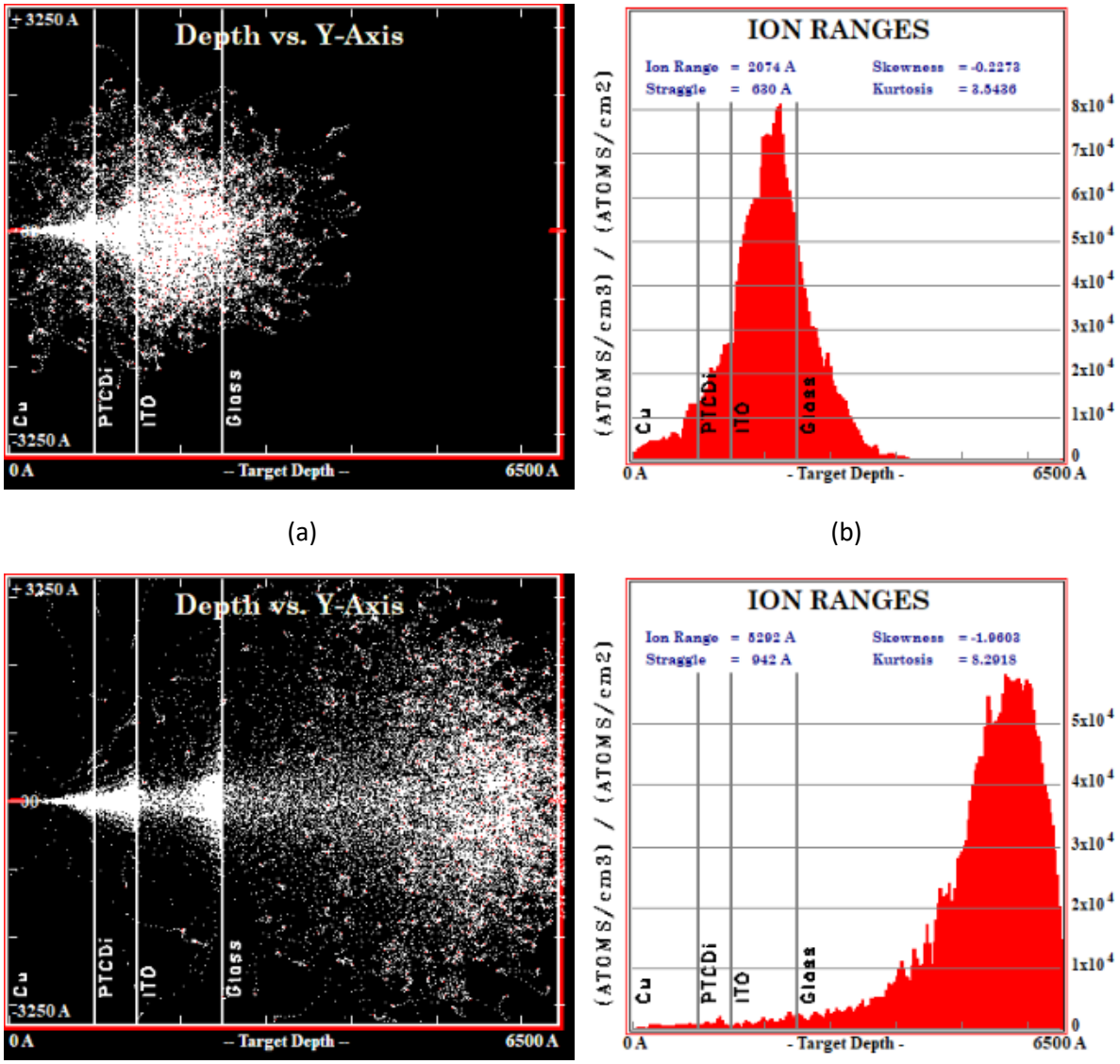

(a) (b)

(c) (d)

Figure B-5: PTCDi SRIM Calculations for (a) (b) 30keV and (c) (d) 75keV protons.

Appendix C. Series Resistance Calculations

```
# -*- coding: utf-8 -*-
"""
Created on Fri Dec 31 13:44:34 2021

@author: Samuel Loke
Go here https://www.pveducation.org/pvcdrom/solar-cell-operation/series-resistance
"""
import numpy as np
import matplotlib.pyplot as plt
from scipy.optimize import fsolve
from sympy.solvers import solve
from sympy import Symbol
from sympy import exp

def IVBase(v):
    JL=35e-3
    J0=1e-19        #Saturation Current Density in A cm-2
    T=300           #Temperature, K
    k=1.3806e-23    #Boltzmann Constant in J K-1
    q=1.60218e-19   #Elementary Charge in C
    n=1             #Ideality Factor
    jguess=J0*(np.exp(q*v/(n*k*T))-1)-JL
    return jguess

def IVPoly(v,Rs,Rsh):
    """
    Parameters
    ----------
    v : Voltage
    Rs : Series Resistance
    Rsh : Shunt Resistance

    Returns
    -------
    j : Current Density
        Solves the parametric equation via parabolic regression- NOT ACCURATE

    """
    JL=35e-3
    J0=1e-19        #Saturation Current Density in A cm-2
    T=300           #Temperature, K
    k=1.3806e-23    #Boltzmann Constant in J K-1
    q=1.60218e-19   #Elementary Charge in C
    n=1             #Ideality Factor
    """
    x = Symbol('x')
    solve(J0*(exp(q*(v+x*Rs)/(n*k*T))-1)-JL+(v+x*Rs)/Rsh-x, x)
    """
    #print(jguess)
    def f(x):
        return J0*(np.exp(q*(v+x*Rs)/(n*k*T))-1)-JL+(v+x*Rs)/Rsh-x
    j=fsolve(f,JL)

    """
    jguess=J0*(np.exp(q*v/(n*k*T))-1)-JL
    j=J0*(np.exp(q*(v+jguess*Rs)/(n*k*T))-1)-JL+(v+jguess*Rs)/Rsh
    while abs((j-jguess)/j)>0.01:
        print(abs((j-jguess)/j))
        jguess=j
        j=J0*(np.exp(q*(v+jguess*Rs)/(n*k*T))-1)-JL+(v+jguess*Rs)/Rsh
    """
```

```
    return j

def IVSimp(v,Rs):
    """
    Parameters
    ----------
    v : Voltage
        Input Voltage
    Rs : Series Resistance in Ohm cm2
        Device Series Resistance

    Returns
    -------
    v2 : Series-corrected Voltage
        DESCRIPTION.
    jguess : Current Density
        In the absence of shunt resistance, we can assume current is the same across the device
    """
    JL=35e-3        #Jsc in A cm-2
    J0=1e-19        #Saturation Current Density in A cm-2
    T=300           #Temperature, K
    k=1.3806e-23    #Boltzmann Constant in J K-1
    q=1.60218e-19   #Elementary Charge in C
    n=1             #Ideality Factor

    jguess=J0*(np.exp(q*v/(n*k*T))-1)-JL
    #print(jguess)
    v2=v+jguess*Rs
    return v2, jguess

def Postproc(j,v):
    p=[]
    if len(v)==len(j):
        for i in range(len(v)):
            p.append(-v[i]*j[i])      #Power density in W cm-2
        pmax=max(p)
        eff=pmax/0.1366     #1366W m-2 = 0.1366W cm-2
        return eff
      else:
          return 'ERROR'

######################## DEFINING DATA ###################################
Rito=4.3324750000000005 #in Ohms
Acirc=0.0248    #In cm2
Lito=100        #In nm
Lpcbm=20        #In nm
Lnio=20         #In nm
Lptcdi=50       #In nm
Lpedot=100      #In nm
resistivity={}
thick={}
thick['tNIO']=Lnio*1E-7
thick['tPCBM']=Lpcbm*1E-7
thick['tPTCDI']=Lptcdi*1E-7
thick['tITO']=Lito*1E-7
thick['tPEDOT']=Lpedot*1E-7
NIO={}
NIO['75_Pre']=[9.477924999999999, 10.705749999999998, 6.9855]
NIO['75_Post']=[12.93075, 15.727500000000001, 10.317425]
NIO['30_Pre']=[7.617325, 9.466450000000002, 8.298325]
NIO['30_Post']=[12.860850000000001, 22.4895, 0.0]

PCBM={}
PCBM['75_Pre']=[5.766125, 5.74955, 4.98375]
```

```
PCBM['75_Post']=[6.013825, 5.534225, 6.728]
PCBM['30_Pre']=[5.176475, 5.110975, 5.143949999999999]
PCBM['30_Post']=[4.90435, 5.103025, 4.83965]

PTCDI={}
PTCDI['75_Pre']=[10.484025, 9.026775, 9.080925]
PTCDI['75_Post']=[10.57425, 9.82395, 13.39025]
PTCDI['30_Pre']=[8.455250000000001, 8.143925, 8.90205]
PTCDI['30_Post']=[9.053875, 12.1564, 9.7686]



ITO={}
ITO['75_Pre']=[0.000134,0.000131,0.000132]
ITO['75_Post']=[0.000134,0.000134,0.000137]
ITO['30_Pre']=[0.000136,0.000135,0.000136]
ITO['30_Post']=[0.000139,0.00014,0.000139]

PEDOT={}
PEDOT['75_Pre']=[0.001276,0.00133,0.001416]
PEDOT['75_Post']=[0.004164,0.009201,0.039895]
PEDOT['30_Pre']=[0.001364,0.001426,0.001437]
PEDOT['30_Post']=[0.002434,0.00372,0.005273]

#Convert to resistivity in Ohm cm
for i in ['75_Pre','75_Post','30_Pre','30_Post']:
    resistivity['NIO_'+i]=NIO[i]
    resistivity['PCBM_'+i]=PCBM[i]
    resistivity['PTCDI_'+i]=PTCDI[i]
    resistivity['ITO_'+i]=ITO[i]
    resistivity['PEDOT_'+i]=PEDOT[i]
    for j in range(3):
        resistivity['NIO_'+i][j]=(NIO[i][j]-Rito)*Acirc/(2*Lnio*1E-7)
        resistivity['PCBM_'+i][j]=(PCBM[i][j]-Rito)*Acirc/(2*Lpcbm*1E-7)
        resistivity['PTCDI_'+i][j]=(PTCDI[i][j]-Rito)*Acirc/(2*Lptcdi*1E-7)
        resistivity['ITO_'+i]

#print(resistivity)
################## Device ####################

voltage=list(range(0,1050)) # In millivolts
device_list=['NIO','PCBM','PTCDI','ITO','PEDOT']
energy=['75','30']
fluence=['4.3E13','8.6E13','1.3E14']


IV={}
effdict={}
try:
    f=open('Radiated_Material_Effect.txt','r+') #r+ opens for read and write, places
pointer at the beginnig of the file
except:
    f=open('Radiated_Material_Effect.txt','x')
f.truncate(0)
f.write('Material\tEnergy/keV\tFluence/p+cm-2\tBefore\tAfter\tNormalized Difference\n')
# For each material, at each energy-fluence, do a before and after calc
for i in device_list:
    for j in energy:
        for k in range(3):
            jbef=[]
            vbef=[]
            jaft=[]
            vaft=[]
            for vtest in voltage:   #Voltage still in millivoltes
                vtest=vtest/1000    #Convert from millivolts to volts
```

```
                    vb,jb=IVSimp(vtest,resistivity[i+'_'+j+'_Pre'][k]*thick['t'+i])
    #Before
                    va,ja=IVSimp(vtest,resistivity[i+'_'+j+'_Post'][k]*thick['t'+i])    #After
                    jbef.append(jb)
                    vbef.append(vb)
                    jaft.append(ja)
                    vaft.append(va)
                #Now plot it
                plt.figure()
                plt.plot(vbef,jbef,label='Before')
                plt.plot(vaft,jaft,label='After')
                plt.title(i+' '+j+' keV '+fluence[k]+' p$^{+}$ cm$^{-2}$')
                plt.ylim([-0.05,0])
                plt.xlim([0,1.2])
                plt.plot([-2,2],[0,0],'k',[0,0],[-100,100],'k')
                plt.legend(bbox_to_anchor=(1.25,0.5),loc='right')
                plt.xlabel('Voltage/ V')
                plt.ylabel('Current Density/ mA cm$^{-2}$')
                #plt.savefig(i+'_'+j+'_Fluence_'+str(k+1)+'.png',bbox_inches='tight')
                #And store data to IV and effdict
                IV[i+'_'+j+'_Pre'+'_v']=vbef
                IV[i+'_'+j+'_Pre'+'_j']=jbef
                IV[i+'_'+j+'_Post'+'_v']=vaft
                IV[i+'_'+j+'_Post'+'_j']=jaft
                effdict[i+'_'+j+'_Pre']=Postproc(jbef,vbef)
                effdict[i+'_'+j+'_Post']=Postproc(jaft,vaft)
                diff=(effdict[i+'_'+j+'_Pre']-
    effdict[i+'_'+j+'_Post'])/effdict[i+'_'+j+'_Pre']

    f.write(i+'\t'+j+'\t'+fluence[k]+'\t'+str(100*effdict[i+'_'+j+'_Pre'])+'\t'+str(100*effdict[
    i+'_'+j+'_Post'])+'\t'+str(diff)+'\n')
     f.close()

```

Material	Energy/keV	Fluence/p+cm-2	Efficiency Before/ %	Efficiency After/ %	Normalized Loss
NIO	30	4.3E+13	23.67237416	23.6171721	0.002331919
NIO	30	8.6E+13	23.65290148	23.51582115	0.005795497
NIO	30	1.3E+14	23.66519713	NA	NA
NIO	75	4.3E+13	23.65278069	23.61643633	0.001536579
NIO	75	8.6E+13	23.63985663	23.58699781	0.002236004
NIO	75	1.3E+14	23.67903879	23.64394413	0.001482098
PCBM	30	4.3E+13	23.69812079	23.70099122	-0.000121125
PCBM	30	8.6E+13	23.6988117	23.69889555	-3.5385E-06
PCBM	30	1.3E+14	23.69846387	23.70167369	-0.000135444
PCBM	75	4.3E+13	23.69190103	23.68928823	0.000110282
PCBM	75	8.6E+13	23.69207587	23.69434716	-9.58673E-05
PCBM	75	1.3E+14	23.70015369	23.68175496	0.000776313
PTCDI	30	4.3E+13	23.66354534	23.65724423	0.000266279
PTCDI	30	8.6E+13	23.66682234	23.62458712	0.001784575
PTCDI	30	1.3E+14	23.65884234	23.64972105	0.000385534
PTCDI	75	4.3E+13	23.6421905	23.6412408	4.017E-05
PTCDI	75	8.6E+13	23.65752948	23.64913844	0.000354688
PTCDI	75	1.3E+14	23.6569595	23.61159965	0.0019174
ITO	30	4.3E+13	23.70702348	23.70702348	1.07653E-12
ITO	30	8.6E+13	23.70702348	23.70702348	1.79433E-12
ITO	30	1.3E+14	23.70702348	23.70702348	1.07653E-12
ITO	75	4.3E+13	23.70702348	23.70702348	0
ITO	75	8.6E+13	23.70702348	23.70702348	1.07641E-12
ITO	75	1.3E+14	23.70702348	23.70702348	1.79409E-12
PEDOT	30	4.3E+13	23.70702347	23.70702347	3.83941E-10
PEDOT	30	8.6E+13	23.70702347	23.70702345	8.2314E-10
PEDOT	30	1.3E+14	23.70702347	23.70702344	1.37645E-09
PEDOT	75	4.3E+13	23.70702348	23.70702345	1.03628E-09
PEDOT	75	8.6E+13	23.70702347	23.70702341	2.8243E-09
PEDOT	75	1.3E+14	23.70702347	23.70702315	1.38072E-08

Table C-1. Predicted normalized efficiency loss due to resistive degradation of transport layers.

Appendix D. Transmission Attenuation Calculations

```
# -*- coding: utf-8 -*-
"""
Created on Wed Feb 23 16:26:46 2022

@author: Samuel Loke

Calculates attenuation of photocurrent and thus efficiency
Uses before and after transmissivity data of HTL, ETL and TCL
Takes MATERIAL_ENERGY.txt tranmission spectra
    Columns are wl, Fl 1-3 Before, Fl 1-3 After
And AM0.txt solar spectrum
And Caelux 5 (561) EQE Spectrum
"""

import os
from scipy.interpolate import interp1d

dir_original=os.getcwd()
os.chdir(dir_original)

list_materials=['ITO','NiO','PCBM','PEDOT','PTCDI']
list_energy=['30','75']
fluence=['4.3E13','8.6E13','1.3E14']

def spectAM0():
    """
    Reads AM0.txt and generates lambda and Intensity
    Spectrum Obtained from https://www2.pvlighthouse.com.au/resources/optics/spectrum%20library/spectrum%20library.aspx
    Returns
    -------
    wl in nm and Isun in W m-2 nm-1 and ph FLux in cm-2 s-1

    """
    f=open('AM0.txt','r')
    wl=[]
    Isun=[]
    phFlux=[]
    for line in f:
        nline=line.split()
        wl.append(float(nline[0]))
        Isun.append(float(nline[1]))
        phFlux.append(float(nline[2]))
    for i in range(len(phFlux)):
        #if i > 0:
        #    phFlux[i]=phFlux[i]-phFlux[i-1]
        phFlux[i]=0.1*Isun[i]*wl[i]*10E-9/(1.98644568*10E-25)  # Converts W/m2nm into mA/cm2nm
    f.close()
    return [wl, Isun, phFlux]

def getT(filename):
    """
    Takes MATERIAL_ENERGY.txt and extracts the tranmission data inside
    Parameters
    ----------
    filename : String
        Must be MATERIAL_ENERGY.txt of format
        wl f1a f2a f3a f1b f2b f3b
    Returns
    -------
```

```
    [wl f1a f2a f3a f1b f2b f3b]
        a is Pre rad, b is Post rad
    """
    wl=[]
    f1a=[]
    f2a=[]
    f3a=[]
    f1b=[]
    f2b=[]
    f3b=[]
    f=open(filename+'.txt','r')
    for line in f:
        nline=line.split()
        try:
            wl.append(float(nline[0]))
            f1a.append(float(nline[1]))
            f2a.append(float(nline[2]))
            f3a.append(float(nline[3]))
            f1b.append(float(nline[4]))
            f2b.append(float(nline[5]))
            f3b.append(float(nline[6]))
        except:
            print('Oops')
    f.close()
    return [wl,f1a,f2a,f3a,f1b,f2b,f3b]

def getEQE():
    """
    Gets EQE from file EQE
    Returns
    -------
    [wl,EQE]
    """
    wl=[]
    EQE=[]
    f=open('EQE.txt','r')
    for line in f:
        nline=line.split()
        wl.append(float(nline[0]))
        EQE.append(float(nline[1]))
    f.close()
    return [wl,EQE]

def calcT(wl,Isun,T):
    """
    Calculates transmissivity

    Parameters
    ----------
    wl : List
        Wavelength range. 300 to 1095
    Isun : interp1d
        Interpolated Sun intensity.
    T : interp1d
        Interpolated spectral transmissivity.

    Returns
    -------
    T : Transmissivity
    """
    dWL=wl[1]-wl[0]
    numer=0
    denom=0
    for i in range(len(wl)):
        numer=numer+Isun(wl[i])*T(wl[i])*dWL
```

```
125.          denom=denom+Isun(wl[i])*dWL
126.      T=numer/denom
127.      return T
128.
129.  def calcJsc(wl,EQE,flux,T):
130.      """
131.      Calculates transmissivity
132.
133.      Parameters
134.      ----------
135.      wl : List
136.          Wavelength range. 300 to 1095
137.      flux : interp1d
138.          Interpolated Solar Flux.
139.      T : interp1d
140.          Interpolated spectral transmissivity.
141.
142.      Returns
143.      -------
144.      Jsc : Current density
145.      """
146.      q=1.60218e-19
147.      dWL=wl[1]-wl[0]
148.      Jsc=0
149.      for i in range(len(wl)):
150.          Jsc=Jsc+q*EQE(wl[i])*flux(wl[i])*T(wl[i])*dWL
151.      return Jsc
152.
153.  #######
154.  #BEGIN#
155.  #######
156.
157.  try:
158.      f2=open('Jsc_Attenuation.txt','r+') #r+ opens for read and write, places pointer at
    the beginnig of the file
159.  except:
160.      f2=open('Jsc_Attenuation.txt','x')
161.  f2.truncate(0)
162.  f2.write('Material\tEnergy/keV\tFluence/p+cm-2\tBefore\tAfter\tNormalized Difference\n')
163.
164.  wl_T=list(range(300,1095))
165.  wl_Jsc=list(range(300,900))
166.  raw_spect=spectAM0()
167.  interp_Isun=interp1d(raw_spect[0],raw_spect[1],fill_value='extrapolate')
168.  interp_flux=interp1d(raw_spect[0], raw_spect[2],fill_value='extrapolate')
169.  raw_EQE=getEQE()
170.  interp_EQE=interp1d(raw_EQE[0], raw_EQE[1],fill_value='extrapolate')
171.  for i in list_materials:
172.      for j in list_energy:
173.          #Order of list is f1a, f2a, f3a, f1b, f2b, f3b
174.          list_T=[]
175.          list_Jsc=[]
176.          data_T=getT(i+'_'+j)
177.          for k in range(len(data_T)-1):
178.              interp_T=interp1d(data_T[0],data_T[k+1],fill_value='extrapolate')
179.              list_T.append(calcT(wl_T,interp_Isun,interp_T))
180.              list_Jsc.append(calcJsc(wl_Jsc,interp_EQE,interp_flux,interp_T))
181.          print(list_T)
182.          print(list_Jsc)
183.          for l in range(3):
184.
    f2.write(i+'\t'+j+'\t'+fluence[l]+'\t'+str(list_T[l])+'\t'+str(list_T[l+3])+'\t'+str(1-
    list_Jsc[l+3]/list_Jsc[l])+'\n')
185.  f2.close()
```

Material	Energy/keV	Fluence/p+cm-2	Transmission Before	Transmission After	Normalized Loss
NiO	30	4.30E+13	0.876478088	0.878255537	-0.001858208
NiO	30	8.60E+13	0.867413728	0.874615163	-0.009886541
NiO	30	1.30E+14	0.87146779	NA	NA
NiO	75	4.30E+13	0.867676138	0.86712177	-0.000604195
NiO	75	8.60E+13	0.869416627	0.873161085	-0.006652866
NiO	75	1.30E+14	0.864200595	0.871865371	-0.011525453
PCBM	30	4.30E+13	0.845131319	0.839149054	0.007283138
PCBM	30	8.60E+13	0.845017413	0.84032671	0.006428054
PCBM	30	1.30E+14	0.839276234	0.838211712	0.001566577
PCBM	75	4.30E+13	0.842218364	0.834792343	0.009279459
PCBM	75	8.60E+13	0.841687797	0.835939398	0.007940335
PCBM	75	1.30E+14	0.842060125	0.836051956	0.008787797
PTCDI	30	4.30E+13	0.49228072	0.486978092	0.01085311
PTCDI	30	8.60E+13	0.492348448	0.478900437	0.027326094
PTCDI	30	1.30E+14	0.488419089	0.479452219	0.017377805
PTCDI	75	4.30E+13	0.493282849	0.479451212	0.026088377
PTCDI	75	8.60E+13	0.483329433	0.472177837	0.019300754
PTCDI	75	1.30E+14	0.495944161	0.48420571	0.017367971
ITO	30	4.30E+13	0.831364144	0.825278065	0.006256814
ITO	30	8.60E+13	0.829054625	0.82696457	0.002055019
ITO	30	1.30E+14	0.828429308	0.82249561	0.005836976
ITO	75	4.30E+13	0.830171598	0.825339827	0.004911437
ITO	75	8.60E+13	0.832252098	0.826851155	0.006220966
ITO	75	1.30E+14	0.831191431	0.824979066	0.006374626
PEDOT	30	4.30E+13	0.839211187	0.814903131	0.023635684
PEDOT	30	8.60E+13	0.842242588	0.808552468	0.032692028
PEDOT	30	1.30E+14	0.840168909	0.80391349	0.034588122
PEDOT	75	4.30E+13	0.839065617	0.802487489	0.035376584
PEDOT	75	8.60E+13	0.843979871	0.798097904	0.043847025
PEDOT	75	1.30E+14	0.845368617	0.784835145	0.0575629

Table D-1. Predicted normalized efficiency loss due to darkening of transport layers.